University of Zurich

Master's Thesis

The galaxy–dark matter connection

by **Tobias Baldauf**
University of Zurich
t.baldauf@tbaweb.de

supervised by **Prof. Dr. Uroš Seljak**
Institute for Theoretical Physics
University of Zurich

Physics and Astronomy Department
University of California, Berkeley

and **Dr. Robert E. Smith**
Institute for Theoretical Physics
University of Zurich

Zurich, February 2009

Abstract

We use dissipationless N-body simulations to investigate the correlation between dark matter and galaxy distribution in the Universe. The dark matter haloes identified in the N-body simulations are populated with galaxies according to the Halo Occupation Distribution. We then use galaxy-clustering and galaxy-galaxy lensing measurements for Luminous Red Galaxies from the Sloan Digital Sky Survey to fit for the free parameters of the occupation statistics. In this vein we obtain realistic galaxy catalogues and use them for our examination of the cross-correlation coefficient between the LRGs and the matter. As our key result we propose and test a new method to constrain the dark matter autocorrelation from observable galaxy-galaxy lensing and galaxy clustering. Most of our conclusions are based on the projected correlation function $w(R)$, which leads us to quantify its dependence on redshift space distortions. As a side project we implement a fast grid based method for the calculation of correlation functions and their projections from N-body simulations.

To my parents

Acknowledgements

First of all I would like to thank Prof. Dr. Uroš Seljak for providing me with this topic and enabling me to carry out my research in his group. Guiding me through this work and giving me inspirations for new aspects of the topic helped me to develop a comprehensive picture of the subject.
I would like to thank Dr. Robert Smith for the enormous support he has given to me. Encouraging me to critically reconsider some of the preliminary results and to carefully study the theoretical framework helped me to evolve towards a better physicist. I also appreciate him for hours of discussions, for bearing my infinite number of questions and for valuable comments on the manuscript of this work.
I am also very grateful to Dr. Vincent Desjacques and Dr. Ilian Iliev for discussions and help with the simulations during the initial stages of the project.
The galaxy clustering and galaxy-galaxy lensing data used in this thesis were kindly provided by Rachel Mandelbaum, Institute for Advanced Study, Princeton.
The Institute for Theoretical Physics provided a perfect working environment, both in terms of the computing equipment as well as in terms of the nice atmosphere. Particularly I would like to thank the PHD students Nico Hamaus and Lucas Lombriser and my office mate Willy Kranz for hours of discussions about physics, programming and daily life.
Special thanks to my family for enabling me my studies and for pointing out to me that there are other things in life than physics.
Finally, I gratefully acknowledge support by a grant of the German Academic Foundation.

Zurich, February 2009

Contents

CHAPTER 1

Introduction

This first chapter will start with a short description of the major scientific cognitions that lead to the current understanding of the Universe, before we proceed with a summary of important events in the cosmic history. Finally we will try to motivate our investigations.
The organisation of the following chapters is as follows: In §2 we will lay down the fundamentals of general relativity and cosmology in a smooth homogeneous Universe, before we proceed to the origin of perturbations on the smooth background Universe in §3. The discussion in §4 will then be devoted to the statistics, frequently used to describe the cosmological random fields, especially power spectra and correlation functions. The formation of non-linear structures will be treated in §5, where we also derive the abundance of dark matter haloes and comment on the halo model of large scale structure. Gravitational lensing, especially weak lensing will be covered in §6. This chapter also provides the necessary formalism for our galaxy-galaxy lensing analysis. All this theory is then used in §7 to develop the techniques necessary for our analysis, especially for the extraction of correlation functions from the simulations and for the adaption of the occupation statistics. Finally we will describe our findings in §8 and discuss them in §9. Readers familiar with the concepts of cosmology should directly jump to §6 on Page 39, where we start to present our own achievements.

1.1 Historical Context

Mankind was observing the night sky for thousands of years but it was not before the 16th and 17th century that physicists like Galileo Galilei, Johannes Kepler and Isaac Newton developed a mathematical theory of gravitation which could coherently account for the planetary orbits. This very successful theory of gravitational force turned out to be the weak field limit of general relativity, which was presented by Albert Einstein in 1915. Based on his earlier work on special relativity, he developed a geometric theory of gravity, which abandons the idea of gravity acting as a force and rather considers it as a property of a curved four dimensional spacetime. The core of the mathematical realisation of this theory are the Einstein field equations, relating curvature of spacetime to its energy content. The correct prediction of the excess precession of Mercury's orbit around the sun was a first confirmation for the new theory. Another validation was published in 1919, when an expedition lead by Arthur Eddington measured the light deflection by the sun during a total eclipse.
At that time astronomers also started to look beyond our local galaxy and realised that the mysterious observed nebulae were nothing more than distant galaxies. Beginning with Edwin Hubble's observations in the 1920s, first quantitatively relevant measurements of the properties of the Universe became available. After a decade of observations Hubble discovered, in

1929, that distant galaxies are receding from us with a velocity proportional to their distance. Independently, Alexander Friedmann in 1922 derived the so called Friedmann equations from the Einstein field equations, using the metric of a homogeneous and isotropic spacetime and the energy momentum tensor of a perfect fluid. The Friedmann equations in fact could predict the expansion that was observed by Hubble.
Another milestone for todays understanding of the evolution of our Universe was the discovery of the **cosmic microwave background** (CMB) radiation by Penzias & Wilson in 1964. This radiation, which shows an almost perfect Planckian spectrum of $T_{\mathrm{CMB}} = 2.725$ K, is a remnant from the early hot epoch of the Universe when the interstellar gas was still ionised and scattered photons efficiently. At a time known as **recombination** the electrons and nuclei formed neutral atoms, leading to an unscattered propagation of the photons, which is what we detect today. The cosmic microwave background explorer (COBE) experiment, starting in 1989, measured the anisotropies of the CMB and found fluctuations in the temperature of $\Delta T/T \approx 10^{-5}$. This was consistent with the inflationary paradigm, introduced by Alan Guth in 1981 to describe the large scale homogeneity and the flatness observed today. In addition, inflation can account for the seeds of structure formation.
All these observational efforts and theoretical models went hand in hand and finally led to a paradigm, which now is known as the **standard model of cosmology** and the Lambda Cold Dark Matter (ΛCDM) cosmology. Its main statements are:

- The spacetime of our Universe is globally flat.
- Approximately 25% of the total energy content of the Universe is in the form of matter, but only one sixth of the matter is of baryonic nature.
- The rest of the energy content is unknown and attributed to **dark energy**.

However, as a consequence of this model we are in the miserable situation that we are not able to observe 95% of the energy content of the Universe, since it is made up of dark ingredients. Dark energy, first introduced as a possible **cosmological constant** in the field equations by Einstein, became again popular in the last decade to account for the accelerated expansion of the Universe. It is a key question of cosmology to determine the nature of this exotic field, which comes along with negative pressure. Having said that, we furthermore have to deal with **dark matter**, an invisible, i.e. noninteracting kind of matter, which was introduced to describe the flat galaxy rotation curves observed by Vera Rubin in th 1960s. So far there has not been evidence for direct detection of dark matter and there has been a whole industry inventing modified versions of gravity in order to remedy the dark components.
Today we are not claiming to have a complete understanding of the processes, which govern our Universe – we are working on transient ideas and try to improve them. Cosmology has to deal with physical processes on scales of the observable Universe down to scales relevant for particle physics, and time intervals which span the whole age of the Universe. Due to the complexity we have to adopt a lot of simplifying assumptions to make the system mathematically tractable. If we just consider the gravitational forces that form the large scale structure of the Universe, we soon come to a point where perturbative calculations break down and a non-linear numerical treatment has to be used. The problems become even more involved as soon as we consider the baryon physics, which leads to the formation of stars and galaxies. This complexity has lead to an intensive use of numerical simulations over all scales. Furthermore, the field of research is separated into branches dealing with large scale structure, individual haloes, galaxies and galaxy clusters down to star and planet formation. Our work will be mainly concerned with the large scale structure of the Universe.

1.2 Cosmic Timeline

Table 1.1 shows a short curriculum vitae of our Universe, which we will explicate in the following. The Universe started with a singularity known as the **big bang**. We don't have a very detailed understanding of what happened in the first 10^{-43} s of the Universe. Most probably

a theory of quantum gravity, which describes the unification of the four fundamental forces, will be needed to describe this time. However, this hot, small Universe started to expand and by doing so it cooled. At some point, the temperature decreased so much, that the quark gluon plasma underwent a phase transition to form the colour neutral baryons and mesons, a process known as **quantum chromodynamics phase transition**. A general appearance in cosmic history is that processes drop out of equilibrium, since their crosssections decrease with decreasing cosmic temperature. This caused for instance a decoupling of the neutrinos and a freeze out of the neutron to proton ratio. Later on, these constituents started to form the lightest elements by nuclear fusion. This happened during the epoch of **nucleosynthesis**, for which predicted element abundances compare remarkably well with observations. Apart from being globally neutral, at this time locally there were still free electrons and nucleons. This era ended with **recombination** at redshift $z \approx 1100$, when the free electrons and the nucleons started to combine to form neutral atoms. At this point the photons stopped to interact effectively with the electrons and the opaque Universe became more less transparent for the radiation. This event is imprinted in the Universe by the **last scattering surface** or **cosmic microwave background** (CMB). The photons which were released during recombination could travel relatively undisturbed to the present time, while they were cooling to give the astonishingly homogeneous blackbody radiation field of temperature $T_{\mathrm{CMB}} = 2.75$ K. This homogeneity is an important constituent of the cosmological standard model, but there are small temperature inhomogeneities in the temperature field that are an imprint of the slightly inhomogeneous matter distribution at recombination.
These inhomogeneities grew by the gravitational evolution and once they were large enough, first dark matter haloes were formed by the process of gravitational collapse. Subsequently these haloes merged and formed larger and larger haloes. The baryonic gas initially followed the dark matter and accreted in the dark matter potential wells. There it could reach sufficiently high densities to cool efficiently and to condense. The first galaxies were then created by star formation from the cold gas.

Event	T	z	t
Now	2.73 K	0	14 Gyr
Formation of first structures	140 K	50	14 Gyr
Recombination	300 K	1100	500000 yr
Matter-radiation equality	9500 K	3500	20000 yr
Nucleosynthesis	4×10^8 K	1×10^8	1×10^3 s
Baryogenesis	1×10^{12} K	1×10^{12}	1×10^{-5} s
Inflation ends	1×10^{27} K	1×10^{27}	1×10^{-32} s
Quantum gravity	1×10^{32} K	1×10^{32}	1×10^{-43} s

Table 1.1: Timeline of events in the history of the Universe [Liddle & Lyth, 2000, Rich, 2001]. This table is thought as an overview and quoted values should not be taken at face value.

1.3 Motivation

According to the current understanding of our Universe, the main ingredients are dark matter and dark energy. Due to their dark nature both fields are not observable directly and indirect methods have to be devised to infer the distribution of dark matter and dark energy. Hence it is important for current and future observations to develop a detailed understanding of how well the luminous baryonic matter in our Universe traces the dark matter.
Once the data of large galaxy redshift surveys such as the Sloan Digital Sky Survey (SDSS) [York *et al.* , 2000] or the 2dF Galaxy Redshift Survey (2dFGRS) [Colless *et al.* , 2001] became available, studies of the clustering properties of galaxies as a function of luminosity and colour were possible. Galaxies are believed to form in the dark matter haloes [White & Rees, 1978] and consequently the clustering of the galaxies will be related to the clustering of haloes as

predicted from numerical simulations or the Press & Schechter approach. An open question is how halo mass and galaxy morphology are related, which galaxies reside in a certain kind of halo and how they are distributed. An answer to this question should come from a theory of galaxy formation, but there is not yet a coherent picture. Hence statistical models of galaxy distribution have to be used to investigate the correlation between the galaxies and the dark matter.

So far surveys have in most cases been analysed under the assumption that galaxies are a biased tracer of the dark matter density field. But this bias is a unknown parameter, which in addition seems to be scale dependent [Smith *et al.* , 2007]. Hence it is interesting to look for a way that enables direct inference to the dark matter distribution. One of the most promising observational direct probes of the dark matter on cosmological scales is the gravitational lensing. The lensing essentially probes small, non-linear scales and is hence complementary to clustering measurements that probe large, linear scales.

Since the first attempts to detect the galaxy-galaxy lensing by [Tyson *et al.* , 1984] the quality of the data has been improved by deeper and wider surveys. Galaxy-galaxy lensing has now been measured with relatively high signal-to-noise and as a function of a wide variety of properties of the lens galaxies [Guzik & Seljak, 2002, Mandelbaum *et al.* , 2006b]. It has become clear in these studies that galaxy-galaxy lensing contains much information about the mass distribution around galaxies and has the potential to measure dark matter halo radii, shapes, concentrations and masses [Mandelbaum *et al.* , 2006c, Mandelbaum *et al.* , 2008].

The interpretation of the signal in terms of the link between galaxies and dark matter is however complicated by the fact that lensing is only detectable by stacking the signal from many lenses. Theoretical modelling of the galaxy-galaxy lensing has been done both with numerical simulations [Hayashi & White, 2007] and with the halo model [Guzik & Seljak, 2001]. It was shown that the signal can be well reproduced assuming an NFW profile and simple models for the halo occupation statistic. The combination of lensing and clustering seems to hold the potential to put constraints on cosmological parameters [Yoo *et al.* , 2006, Cacciato *et al.* , 2008].

In addition to the direct use of galaxy-galaxy lensing and clustering for cosmological parameter estimation one could use the projected lensing and clustering to determine the relative bias, and from that derive the bias of the galaxy sample with respect to the matter [Seljak & Warren, 2004, Bonoli & Pen, 2008]. Usually the clustering is measured with higher statistical significance, but due to the lack of bias one is not able to infer the amplitude of the matter correlation. Bias measurements are usually performed on large, linear scales, but if one would be able to recover the linear galaxy-matter and galaxy-galaxy correlations on small scales, one should be able to recover the bias already on scales around 10 h^{-1}Mpc.

For all these studies it is important to develop an understanding how well the galaxies trace the dark matter distribution. Cosmological simulations of the dark matter density field are a standard tool to investigate the non-linear evolution of the collisionless dark matter field. Despite their statistical power in describing the large scale structure of the Universe, these simulations have the disadvantage that they are not providing the distribution of the galaxies probed in cosmological surveys. Consequently it would be of great benefit to supplement the the simulations with information about the galaxies residing within the dark matter haloes. Such galaxy catalogues can help to extend the theoretical investigations on haloes to observable quantities.

We consider the Luminous Red Galaxies (LRGs), a subset of the galaxies observed with the Sloan Digital Sky Survey (SDSS) for our investigations. These galaxies are believed to reside in the most massive dark matter haloes of the Universe, which can be probed in large scale cosmological N-body simulations with sufficient accuracy. The dark matter haloes are populated with galaxies according to the Halo Occupation Distribution (HOD). In order to obtain reasonable galaxy catalogues we fit the parameters of the HOD using galaxy clustering and galaxy-galaxy lensing measurements. The final goal of our investigations is to devise a method that can recover the dark matter correlation from observable quantities.

To conclude we will summarise the main goals of this thesis:

1. Develop a fast algorithm for calculation of correlation functions from the N-body simulations and their projections on scales down to $R_{\rm min} = 0.1\ h^{-1}$Mpc.

2. Populate the dissipationless simulations with galaxies according to the halo occupation distribution and find the parameters that can reproduce galaxy-galaxy lensing and clustering for two LRG samples from the SDSS.

3. Use these galaxy catalogues to investigate how well the dark matter correlation function can be recovered from the lensing and clustering measurements.

4. Investigate the effect of redshift space distortions on the projected correlation function.

CHAPTER 2

The Expanding Universe

It will be crucial for the understanding of the concepts used in this work to be familiar with the basic ideas of general relativity and the expanding Universe. Hence we will start with a brief introduction of general relativity. We refer the reader to standard textbooks on general relativity [Carroll, 2004] for a more detailed treatment. We then consider the solutions of the Einstein equations, that are believed to describe our Universe. Afterwards we will devote a short section to distances and luminosity measures, we will need later on. Finally we will comment on the nature of dark matter and describe in brevity the most viable dark matter candidates.

2.1 Fundamentals of General Relativity

The basic and simple principle which underlies general relativity (GR) is the **equivalence principle**:

In small enough regions of spacetime the laws of physics reduce to those of special relativity, it is impossible to detect the existence of a gravitational field by using local experiments. In a freely falling local frame all physical processes look as if there was no gravitation.

In special relativity one is used to inertial or Minkowski frames, which are unaccelerated with respect to each other but there is no distinguished frame which could be considered as a fixed static reference. Similarly in GR we have that gravity is inescapable as there is no gravitational neutral object. So all test bodies evolve under the influence of gravity and we have no fixed object w.r.t. which we could define an acceleration due to gravity. Consequently we give up the idea of gravity acting as a force but rather consider it as curvature of spacetime and define

unaccelerated $\equiv$ freely falling.

But the property of being unaccelerated will only hold for very small (in fact infinitesimally small) regions of spacetime. Therefore we won't be able to define a large inertial frame, which would enable us to define such things as relative velocities of far away objects. We have to restrain ourselves to **local inertial frames**.
We come to the conclusion that we can interpret the spacetime as being a curved manifold due to the following reasons:

- In small regions of a curved manifold we can establish Riemann normal coordinates for which the metric is Minkowski and the first derivatives of the metric vanish. In this coordinates the laws of physics look like those in flat Minkowski space.

- The result of parallel transporting a vector on a curved manifold depends on the way taken. This is a representation of the inability to compare vectors at widely separated regions in general relativity.

Now that we know which mathematical background can describe the spacetime, we have to consider the objects which live on this manifold, vectors and tensors. Tensor calculus essentially states that physical laws which are valid in flat space, will be true in any coordinate system if they are written in tensorial form and partial derivatives are replaced by **covariant derivatives**. The covariant derivative is constructed to reduce to the usual partial derivative when applied to scalars and to obey Leibniz rule. Application on a vector reads as

$$\nabla_\mu V^\nu = \partial_\mu V^\nu + \Gamma^\nu_{\mu\lambda} V^\lambda. \tag{2.1}$$

Here we introduced the so called **connection** or Christoffel symbols, which can be derived from the metric $g_{\mu\nu}$ if the covariant derivative is metric compatible and the connection is torsion free.[1]

$$\Gamma^\sigma_{\mu\nu} = \frac{1}{2} g^{\sigma\rho} \left(\partial_\mu g_{\rho\nu} + \partial_\nu g_{\mu\rho} - \partial_\rho g_{\mu\nu}\right) \tag{2.2}$$

In flat space force free particles move on straight lines $\ddot{x} = 0$, which can be generalised to obtain the **geodesic equation**

$$\frac{d^2 x^\nu}{d\lambda^2} + \Gamma^\nu_{\sigma\rho} \frac{dx^\sigma}{d\lambda} \frac{dx^\rho}{d\lambda} = 0, \tag{2.3}$$

where λ is an arbitrary parametrisation of the path. So far we considered how a curved spacetime influences the motion of test particles and how the connection can be derived from the metric. As a next step we have to consider how the energy content of the spacetime, described by the **energy-momentum tensor** $T_{\mu\nu}$, influences the curvature. To do so it will turn out convenient to introduce Riemann tensor

$$R^\mu{}_{\nu\sigma\rho} = \partial_\sigma \Gamma^\mu_{\rho\nu} - \partial_\rho \Gamma^\mu_{\sigma\nu} + \Gamma^\mu_{\sigma\lambda}\Gamma^\lambda_{\rho\nu} - \Gamma^\mu_{\rho\lambda}\Gamma^\lambda_{\sigma\nu}, \tag{2.4}$$

as well as the Ricci tensor, Ricci scalar and Einstein tensor

$$R_{\mu\nu} = R^\gamma{}_{\mu\gamma\nu}, \qquad R = R^\mu{}_\mu, \qquad G_{\mu\nu} = R_{\mu\nu} - \frac{1}{2} R g_{\mu\nu}. \tag{2.5}$$

The field equations which determine the dynamics of the spacetime are known as **Einstein equations** and can be derived from a weak field equivalence to Newton and Poisson equations or equivalently from an action principle.

$$\boxed{G_{\mu\nu} = 8\pi G T_{\mu\nu} + \Lambda g_{\mu\nu}} \tag{2.6}$$

The last term on the right hand side is the so called **cosmological constant**. It was introduced by Einstein in order to find a static solution of the Universe. Lateron he called this the "Biggest blunder" of his life but, as we will see below, today there is striking evidence for a nonzero value of this constant.

2.2 Fundamentals of Cosmology

Assuming the validity of general relativity we have to make a further assumption in order to obtain a solution of the Einstein field equations that describes the Universe. This assumption is called the **Copernican principle** and states that our Universe is homogeneous and isotropic. Here isotropy says that the space looks the same irrespective in which direction one looks and homogeneity states that it looks the same irrespective from where one looks. The assumption implies that we are in no way special, we are sitting in an average galaxy and hence we are

[1] Here we used Einstein summation convention were equal upper and lower indices are summed over

observing an average representation of the Universe. These statements are for sure only true if we average over local inhomogeneities, such as galaxies and clusters of galaxies, and the smoothing scale is taken to be around 100 h^{-1}Mpc.
Einstein first tried to find a static solution to his field equations but as observations implied there is a recession of far away galaxies. So we have to drop the assumption of a static spacetime and replace it by a spacetime Υ which is homogeneous and isotropic in space but not in time. Hence we decompose it into a set of maximal symmetric spacelike slices Σ and the time component $\Upsilon = \mathbb{R} \times \Sigma$. The line element of this spacetime can be expressed as

$$ds^2 = -dt^2 + a^2(t)\gamma_{ij}du^i du^j. \tag{2.7}$$

Here we introduced the **scale factor** a, which is by convention set to unity today $a_0 = 1$, and used **comoving coordinates**, which are free of cross terms with the time component. The maximal symmetric spatial metric γ_{ij} should obey spherical symmetry. This symmetry can be used to derive the general form of the **Robertson Walker metric**

$$ds^2 = -dt^2 + a^2(t)\left[\frac{dr^2}{1-Kr^2} + r^2 d\Omega^2\right]. \tag{2.8}$$

Here K describes the spatial curvature of the Universe and the angular part of the metric is given by $d\Omega = d\theta^2 + \sin^2\theta d\phi^2$. We have to distinguish three cases:

open Universe ($K < 0;\ \rho < \rho_{crit};\ \Omega < 1$) There is constant negative curvature on Σ and we can set $r = S_K(\chi) = (-K)^{-1/2}\sinh\left[(-K)^{1/2}\chi\right]$.

$$\gamma_{ij}du^i du^j = d\chi^2 + (-K)^{-1/2}\sinh^2\left[(-K)^{1/2}\chi\right]d\Omega^2$$

flat Universe ($K = 0;\ \rho = \rho_{crit};\ \Omega = 1$) There is no curvature on Σ yielding the Euclidean metric and $r = S_K(\chi) = \chi$.

$$\gamma_{ij}du^i du^j = d\chi^2 + \chi^2 d\Omega^2 = dx^2 + dy^2 + dz^2$$

closed Universe ($K > 0;\ \rho > \rho_{crit};\ \Omega > 1$) There us positive curvature on Σ and we can set $r = S_K(\chi) = K^{-1/2}\sin\left[K^{1/2}\chi\right]$ to obtain the metric of a three sphere.

$$\gamma_{ij}du^i du^j = d\chi^2 + K^{-1/2}\sin^2\left[K^{1/2}\chi\right]d\Omega^2$$

The meaning of ρ_{crit} and Ω will be described below and is included in this overview for the sake of completeness. All these three cases can be conveniently expressed as

$$ds^2 = -dt^2 + a(t)^2\left[d\chi^2 + S_K(\chi)^2(\chi)d\Omega^2\right]. \tag{2.9}$$

So far we dealt only with the metric of the spacetime, but in fact we are interested in the effect of matter on the spacetime, especially on the time evolution of the scale factor. To examine this we will use perfect fluids to model the energy sources present in our Universe. We consider the rest frame in which the matter is isotropic and therefore at rest in comoving coordinates and has velocity $U^\mu = (1, 0, 0, 0)$ to write the energy-momentum tensor as

$$T_{\mu\nu} = (p + \rho)U_\mu U_\nu + p g_{\mu\nu}, \tag{2.10}$$

$$T^\mu_{\ \nu} = \text{diag}(-\rho, p, p, p), \tag{2.11}$$

where ρ is the density and p the pressure. To proceed in this topic it is necessary to assume an **equation of state** in oder to close the set of equations. Most sources of energy obey the following simple equation of state

$$p = w\rho. \tag{2.12}$$

The time evolution of the energy density of the different species can be derived from the first component of the energy-momentum conservation

$$\nabla_\mu T^\mu_0 = -\partial_0 \rho - 3\frac{\dot{a}}{a}(\rho + p) \stackrel{!}{=} 0 \Rightarrow \frac{\dot{\rho}}{\rho} = -3(1+w)\frac{\dot{a}}{a}. \tag{2.13}$$

Integrating this equation we obtain for the time dependence of a species described by the equation of state w

$$\rho \propto a^{3(1+w)} \tag{2.14}$$

Using the Einstein field equations we can now derive the **Friedmann equations**

$$\boxed{\frac{\ddot{a}}{a} = -\frac{4\pi G}{3}(\rho + 3p)} \tag{2.15}$$

$$\boxed{\left(\frac{\dot{a}}{a}\right)^2 = \frac{8\pi G}{3}\rho - \frac{K}{a^2}} \tag{2.16}$$

These equations describe the so called **Friedmann-Robertson-Walker Universe**. They can be rendered into a simpler functional form if we introduce the **Hubble parameter**

$$H := \frac{\dot{a}}{a}, \tag{2.17}$$

and the critical density

$$\rho_{\text{crit}} := \frac{3H^2}{8\pi G}. \tag{2.18}$$

All densities can then be rewritten in terms of this critical density using the **density parameter**

$$\Omega_i = \frac{\rho_i}{\rho_{\text{crit}}}. \tag{2.19}$$

The total energy content can then be expressed as

$$\Omega_{\text{tot}} = \Omega_{\text{m}} + \Omega_{\text{r}} + \Omega_\Lambda. \tag{2.20}$$

Using above definition Equation (2.16) reads as

$$\Omega_{\text{tot}} - 1 = \frac{K}{H^2 a^2}. \tag{2.21}$$

So we see that the sign of the spatial curvature is completely determined by the total energy density.
We will now in brevity mention the different sources, which contribute to the energy density of the Universe

dust $w = 0$**:** Collisionless, non-relativistic matter. Universes whose energy density is mainly influenced by dust are called **matter dominated** and the time evolution of the matter is given by $\rho_{\text{m}} \propto a^{-3}$.

radiation $w = 1/3$**:** The energy-momentum tensor $T_{\mu\nu}$ from electrodynamics is traceless and thus we have $\rho_{\text{r}} = 3p_{\text{r}}$. This model can be used for electromagnetic fields or massive particles with $v \approx 1$. A Universe whose energy density is mainly influenced by radiation is known as **radiation dominated**.
The number density of photons decreases in the same way as for massive particles, but the photon energies are suffering from an additional redshift by a^{-1} and we finally obtain $\rho_{\text{r}} \propto a^{-4}$.

vacuum $w = -1$**:** Introducing vacuum energy is equivalent to a **cosmological constant** in Einstein equations and yields $\rho_\Lambda \propto a^0$

$$\rho = -p = \frac{\Lambda}{8\pi G}$$

curvature The curvature can be interpreted as another type of energy and yields

$$\rho_c = -\frac{3K}{8\pi G a^2} \Rightarrow \Omega_c = -\frac{K}{H^2 a^2}$$

In terms of the above defined quantities we can write the second Friedmann equation as

$$H(a)^2 = H_0^2 \left[\Omega_m a^{-3} + \Omega_r a^{-4} + \Omega_\Lambda + \Omega_c a^{-2}\right], \tag{2.22}$$

where H_0 is the present day value of the Hubble parameter. The uncertainty in H_0 is commonly expressed as $H_0 = h$ 100 km s^{-1} Mpc^{-1}. It is useful to consider the analytic solutions which exist for some simple cases with vanishing curvature in order to develop some intuition about the time scales involved. If we have a **radiation dominated** Universe we obtain

$$a \propto t^{1/2} \quad \Rightarrow \quad t = \sqrt{\frac{3}{32\pi G\rho}}, \tag{2.23}$$

whereas in the case of a **matter dominated** Universe, also known as the **Einstein-de-Sitter Universe**, we obtain

$$a \propto t^{2/3} \quad \Rightarrow \quad t = \sqrt{\frac{1}{6\pi G\rho}}. \tag{2.24}$$

A Universe that has an energy content dominated by vacuum-energy or a cosmological constant has

$$a \propto \exp[Ht] \quad \Rightarrow \quad H = \sqrt{\frac{8\pi G\rho}{3}} = \text{const.} \tag{2.25}$$

So we see that vacuum repulsion would cause the Universe to expand infinitely. The general case will not be analytically tractable but numerical solutions do a good job as well.

2.3 The Nature of Redshift

The FRW Universe has no energy conservation but if $U^\mu = (1, 0, 0, 0)$ is the velocity of comoving observers we can write down a conserved **Killing tensor**. Therefore we obtain for a particle with velocity V^μ

$$K_{\mu\nu} = a^2(g_{\mu\nu} + U_\mu U_\nu) \Rightarrow a^2\left[V_\mu V^\mu + (U_\mu V^\mu)^2\right] = \text{const.} = K. \tag{2.26}$$

For photons $V_\mu V^\mu = 0$ and hence

$$U_\mu V^\mu = \frac{K}{a}. \tag{2.27}$$

This is proportional to the frequency measured by an observer given by $\nu = -U_\mu V^\mu$. Hence the frequency between emission and absorption of a light ray changes by

$$\frac{\nu_{\text{obs}}}{\nu_{\text{em}}} = \frac{a_{\text{em}}}{a_{\text{obs}}}. \tag{2.28}$$

The **redshift** between two events is defined by the fractional change in wavelength

$$z = \frac{\lambda_{\text{obs}} - \lambda_{\text{em}}}{\lambda_{\text{em}}} = \frac{a_{\text{em}}}{a_{\text{obs}}} - 1. \tag{2.29}$$

This redshift is different from Doppler effect as it is due to the expansion of space.

2.4 Age of the Universe

As sometimes it is more intuitive to think about times rather than redshifts we calculate the $t(z)$ relationship for a flat ΛCDM Universe with matter density $\Omega_m = 0.25$ and dark energy density $\Omega_\Lambda = 0.75$.

$$t(z) \quad = \quad \int_0^{t(z)} dt' = \int_0^{a(z)} \frac{da'}{\dot{a}'}, \tag{2.30}$$

$$= \int_0^{a(z)} \frac{da'}{Ha'} = \frac{1}{H_0} \int_z^{\infty} \frac{dz'}{(1+z)\sqrt{\Omega_m(1+z')^3+\Omega_\Lambda}} \tag{2.31}$$

In Figure 2.1 we show $t_0 - t(z)$ where $t_0 = 14.15 \times 10^9$ a is the present age of the Universe. Another useful quantity is the relation between comoving distance and redshift which follows from the integration of a radial photon lightpath, the **geodesic distance**:

$$\chi(z) = \int_t^{t_0} \frac{dt}{a} = \frac{1}{H_0} \int_z^1 \frac{dz'}{\sqrt{\Omega_m(1+z')^3+\Omega_\Lambda}}. \tag{2.32}$$

For the Einstein-de-Sitter case we find the analytic expression

$$\chi(z) = \frac{2}{H_0\Omega_m}\left[1 - \frac{1}{\sqrt{1+z}}\right]. \tag{2.33}$$

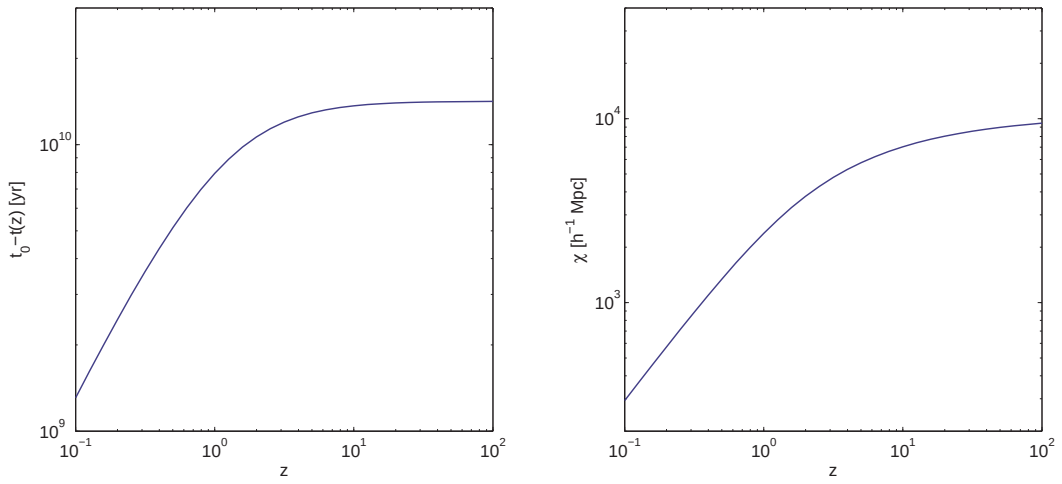

Figure 2.1: *Left panel:* Time from redshift z to present for a ΛCDM Universe *Right panel:* Comoving radial distance to an object at redshift z.

2.5 Luminosity Measures

There is a wide range of luminosities in our Universe and therefore astronomers like to quantify them on a logarithmic scale called the **absolute magnitude**. For an object of luminosity L, the absolute bolometric luminosity is given by

$$M_{\text{bol}} = -2.5 \log\left(\frac{L}{L_\odot}\right) + C_\odot, \tag{2.34}$$

where $L_\odot$ is the solar luminosity and the numerical summand $C_\odot$ is the solar magnitude. The brighter a star or galaxy, the smaller is its absolute magnitude. In most cases only luminosities in a certain spectral range, defined by a filter, will be used. Equivalently flux ϕ can be measured by the **apparent magnitude** on a logarithmic scale

$$m = -2.5 \lg(\phi) + \alpha_C. \tag{2.35}$$

The constant α_C is chosen in a way, such that in absence of absorption absolute magnitude equals apparent magnitude for a source in distance $d = 10$ pc

$$m = M + 5 \lg\left(\frac{d}{10 \text{ pc}}\right) + \alpha_C. \tag{2.36}$$

2.6 Cosmological Distances

There are three different distance measures, which are frequently used in cosmology. First it is important to distinguish between physical distances $r$phys, which are at least principally measurable with a ruler, and comoving distances x_{com}, which give a notion of the distance in a nonexpanding Universe

$$r_{\mathrm{phys}} = a x_{\mathrm{com}}. \tag{2.37}$$

Let us consider a photon travelling in radial direction. We can use the metric (2.9) to see that the comoving distance traveled in time interval dt is $d\chi = dt/a$. By integrating this radial null geodesic $ds^2 = 0$ we obtain the **geodesic distance**

$$\chi(z) = \int \frac{dz'}{H(z')}. \tag{2.38}$$

Often the angle subtended by an object on the sky is measured to estimate its physical size. The **angular diameter distance** is constructed to give an expression equivalent to the well known flat space equation

$$\theta = \frac{q}{D_{\mathrm{A}}}. \tag{2.39}$$

Here q is the physical dimension of the object. From the metric we see that for two points separated by an angle $d\Omega$ we have $dt = aS_k(\chi)d\Omega$. The physical dimension of a small object would be $dl = dt$, since we use units in which $c = 1$. Equating $d\Omega = d\theta$ we see

$$D_{\mathrm{A}} = \frac{S_k(\chi)}{1+z}. \tag{2.40}$$

If we consider an object with luminosity L, the equivalent of the flat space expression for the flux through a sphere with radius D_{L} would be

$$F = \frac{L}{4\pi D_{\mathrm{L}}^2}. \tag{2.41}$$

The area of the sphere in the denominator would be $4\pi S_k(\chi)^2$ and hence one could think of $D_{\mathrm{L}} = S_k(\chi)$. This is however not true, since the photon energies are redshifted by an factor $1/(1+z)$ and the space expands during the travel time from the source to the sphere by another factor of $1/(1+z)$. Hence the flux is $(1+z)^2$ times smaller than expected from the trivial case and we finally obtain the **luminosity distance**

$$D_{\mathrm{L}} = (1+z)S_k(x) = (1+z)^2 D_{\mathrm{A}}(\chi). \tag{2.42}$$

2.7 Cosmological Parameters

Throughout this thesis we use the cosmological parameters which that used for the simulations our investigations rely on. The cosmological parameters for the simulations are inspired by the best fit values released by the WMAP team observing the cosmic microwave background [Spergel *et al.* , 2003, Spergel *et al.* , 2007] and can be taken from Table 2.1.

Ω_{b}	Ω_{dm}	Ω_Λ	h	σ_8	n	w
0.04	0.21	0.75	0.7	0.8	1	-1

Table 2.1: Cosmological parameters adopted throughout this thesis. Baryon density parameter, dark matter density parameter, dark energy density parameter, dimensionless Hubble parameter $H_0 = 100h$ km s^{-1} Mpc^{-1}, power spectrum normalisation, primordial power spectrum slope, dark energy equation of state $p = \omega\rho$.

Tighter constraints of cosmological parameters can be obtained from a combination of observations, as is for instance done by [Seljak *et al.* , 2006] for a combination of WMAP 3 year data, Ly-α forest power spectrum, supernovae and galaxy clustering spectra.

2.8 Dark Matter

One of the main assumptions underlying this thesis is that there exists a non-luminous kind of matter, whose mass however strongly affects the gravitational evolution of the Universe. The study of galaxy dynamics revealed already in in the 1930s that there is a difference between the observed luminous matter content and the mass needed to explain the galaxy dynamics [Raffelt & Murdin, 2002]. Further evidence comes from large scale flows and the flat rotation curves of galaxies. Most importantly the luminous matter present in the Universe can in no way account fro the total matter content of our flat spacetime. While there have been attempts to circumvent this missing mass problem by introducing modifications of general relativity, the most popular explanation is that there is a non-visible or weakly interacting kind of matter.
Basicly one distinguishes baryonic and non-baryonic dark matter candidates. Often the dark matter is further classified in the categories **Hot Dark Matter** (HDM) for candidates that were relativistic at decoupling and **Cold Dark Matter** (CDM) for non-relativistic species. Hot Dark Matter suffers from free-streaming and is strongly disfavoured by structure formation, since it would damp the density contrast too much.
We will now in brevity discuss the most viable dark matter candidates:

axions The smallest mass non-baryonic cold dark matter candidate $m_A \approx 1 \times 10^{-5}$ GeV is a postulate from quantum chromodynamics. Axions would arise from a non-thermal process in the early Universe, producing a Bose condensate. They possess small electromagnetic interactions and could thus drive microwave cavities, which is the most promising approach to detect them.

WIMPs Weakly Interacting Massive Particles (WIMPs) are a standard cold dark matter candidate with $m_{WIMP} > 10$ GeV. Their existence is predicted from a supersymmetric extension of the standard model of particle physics. In this theory the role of the WIMP can be played by the neutralino, the lightest supersymmetric particle. The experimental search for WIMPs mainly focuses on the detection of energy depositions through the rare collisions of a WIMP with a nucleus. These experiments assume that a WIMP aether permeates the whole Milky Way. The DAMA experiment has reported a fluctuation of the WIMP flux during the earth's orbit around the sun [Bernabei *et al.* , 2003]. This result was so far not confirmed by other experiments and is thus heavily discussed.

neutrinos The neutrino is the only yet detected candidate for non-baryonic dark matter. Neutrino oscillation experiments have shown evidence for non-zero neutrino masses and an upper bound of $\sum m_\nu < 0.17$ eV [Seljak *et al.* , 2006] is set from cosmology. Due to the upper bounds on the neutrino mass they fall into the regime of hot dark matter, which leads to some tension with structure formation. Consequently neutrinos can not account for all the required dark matter.

MACHOs Massive Astrophysical Halo Objects (MACHOs) are a baryonic dark matter candidate. They consist of ordinary matter in a non-luminous form, e. g. failed stars, stellar remnants or black holes. The search for MACHOs involves microlensing, the temporary increase of the apparent brightness of stars due to the gravitational light deflection by MACHOs passing close to the line of sight. There has been positive detection of a few objects, yielding $m_{MACHO} \approx 0.5\ M_\odot$. While the opinions about the interpretation of these detections are still divided, it is clear that the MACHOs can in no way account for all the dark matter in the Milky Way.

CHAPTER 3

Linear Growth of Structures

In this chapter we will describe how the nonlinear structures observed today could develop from the very homogeneous and isotropic initial conditions, present at the time of recombination. We will see that this homogeneity is not perfect. There were small inhomogeneities, created during inflation as zero point fluctuations of the inflaton field and then stretched to become classical during the rapid expansion in inflation. The quantum mechanical origin of the fluctuations leads to the cosmological random field, whose evolution will be treated in this chapter.
Structure formation can be treated with Newtonian dynamics on scales small compared to the Hubble scale[1] but on larger scales, especially during inflation, a fully relativistic treatment of the perturbations has to be performed. We will start with some comments on Eulerian and Lagrangian dynamics of the nonrelativistic cosmological fluid, before we turn towards a brief introduction to inflation. Finally, we will develop the formalism of relativistic perturbation theory and apply it to the derivation of the primordial matter power spectrum. To conclude, we comment on the evolution of the latter using transfer functions.

3.1 Newtonian Theory of Structure Formation

We consider our Universe as being composed of an **ideal fluid** characterised by an equation of state, which in most cases can be written as $p = w\rho$. The standard Newtonian equations for a homogeneous fluid are known as the continuity and Euler equations

$$\frac{\partial \rho}{\partial t} + \boldsymbol{\nabla}(\rho \boldsymbol{u}) = 0 \tag{3.1}$$

$$\frac{D\boldsymbol{u}}{Dt} = \frac{d\boldsymbol{u}}{dt} + \frac{d\boldsymbol{x}}{dt} \cdot \nabla \boldsymbol{u} = -\frac{1}{\rho}\boldsymbol{\nabla} p - \boldsymbol{\nabla}\Phi, \tag{3.2}$$

where we defined the convective derivative D/Dt. These equations are supplemented by the Poisson equation, which relates the density to the gravitational potential

$$\Delta\Phi = 4\pi G\rho. \tag{3.3}$$

In a smooth, expanding Universe we have fixed comoving or Lagrangian positions $\boldsymbol{x}$ and time dependent physical coordinates $\boldsymbol{r}$ related by

$$\boldsymbol{r}(t, \boldsymbol{x}) = a(t)\boldsymbol{x}. \tag{3.4}$$

[1] The Hubble scale describes over which distances events can be causally connected.

The particle movement in the smooth case is described by the so called Hubble flow, the linear dependence of the recessional velocity on physical distance

$$\dot{\boldsymbol{r}}(t,\boldsymbol{x}) = \dot{a}(t)\boldsymbol{x} = H\boldsymbol{r}. \tag{3.5}$$

As we know that our Universe is far from being homogeneous on small scales, we will introduce perturbations on the smooth background Universe by [Mukhanov, 2005]

$$\rho(\boldsymbol{x},t) = \bar{\rho}(t) + \delta\rho(t,\boldsymbol{x}), \tag{3.6}$$
$$p(\boldsymbol{x},t) = \bar{p}(t) + \delta p(t,\boldsymbol{x}), \tag{3.7}$$
$$\Phi(\boldsymbol{x},t) = \Phi_b(t) + \delta\Phi(t,\boldsymbol{x}). \tag{3.8}$$

We will generally assume **adiabatic initial conditions**, i.e. the fluctuations in the photon density follow the fluctuations in the matter density. In this context it is convenient to introduce a dimensionless **overdensity**

$$\delta := \frac{\rho(\boldsymbol{x})}{\bar{\rho}} - 1. \tag{3.9}$$

By perturbing the homogeneous fluid, initially static comoving positions now become time dependent.

$$\boldsymbol{r}(t,\boldsymbol{x}) = a(t)\boldsymbol{x}(t) \tag{3.10}$$

The time dependent comoving position leads to an additional term in the physical velocity

$$\dot{\boldsymbol{r}}(t,\boldsymbol{x}) = \boldsymbol{u}(t,\boldsymbol{x}) = H\boldsymbol{r} + a\dot{\boldsymbol{x}} = H\boldsymbol{r} + \boldsymbol{v}. \tag{3.11}$$

In the last line we split the particle velocity in one part following Hubble flow and the **peculiar velocity** $\boldsymbol{v}$, which a uniform expansion observer would now measure for the comoving observer. The Newtonian restframe is defined as the frame where the spatial average over $\boldsymbol{v}$ vanishes. Today this restframe is determined by the matter content rather than the radiation. The acceleration of the comoving observer reads as

$$\frac{d\boldsymbol{u}}{dt} = \ddot{a}\boldsymbol{x} + \boldsymbol{g}. \tag{3.12}$$

Here $\boldsymbol{g}$ refers to the peculiar acceleration, which is given by

$$\boldsymbol{g} = \frac{d\boldsymbol{v}}{dt} + H\boldsymbol{v} = \frac{1}{a}\frac{d(a\boldsymbol{v})}{dt} \tag{3.13}$$

The Euler equation relates the acceleration to pressure and gravitational potential

$$\frac{d\boldsymbol{u}}{dt} = -\frac{1}{\rho}\boldsymbol{\nabla}p - \boldsymbol{\nabla}\Phi \tag{3.14}$$

It is convenient to express all spatial derivatives w.r.t. the comoving position $\boldsymbol{x}$ and to subtract out the fluid equations valid for the homogeneous background. To do this we have to consider the following relation when rewriting partial derivatives

$$\left.\frac{\partial f(\boldsymbol{r}=a\boldsymbol{x},t)}{\partial t}\right|_{\boldsymbol{x}} = \left.\frac{\partial f(\boldsymbol{r}=a\boldsymbol{x},t)}{\partial t}\right|_{\boldsymbol{r}} + \dot{a}\boldsymbol{x}\cdot\boldsymbol{\nabla}_{\boldsymbol{r}}f. \tag{3.15}$$

Furthermore, we can use conformal time defined by $ad\tau = dt$. This yields mass conservation, Euler and Poisson equation for the perturbed Universe[2]

$$\frac{\partial\delta}{\partial\tau} + \boldsymbol{\nabla}\cdot\big[\boldsymbol{v}(1+\delta)\big] = 0, \tag{3.16}$$

[2] In this chapter we will use the prime to denote derivatives w.r.t. conformal time and conformal Hubble parameter defined as

$$\mathcal{H} = \frac{1}{a}\frac{da}{d\tau} = \frac{da}{dt} = aH.$$

$$\frac{\partial \boldsymbol{v}}{\partial \tau} + \mathcal{H}\boldsymbol{v} + \boldsymbol{v}\,(\boldsymbol{\nabla}\cdot\boldsymbol{v}) = -c_s^2\boldsymbol{\nabla}\delta - \boldsymbol{\nabla}\delta\Phi, \tag{3.17}$$

$$\Delta\delta\Phi = 4\pi\bar{\rho}a^2\delta. \tag{3.18}$$

Here we neglected entropy perturbations and used $\delta p = c_s^2\delta\rho$. To proceed, we linearise above equations, noting that the linearised equations will only be valid as long as the density perturbations are well into the linear regime. Expansions to higher order are necessary to follow the perturbations into the non-linear regime.
Neglecting pressure on scales larger than the **Jeans scale**[3], we can derive the following equation:

$$\boxed{\delta'' + \mathcal{H}\delta' - 4\pi G a^2\bar{\rho}\delta = 0} \tag{3.19}$$

Here primes denote differentiation w.r.t. conformal time and the Laplacian is w.r.t. comoving coordinates. This is a linear differential equation of second order and has a growing and a decaying solution, such that the general solution can be written as a linear combination of both

$$\delta(\tau) = c_1 D_1(\tau) + c_2 D_2(\tau), \tag{3.20}$$

with D_1 and D_2 given by

$$D_1(\tau) = \frac{5}{2}\Omega_m H(\tau)\int_0^{a(\tau)} \frac{d\tilde{a}}{(\tilde{a}H)^3} \qquad D_2(\tau) = H(\tau). \tag{3.21}$$

A common assumption is that the perturbations observed today are influenced by the growing mode only. Perturbations were extremely small after recombination and hence the decaying mode has vanished. Often one refers to $D_1(\tau)$ as the **linear growth factor**.
In a flat, purely matter dominated Universe ($\Omega_m = 1$), usually termed **Einstein-de-Sitter Universe**, we have $a \propto t^{2/3} \propto \tau^2$ and hence

$$D_1 = \tau^2 \propto t^{2/3}, \qquad D_2 = \tau^{-3} \propto t^{-1}. \tag{3.22}$$

Peculiar Velocities

We can write down the linearised continuity equation (3.16) in Fourier space

$$\tilde{\delta}' + i\boldsymbol{k}\cdot\tilde{\boldsymbol{v}} = 0. \tag{3.23}$$

In linear theory vorticity decays as $1/a$. As long as there is no process which generates vorticity the peculiar velocity can be written as the gradient of a potential, leading to $\boldsymbol{v} \parallel \boldsymbol{k}$. At late times the matter density contrast scales with the growing mode $D_1(\tau)$ and hence

$$|\boldsymbol{v}| = \frac{i}{k}\frac{d}{d\tau}\left(\frac{\tilde{\delta}}{D_1}D_1\right) = \frac{i\tilde{\delta}}{kD_1}\frac{dD_1}{d\tau} = \frac{i\tilde{\delta}\mathcal{H}}{k}\frac{d\ln D_1}{d\ln a} = \frac{i\tilde{\delta}\mathcal{H}f}{k}. \tag{3.24}$$

In the last equality we introduced the **logarithmic growth factor** $f \approx \Omega_{\mathrm{m}}^{6/11}$ and in a flat Universe with cosmological constant Ω_{m} scales as

$$\Omega_{\mathrm{m}}(z) = \left(1 + \frac{1-\Omega_{\mathrm{m},0}}{\Omega_{\mathrm{m},0}}\frac{1}{(1+z)^3}\right)^{-1} \tag{3.25}$$

where $\Omega_{\mathrm{m},0}$ is the matter density at $z = 0$.

[3] The Jeans scale basically separates small scales dominated by pressure forces from large scales dominated by gravity.

3.2 Lagrangian Description of Structure Formation - Zeldovich Approximation

In Lagrangian dynamics one considers the change of particle position with time rather than continuum quantities such as pressure or density at a fixed location. Hence we have to solve the particle equation of motion in comoving coordinates

$$\boldsymbol{x}'' + \mathcal{H}\boldsymbol{x}' = -\boldsymbol{\nabla}_{\boldsymbol{x}}\delta\Phi. \tag{3.26}$$

As the perturbations were small at recombination, it is valid to assume that only the growing mode solution of (3.19) is present today

$$\delta(\boldsymbol{x}, \tau) = D_1(\tau)\delta_0(\boldsymbol{x}). \tag{3.27}$$

Substituting this into Poisson equation implies that gravitational potential scales as

$$\delta\Phi = \frac{D}{a}\delta\Phi_0, \tag{3.28}$$

which can be used to integrate (3.26) twice in time.

$$\boldsymbol{x}' = -\frac{1}{a}\int_0^\tau d\tilde{\tau} D(\tilde{\tau})\boldsymbol{\nabla}\delta\Phi_0, \tag{3.29}$$

$$\boldsymbol{x} = \boldsymbol{x}_0 - \int_0^\tau \frac{d\tilde{\tau}}{a(\tilde{\tau})}\int_0^{\tilde{\tau}} D(\tilde{\tilde{\tau}})d\tilde{\tilde{\tau}}\boldsymbol{\nabla}\delta\Phi_0. \tag{3.30}$$

The growth factor satisfies the linear growth equation (3.19) and hence we have

$$D = \frac{(aD')'}{4\pi G\bar{\rho}a^3}. \tag{3.31}$$

Note that the denominator is constant and the integration of (3.29) and (3.30) is readily done by evaluation of above expression at the boundaries

$$\boldsymbol{x} = \boldsymbol{x}_0 - \frac{\boldsymbol{\nabla}\delta\Phi}{4\pi G\bar{\rho}a^2}, \qquad \boldsymbol{v} = -\frac{1}{4\pi G\bar{\rho}a^2}\frac{aD'}{D}\boldsymbol{\nabla}\delta\Phi. \tag{3.32}$$

In the derivation of above result we used the validity of the linear growth equation. This assumption is no longer valid when the overdensities enter the non-linear regime. Zeldovich proposed in 1970 that above result should be applicable also in the weakly non-linear regime, an assumption which was christened the **Zeldovich approximation**. When the particle trajectories in Eulerian space cross, i.e. when particles with different Lagrangian positions get mapped to the same position in real space, the Lagrangian description breaks down.
Using Zeldovich approximation and conservation of mass one can infer to the first structures that will form in the Universe. It turns out that the first structures are sheetlike.
The Zeldovich approximation is often written in the form

$$\boldsymbol{x}(a, \boldsymbol{q}) = \boldsymbol{q} + \boldsymbol{L}(\boldsymbol{q}, a). \tag{3.33}$$

Here $\boldsymbol{q}$ denotes the initial Lagrangian position of a particle and $\boldsymbol{L}$ is the displacement, whose functional form we derived above.
Once calculated the density field at the starting time of a simulation, one needs to set up particle positions and velocities. One approach to generate the initial conditions for large N-body dissipationless simulations is to put the N_p particles on a Cartesian grid with grid spacing $\Delta x = (V/N_\mathrm{p})^{1/3}$, where V is the volume, and displace them according to Zeldovich approximation [Bertschinger, 1998].

3.3 Inflation in a Nutshell

Inflation was proposed by [Guth, 1981] to account for the large scale homogeneity and horizon problem present in the big bang paradigm. He argued that shortly after **big bang** the Universe must undergo an epoch of accelerated expansion $\ddot{a} > 0$ which should be over at $t \approx 10^{-34}$ s. During this expansion the comoving Hubble length $1/\mathcal{H}$ decreases with time while the metric approaches that of a flat isotropic Robertson-Walker Universe. From the first Friedmann equation (2.15) one immediately sees that the field driving inflation needs to come along with negative pressure.
The easyest model of inflation is based on a Universe dominated by a single scalar field ϕ, the **inflaton field**. From the Lagrangian of the inflaton field one can derive pressure and density

$$p_\phi = \frac{1}{2}\dot{\phi} - V(\phi), \qquad \rho_\phi = \frac{1}{2}\dot{\phi} + V(\phi), \tag{3.34}$$

where V is the potential of the scalar field. The equation of motion is the Klein-Gordon equation, that in an expanding Universe has an additional friction term

$$\ddot{\phi} + 3H\dot{\phi} + V_{,\phi}(\phi) = 0, \tag{3.35}$$

inflation stretches all lengths exponentially $\ln(a_\mathrm{f}/a_\mathrm{i}) \approx 75$, where a_i and a_f are the expansion factors at begin and end of inflation, respectively. When a mode with comoving wavelength $1/k$ becomes comparable to the comoving Hubble length $1/\mathcal{H}$, it will cross the **horizon**[4] and will remain unchanged until it reenters the horizon after the end of inflation.
One of the easyest inflationary models, **slow roll inflation**, states that the scalar field approaches the minimum of its potential by slowly rolling down the potential. The first slow roll parameter describes the deviations from the de Sitter case $w_\phi = p_\phi/\rho_\phi = -1$

$$\epsilon = \frac{3}{2}(1 + w_\phi) = 4\pi G \left(\frac{V_{,\phi}}{V}\right)^2. \tag{3.36}$$

The slowly rolling field has to satisfy $\dot{\phi} \ll 1$, which is described by the second slow roll parameter

$$\eta = \frac{d^2\phi}{dt^2} = \frac{\phi''}{\mathcal{H}\phi'} - 1 = 8\pi G \frac{V_{,\phi\phi}}{V}. \tag{3.37}$$

Successfull inflation requires $\epsilon \ll 1$ and $\eta \ll 1$. At the end of inflation the scalar field starts to oscillate and by doing so, it loses its energy and creates particles. To lowest order in the slow roll parameters we have

$$\epsilon = \frac{3\dot{\phi}^2}{2a^2V}, \qquad \dot{\phi} = -\frac{a^2 V_\phi}{3\mathcal{H}}. \tag{3.38}$$

3.4 Cosmological Perturbation Theory

In the above discussion we assumed that after recombination small density fluctuations were present in all components but did not say much about their creation. Besides the Gaussian fluctuations generated by Inflation, there are also non-Gaussian fluctuations, predicted for instance by topological defects. We will neglect the latter and assume that inflation is the valid physical model to describe the early phase of the Universe.
In order to calculate the spectrum of the density fluctuations we have to use a fully relativistic approach, where deviations from homogeneity are described by small perturbations around the flat Robertson-Walker background metric $\eta_{\mu\nu}$

$$g_{\mu\nu} = \eta_{\mu\nu} + h_{\mu\nu}. \tag{3.39}$$

[4] The horizon scale determines over which distances physical processes can be in causal contact at a given cosmological time and is usually of order $\mathcal{H}^{-1}$.

Following the notation of [Liddle & Lyth, 2000, Seljak, 2000b] we can write down the **perturbed metric** as

$$ds^2 = a^2(\tau)\left[-(1+2A)\,d\tau^2 - 2B_i dx^i d\tau + ((1+2D)\delta_{ij} + 2E_{ij})\,dx^i dx^j\right]. \tag{3.40}$$

Here we decomposed the metric perturbations into time, space and mixed time space component, where E_{ij} is the traceless part of the spatial perturbation and D is its trace. We will in the following only consider the scalar part of a scalar-vector-tensor decomposition of the perturbations [Seljak, 2000b], and denote the scalar parts of the above introduced perturbations as A, B, D and E. To write down the Einstein equations, we have to consider the following energy momentum tensor (EMT)

$$T^{\mu\nu} = (\rho + p)u^\mu u^\nu + pg^{\mu\nu} + \Sigma^{\mu\nu}, \tag{3.41}$$

where $\Sigma^{\mu\nu}$ is the anisotropic stress. There is no longer a preferred coordinate system if we go over to a perturbed Universe. We did not yet specify a specific **gauge** for the coordinates used in (3.40) but have rather chosen an arbitrary coordinate system applicable throughout the whole space-time.
We can furthermore define density and pressure perturbation as

$$\rho(\tau, x_i) = \bar{\rho}(\tau) + \delta\rho(\tau, x_i), \qquad p(\tau, x_i) = \bar{p}(\tau) + \delta p(\tau, x_i). \tag{3.42}$$

Gauge transformations can be described as first order changes ξ^μ in the coordinates

$$\tilde{x}^\mu = x^\mu + \xi^\mu, \tag{3.43}$$

which can be split up into time and space part

$$\tilde{x}^0 = x^0 + T(x^\mu), \qquad \tilde{x}^i = x^i + L^i(x^\mu). \tag{3.44}$$

The line element has to be conserved under this transformation and hence we can write down the transformation law of a general tensor under this change of coordinates

$$\tilde{Q}_{\mu\nu}(\tilde{x}^\gamma) = \frac{\partial x^\alpha}{\partial \tilde{x}^\mu}\frac{\partial x^\beta}{\partial \tilde{x}^\nu} Q_{\alpha\beta}(\tilde{x}^\gamma - \xi^\gamma). \tag{3.45}$$

This leads to

$$\delta\tilde{\rho} = \delta\rho - \rho' T, \tag{3.46}$$
$$\delta\tilde{p} = \delta p - p' T, \tag{3.47}$$
$$\tilde{v} = v + L'. \tag{3.48}$$

The scalar field which will be the driving force of inflation transforms as

$$\delta\tilde{\phi} = \delta\phi - \phi' T. \tag{3.49}$$

3.5 Popular Gauge Choices

To proceed in our goal of deriving the spectrum of fluctuations from inflation we have to use a convenient gauge. The discussion presented here is based on [Seljak, 2000b] and is not thought as a formal derivation but rather as a rough guideline.

Newtonian Gauge

This gauge is defined by $\tilde{B} = \tilde{E} = 0$. We rename the remaining two scalar perturbations $A \to \Psi$ and $D \to -\Phi$. There is no remaining gauge ambiguity, i.e. the gauge is completely fixed by the transformation

$$L = -\frac{E}{k}, \qquad T = -\frac{B}{k} + \frac{E'}{k^2}, \tag{3.50}$$

where B and E are evaluated in an arbitrary gauge. Some important equations following from the Einstein field equations are

$$(-k^2+3K)\Phi = 4\pi G a^2\left[3\mathcal{H}(\bar{\rho}+\bar{p})\frac{v}{k}+\delta\rho\right], \tag{3.51}$$

$$\Phi'+\mathcal{H}\Phi = 4\pi G a^2(\bar{\rho}+\bar{p})\frac{v}{k}, \tag{3.52}$$

$$k^2(\Phi-\Psi) = 8\pi G a^2\Sigma. \tag{3.53}$$

On small scales we can neglect the curvature K on the lhs as well as the first term on the rhs of the first equation to obtain a Poisson equation for the expanding Universe

$$-k^2\Phi = 4\pi G a^2\delta\rho. \tag{3.54}$$

The metric then reduces to the form

$$ds^2 = a^2\left\{-(1+2\Psi)d\tau^2+(1-2\Phi)dx_i dx_j\right\} \tag{3.55}$$

In the absence of anisotropic stress we furthermore have $\Phi=\Psi$.

Comoving Gauge

This gauge is very useful in the calculation of the primordial perturbations and is defined such that the momentum density T^0_i vanishes. We have one further gauge freedom, which we use to set $\tilde{E}=0$ and get the following transformation

$$L=-\frac{E}{k}, \qquad T=\frac{v-B}{k}. \tag{3.56}$$

The two remaining scalar perturbations are renamed as $A\to\xi$ and $D\to\mathcal{R}$, where $\mathcal{R}$ is known as the **curvature perturbation**. We quote only two Einstein and one conservation equation for later use

$$(k-3K)(\mathcal{R}+\mathcal{H}v_{com}/k) = 4\pi G a^2\delta\rho_{com}, \tag{3.57}$$

$$\mathcal{H}\xi-\mathcal{R}' = \frac{K}{k}v, \tag{3.58}$$

$$(\bar{\rho}+\bar{p})\xi = -\delta p+\frac{2}{3}\left(1-3\frac{K}{k^2}\right)\Sigma. \tag{3.59}$$

Spatially Flat Gauge

This gauge will prove to be very convenient to calculate scalar field perturbations which vanish in comoving gauge. The gauge is fixed by $\tilde{E}=0$ and $\tilde{D}=0$. The scalar field equation simplifies if we neglect all terms proportional to the slow roll parameters

$$\delta\phi''+2\mathcal{H}\delta\phi'+k^2\delta\phi=0. \tag{3.60}$$

3.6 Perturbations from Inflation

We already noted that the concept of inflation can account both for the horizon and the flatness problem. Another important advantage of having inflation in the early Universe is that it can produce the seeds for structure formation in the Universe. These fluctuations arise as zero point fluctuations of a scalar field and are then stretched by the exponential expansion to become classical at horizon crossing. As a first step we will consider the relation between Newtonian potential Φ and curvature perturbation $\mathcal{R}$

$$\delta\rho_{\rm com}=\delta\rho_{\rm N}-\rho'_{\rm N}T_{\rm N\to com}=\delta\rho_N+3\mathcal{H}(\bar{\rho}+\bar{p})\frac{v_N}{k}, \tag{3.61}$$

where we used continuity equation $\bar{\rho}' = -3\mathcal{H}(\bar{\rho} + \bar{p})$.
Using (3.51) and furthermore neglecting curvature K leads to

$$-k^2\Phi = 4\pi G a^2 \delta\rho_{\text{com}}. \tag{3.62}$$

With the Poisson equation in comoving gauge (3.57) we can derive

$$\mathcal{R} + \mathcal{H}\frac{v_{\text{com}}}{k} = \Phi. \tag{3.63}$$

In Newtonian gauge $E = 0$ and hence $L_{N\to\text{com}} = 0$. This implies $v_{\text{com}} = v_{\text{N}} + L'_{N\to\text{com}} = v_{\text{N}}$.

$$\mathcal{R} = \Phi - \frac{2}{3}\frac{\mathcal{H}^{-1}\Phi + \Psi}{1+\omega} \tag{3.64}$$

Here we used (3.51) and the Friedmann equation for the smooth background

$$\mathcal{H} = \frac{8\pi G a^2}{3}\bar{\rho}. \tag{3.65}$$

If we furthermore neglect anisotropic stress $\Sigma = 0$ for a Universe dominated by ideal fluids, we obtain $\Phi = \Psi$ and hence

$$\Phi = \frac{3+3\omega}{5+3\omega}\mathcal{R}. \tag{3.66}$$

We can now use above results to show that curvature perturbation is constant outside horizon. To do so, we rewrite the evolution and conservation equations for the curvature perturbation (3.57) and (3.58) to yield

$$\mathcal{R}' = \mathcal{H}\xi = -\frac{\mathcal{H}\delta p_{\text{com}}}{\bar{\rho} + \bar{p}} \tag{3.67}$$

We will now show that this quantity is very small outside horizon, i.e. for $k/\mathcal{H} \to 0$. Assuming vanishing entropy perturbation, we have $\delta p_{\text{com}} = c_s^2 \delta\rho_{\text{com}}$ and equation (3.62) as well as (3.67) lead to

$$\mathcal{R}' = \frac{c_s^2 k^2 \mathcal{H}\Phi}{4\pi G a^2(\bar{\rho}+\bar{p})} = \left[\frac{k}{\mathcal{H}}\right]^2 \frac{2\mathcal{H}c_s^2\mathcal{R}}{5+3\omega}. \tag{3.68}$$

So we in fact see, that $\mathcal{R}'$ vanishes outside horizon and hence $\mathcal{R} = \text{const}$.
We now want to calculate the spectrum of the metric perturbation that are produced by the scalar field driving inflation. To calculate these zero point fluctuations we have to transform to spatially flat gauge, since the scalar field fluctuation vanishes in comoving gauge. This implies for any transformation to comoving gauge

$$0 = \tilde{\delta\phi}_{\text{com}} = \delta\phi - T_{\text{flat}\to\text{com}}\phi'_{\text{flat}} \Rightarrow T_{\text{flat}\to\text{com}} = \frac{\delta\phi}{\phi'}. \tag{3.69}$$

The sense of using the spatially flat gauge becomes obvious when writing down the equation which relates the curvature perturbation to the scalar field

$$\mathcal{R} = D - \frac{k}{3}L - \mathcal{H}T = D + \frac{E}{3} - \mathcal{H}T_{\text{flat}\to\text{com}} = -\mathcal{H}\frac{\delta\phi}{\phi'}. \tag{3.70}$$

Now that we know how to calculate the curvature perturbation from the scalar field we can derive the actual fluctuations. As already noted, the evolution equation for the scalar field simplifies if we assume slow roll inflation and neglect all terms proportional to the slow roll parameters

$$\delta\phi'' + 2\mathcal{H}\delta\phi'' + k^2\delta\phi = 0. \tag{3.71}$$

Introducing $y = a\delta\phi$ we can simplify this to obtain

$$y'' + \left(k^2 - 2\mathcal{H}^2\right) y = 0. \tag{3.72}$$

On small scales the term proportional to k^2 will dominate and we obtain an harmonic oscillator equation, which can be quantised using creation $\hat{a}^\dagger$ and annihilation operators $\hat{a}$ with the usual bosonic commutation relations. A general state is descried by a superposition of both operators

$$\hat{y} = \lambda(k)\hat{a} + \lambda^\dagger(k)\hat{a}^\dagger. \tag{3.73}$$

We can now calculate the variance of the ground state for the harmonic oscillator by calculating the expectation values in the vacuum

$$\left\langle \hat{y}\hat{y}^\dagger \right\rangle - \left\langle \hat{y} \right\rangle^2 = \left\langle 0|\hat{y}\hat{y}^\dagger|0 \right\rangle = |\lambda_k|^2 . \tag{3.74}$$

The classical solution to equation (3.73) is given by

$$\lambda(k) = \frac{1}{\sqrt{2k}}\left(1 - \frac{i\mathcal{H}}{k}\right)\exp\left[-i\frac{k}{\mathcal{H}}\right], \tag{3.75}$$

which has small $k/\mathcal{H} \to \infty$ and large scale $k/\mathcal{H} \to 0$ limits

$$|\lambda_k| = \frac{1}{\sqrt{2k}}, \qquad\qquad |\lambda_k| = \frac{\mathcal{H}}{\sqrt{2k^3}}. \tag{3.76}$$

Since we are interested in the classical solution after horizon crossing, we can use the large scale limit and (3.70) to obtain

$$\mathcal{R} = \frac{-i\mathcal{H}^2}{\sqrt{2k^3}a\phi'}. \tag{3.77}$$

From this quantity we can derive the variance or **power spectrum**[5] of the curvature fluctuation

$$\Delta^2_{\mathcal{R}}(k) = \frac{k^3\left|\mathcal{R}\right|^2}{2\pi^2} = \frac{G}{\pi\epsilon}\left(\frac{\mathcal{H}}{a}\right)^2, \tag{3.78}$$

where we used $4\pi G\phi'^2 = \epsilon\mathcal{H}^2$. Since the Hubble parameter $H = \mathcal{H}/a$ is approximately constant during inflation the variance is almost scale invariant. Furthermore we derived above that the curvature perturbation is frozen outside the horizon. The reason for this scale independence is that the perturbations cross horizon very fast and no physical processes can imprint their scale.
Relating the logarithmic derivative of $\Delta^2_{\mathcal{R}}$ at horizon crossing $k/\mathcal{H} = 1$ to the slow roll parameters we can derive the slope

$$\left.\frac{d\ln\Delta^2_{\mathcal{R}}}{d\ln k}\right|_{k=\mathcal{H}} = n - 1 = -4\epsilon - 2\eta. \tag{3.79}$$

This guides us to make an power law ansatz for the power spectrum

$$\Delta^2_{\mathcal{R}} \propto k^{n-1}. \tag{3.80}$$

The value $n = 1$ is predicted by slow roll inlfation $\epsilon \ll 1, \eta \ll 1$ and corresponds to the Harrison-Zeldovich or **scale free spectrum**. To calculate the actual density perturbation in Newtonian gauge during matter domination $w = 0$ we simply use Poisson equation $-k^2\Phi = 4\pi G a^2\bar{\rho}\delta_k = \frac{3}{2}\mathcal{H}^2\delta_k$

$$\delta_k = -\frac{2}{3}\left(\frac{k}{a\mathcal{H}}\right)^2\Phi_k = \frac{2}{5}\left[\frac{k}{\mathcal{H}}\right]^2\mathcal{R}. \tag{3.81}$$

Hence the power spectrum of the density fluctuations is given by

$$\Delta^2_\delta = \frac{4}{25}\left[\frac{k}{\mathcal{H}}\right]^4\Delta^2_{\mathcal{R}} \quad \Rightarrow \quad P(k) \propto k. \tag{3.82}$$

[5]There are two definitions of the power spectrum in the literature. We will mainly use the definition $P(k) = \left\langle|\delta(\boldsymbol{k})|^2\right\rangle$, which is related to the definition used here as $P(k) = 2\pi^2\Delta^2(k)/k^3$

3.7 Evolution of the Primordial Spectrum

In the last section we developed an understanding of the shape of the perturbations at the moment when a mode crosses the horizon. We saw that the modes outside horizon do not grow both in matter and in radiation domination. But modes entering during radiation domination will grow as $\delta \propto \ln \tau$, whereas during matter domination the growth scales as $\delta \propto \tau^2$. So the amplitude of small scale (high k) modes entering during radiation domination will be suppressed compared to the modes entering only after matter radiation equality. A convenient way to express how the amplitude of a certain mode changes by the cosmological evolution is the **transfer function**

$$T(k,\tau) = \frac{\delta(k,\tau)}{\delta(k,\tau_{\mathrm{e}})}. \tag{3.83}$$

Here we used τ_{e} to denote the time of horizon entry, given by $\tau_{\mathrm{e}} \propto k^{-1}$. The processed power spectrum then is given by

$$P(k,\tau) = T^2(k,\tau)P(k,\tau_e). \tag{3.84}$$

The transfer function will be close to unity on large scales and suppressed for small scales. We show the transfer function calculated for the cosmology under consideration in our simulations in Figure 3.1.

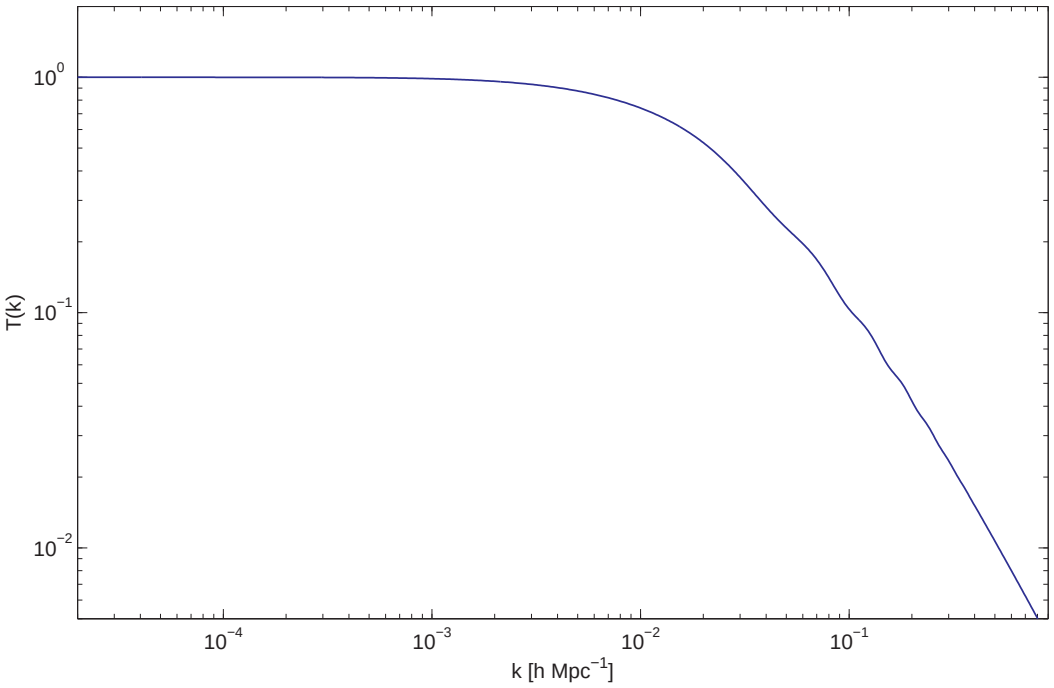

Figure 3.1: The transfer function as computed with `CMBFAST` for the cosmology under consideration in our work. We clearly see the baryon acoustic oscillations imprinted by the strongly coupled baryon photon fluid.

The reason for the different growth rates is that the species present in the Universe are not evolving independently after horizon crossing and have to be described by the Boltzmann equations, a coupled set of differential equations describing the densities and distribution functions of the relativistic and nonrelativistic species. There are fitting functions for $T(k)$ in the literature but we decide to use `CMBFAST` [Seljak & Zaldarriaga, 1996] to find a numerical solution. We will compare measured power spectra to the matter power spectrum predicted by slow roll inflation

$$P_l(k) = Ak^n \tag{3.85}$$

Using the transfer function we calculate the normalisation A of the power spectrum by demanding for the right root mean square overdensity within spheres of $R = 8h^{-1}\text{Mpc}$

$$\sigma_R^2 = \frac{4\pi V}{(2\pi)^3} \int dk A k^3 T^2(k) \left|\hat{W}_R(k)\right|^2 . \tag{3.86}$$

Here $\hat{W}_R(k)$ is the Fourier transform of the top hat window function. For the simulation we used $\sigma_8 = 0.8$ and obtain a normalisation of $A = 5.05 \times 10^6/V$.

CHAPTER 4

Statistics

The Universe we live in was seeded by quantum fluctuations, which became classical during inflation and grew by the subsequent evolution to form the highly nonlinear structures we observe today. As a consequence of this quantum mechanical origin, the structures are stochastic with random initial conditions. Due to this fact we can not hope to develop a theory that exactly reproduces the Universe we observe today. Rather, we should consider our Universe as one representation of an ensemble of possible Universes. Therefore, we need to introduce statistical quantities, which can be used to compare theoretical predictions with the observed data.

4.1 Correlation Functions

Starting from a smooth matter density field $\rho(\boldsymbol{r})$ we can define a dimensionless **overdensity** or **density contrast**

$$\delta(\boldsymbol{r}) = \frac{\rho(\boldsymbol{r}) - \bar{\rho}}{\bar{\rho}}, \tag{4.1}$$

which satisfies $\langle \delta(\boldsymbol{r}) \rangle = 0$ and should be homogeneous and isotropic in a statistical sense. Here statistical homogeneity means that all multipoint moments remain invariant under coordinate translations, whereas statistical isotropy states that the latter will be true for coordinate rotations. The brackets stand for an averaging process, which can be understood either as an ensemble average over many possible realisations of the Universe or as a spatial average considering all $\boldsymbol{x}$ of the Universe. That these two averages are equivalent is not trivial. But we can assume that points that are far away from each other in the Universe are not causally connected and therefore we can use averages over widely separated regions as an approximation for independent realisations [Peacock, 1999].[1]
It will prove convenient to build up the actual density field from a superposition of modes that describe the behaviour on a certain scale. We therefore consider a finite box of volume V with periodic boundary conditions.
We introduce the following Fourier convention:

$$\hat{\delta}(\boldsymbol{k}) = \frac{1}{V} \int d^3 r \exp\left[i\boldsymbol{k} \cdot \boldsymbol{r}\right] \delta(\boldsymbol{r}), \tag{4.2}$$

$$\delta(\boldsymbol{r}) = \frac{V}{(2\pi)^3} \int d^3 k \exp\left[-i\boldsymbol{k} \cdot \boldsymbol{r}\right] \hat{\delta}(\boldsymbol{k}). \tag{4.3}$$

[1] Fields which satisfy the property that volume average is equivalent to ensemble average are termed ergodic in statistical physics.

One of the most important clustering statistics is the **two-point autocorrelation function**, defined as

$$\xi(\boldsymbol{r}) = \langle \delta(\boldsymbol{x})\delta(\boldsymbol{x}+\boldsymbol{r})\rangle\,. \tag{4.4}$$

Due to statistical isotropy the two point correlation only depends on the magnitude of the separation $\xi(\boldsymbol{r}) = \xi(|\boldsymbol{r}|)$. Noting that $\delta(\boldsymbol{r})$ is a real quantity and using (4.3) in above equation one can easily derive

$$\xi(\boldsymbol{r}) = \frac{V}{(2\pi)^3}\int d^3k \left|\hat{\delta}(\boldsymbol{k})\right|^2 \exp\left[-i\boldsymbol{k}\cdot\boldsymbol{r}\right]. \tag{4.5}$$

Here we used the Hermitian property of Fourier transforms of real fields $\hat{\delta}(-\boldsymbol{k}) = \hat{\delta}^{\dagger}(\boldsymbol{k})$. We see that the correlation function is just the Fourier transform of the **power spectrum** defined as

$$\langle \delta(\boldsymbol{k})\delta(\boldsymbol{k}')\rangle = \delta^D(\boldsymbol{k}-\boldsymbol{k}')P(k), \tag{4.6}$$

where $\delta^D(\boldsymbol{k})$ is the Dirac-Delta distribution. The power spectrum is in turn related to the correlation function by

$$P(k) = \frac{1}{V}\int d^3r\xi(r)\exp\left[i\boldsymbol{k}\cdot\boldsymbol{r}\right] = \frac{4\pi}{V}\int dr\xi(r)r^2 j_0(kr), \tag{4.7}$$

where $j_0(kr) = \sin(kr)/kr$ refers to the spherical Bessel function of order 0.

4.2 Filtering of the Density Field

As we are not only interested in the local properties of perturbations, but also in averages over a certain volume, we can convolve the density field with a filter $W(R)$ of scale R. This convolution in real space translates into a simple multiplication in Fourier space.
The variance of the smoothed density field is given by

$$\sigma_R^2 = \frac{V}{(2\pi)^3}\int d^3k P(k)\left|\hat{W}_R(k)\right|^2 = \left\langle \delta_R(\boldsymbol{x})^2\right\rangle. \tag{4.8}$$

Often one considers the Fourier transform of the **top hat filter** with radius R

$$\hat{W}_R(k) = 3\left[\frac{\sin(kR)}{(kR)^3} - \frac{\cos(kR)}{(kR)^2}\right]. \tag{4.9}$$

This function gives notable contributions only for $|k| \leq \frac{4.5}{R}$. Note that the scale of the filter is related to a typical mass by the relation

$$M = \frac{4\pi}{3}R^3\bar{\rho}. \tag{4.10}$$

The quantity σ_8 is the root mean square (rms) density fluctuation in spheres of radius 8 h^{-1}Mpc and is often used to normalise the power spectrum. Figure 4.1 shows the rms overdensity in spheres of radius R and mass M for the cosmology under consideration.

4.3 Two-Point Probability Distribution

An alternative interpretation of the correlation function defined above can be found in terms of the multi-point probability distribution functions [Peebles, 1980]. We will consider the background density field to be traced by a certain species with number density $\bar{n}$ and consider small volumes δV, which either host or don't host one tracer particle. If we had a purely random field the probability of finding particles both in volumes δV_1 and δV_2 separated by $r_{12} = |\boldsymbol{x}_1 - \boldsymbol{x}_2|$ would be given by the product of the independent probabilities

$$\delta P = \bar{n}^2\delta V_1\delta V_2. \tag{4.11}$$

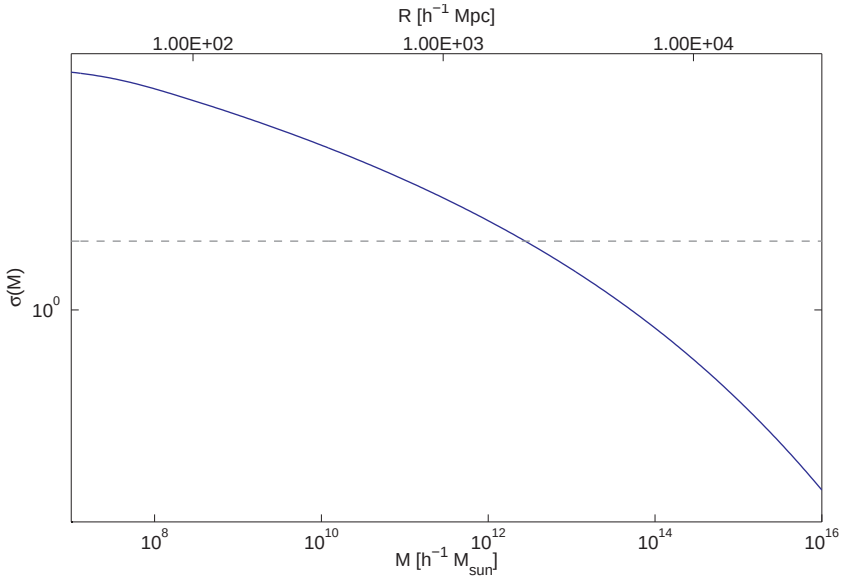

Figure 4.1: The rms density fluctuations in spheres containing mass M at $z = 0$ calculated for the cosmology under consideration in our simulation with `CMBFAST` [Seljak & Zaldarriaga, 1996]. Dashed line shows the collapse threshold $\delta_c = 1.686$ from spherical top hat collapse.

For a correlated sample the probabilities will no longer be independent and the correlation function can now be defined as the excess over random probability of finding two particles separated by r_{12}

$$\delta P(r_{12}) = \bar{n}^2 \left[1 + \xi(r_{12})\right] \delta V_1 \delta V_2. \tag{4.12}$$

Since the probability of having a particle in δV_1 is given by $\bar{n}\delta V_1$, we can write the conditional probability to find a particle in δV_2 given there is one in δV_1

$$\delta P(2|1) = \bar{n} \left[1 + \xi(r_{12})\right] \delta V_2. \tag{4.13}$$

So we see that for correlated samples ($\xi(r_{12}) > 0$) the probability of finding a second particle is enhanced over random, whereas it is suppressed over random for the anticorrelated case ($\xi(r_{12}) < 0$).
Similarly, we can define a quantity which describes how much two different tracers of the cosmological density field are correlated. The **cross-correlation function** between two populations A and B is defined by

$$\delta P(r) = \bar{n}_\mathrm{A} \bar{n}_\mathrm{B} \left[1 + \xi_\mathrm{AB}(r)\right] \delta V_1 \delta V_2, \tag{4.14}$$

which can be calculated from the density fields as

$$\xi_\mathrm{AB}(\boldsymbol{r}) = \langle \delta_\mathrm{A}(\boldsymbol{x}) \delta_\mathrm{B}(\boldsymbol{x} + \boldsymbol{r}) \rangle \,. \tag{4.15}$$

4.4 Bias and Cross-Correlation Coefficient

The **bias** describes the excess clustering of population A with respect to population B and can be defined from cross-correlations and auto-correlations

$$b_\mathrm{AB} = \sqrt{\frac{\xi_{BB}}{\xi_{AA}}}, \qquad\qquad b_\mathrm{AB} = \frac{\xi_{AB}}{\xi_{AA}}. \tag{4.16}$$

This linear relationship between the underlying field and the tracer population will only be applicable in the linear regime and one should note that scale dependence of bias is intensively

discussed in the literature [Smith *et al.* , 2007].
The **cross-correlation coefficient** between populations A and B is defined by[2]

$$r_{\mathrm{AB}} = \frac{\xi_{\mathrm{AB}}}{\sqrt{\xi_{\mathrm{AA}}\xi_{\mathrm{BB}}}} \tag{4.17}$$

and describes the stochasticity between two density fields [Bonoli & Pen, 2008]. It was shown in N-body simulations that this quantity is close to one over a wide range of scales. Similar quantities can be defined for other clustering statistics such as projected correlation functions and power spectrum. The cross-correlation coefficient allways satisfies $-1 \leq r \leq 1$. The profit of r is that if it were really constant $r = 1$ over all scales there was no stochasticity and one could calculate the unobservable dark matter correlation from observable galaxy-matter and galaxy-galaxy correlations by simply inverting Equation (4.17)

$$\xi_{\mathrm{mm}} = \frac{\xi_{\mathrm{gm}}^2}{\xi_{\mathrm{gg}} r^2}. \tag{4.18}$$

It will be a key result of this work to show that r, calculated from projected correlation, is in fact close to one for a realistic galaxy sample that can reproduce the observed galaxy clustering. For a discussion of our findings we refer the reader to §8 on Page 69.

4.5 Gaussian Random Fields

The seeds for structure formation are most probably of quantum mechanical origin. Hence we can treat the density field as a noise-like random field, where the phases of the Fourier modes are independent. From **central limit theorem** we know that the superposition of a large number of independent random fields will tend to a joint normal distribution. Besides δ itself, all quantities that can be expressed by linear sums over the modes will tend to be normally distributed. Since the first moment of δ vanishes, the Gaussian random field is entirely determined by its power spectrum, the variance for a certain Fourier mode.
By **Wick theorem** the reduced correlation functions of order higher than two either vanish or are expressible in terms of two-point functions [Bernardeau *et al.* , 2002]

$$\langle \delta(\boldsymbol{k}_1), \ldots, \delta(k_{2n+1}) \rangle = 0, \tag{4.19}$$

$$\langle \delta(\boldsymbol{k}_1), \ldots, \delta(k_{2n}) \rangle = \sum_{\text{pairs}} \prod_{P\{(i,j)\}} \langle \delta(\boldsymbol{k}_i), \delta(\boldsymbol{k}_j) \rangle . \tag{4.20}$$

The Gaussiannity of the random field is also clear from the commutation relations for the quantum field.

[2] We use the common symbol r to denote the cross correlation coefficient as there should be no confusion with the radius r.

CHAPTER 5

Gravitational Clustering

In the last chapters we saw how small perturbations could form on a smooth background of a Friedmann-Robertson-Walker cosmology. So far we used linearised equations to treat the fluctuations but at some point gravitation will cause the collapse of such overdensities to form non-linear gravitationally bound objects. Eventually the first galaxies will form in these potential wells.
Beginning with a simple model to estimate the properties of the collapsed dark matter haloes we will proceed to derive their abundance using the theory of peaks. Finally we will introduce the halo model, which will be the basis for our further discussion.

5.1 Spherical Collapse Model

To develop a better understanding of the formation of structures in the Universe we will first consider a toy model known as the **spherical top-hat collapse** model that will provide us with some useful numbers of merit, useful for later calculations. Following the arguments in [Liddle & Lyth, 2000, Padmanabhan, 1993], we postulate a spherically symmetric region with uniform overdensity δ_i at initial time t_i in an otherwise uniform critical density matter dominated Universe. We will assume that the additional material is taken from a thin spherically symmetric underdense shell around the overdensity in order to preserve the mean density. According to Birkhoff theorem, the evolution of the Universe outside will be independent of the spherical overdensity and the sphere will behave like a closed Universe with density parameter $\Omega_i = 1+\delta$. We consider the the Friedmann equation for the overdensity

$$\dot{a}^2 = \frac{\Omega_i}{a} + \Omega_i - 1. \tag{5.1}$$

This equation has a parametric solution

$$a = a_0(1-\cos\theta)\frac{\Omega_i}{1-\Omega_i}, \qquad t = t_0(\theta - \sin\theta)\frac{\Omega_i}{(1-\Omega_i)^{3/2}}, \tag{5.2}$$

where we have chosen the integration constant in order to match the time coordinates with the rest of the Universe $t_i = 0$. Here θ runs from 0 to 2π and the maximum expansion occurs at $\theta_{\max} = \pi$. It is convenient to express a and t in terms of their values at maximum expansion or turnaround $a_{\max} = a_0\Omega_i(1-\Omega_i)^{-1}$

$$a = \frac{a_{\max}}{2}(1-\cos\theta), \qquad t = \frac{t_{\max}}{\pi}(\theta - \sin\theta). \tag{5.3}$$

If we now expand both terms for small θ, we obtain the linear theory expression for the development of the overdense region

$$a_{\rm lin}(t) = \frac{1}{4}\left(\frac{6\pi t}{t_{\rm max}}\right)^{2/3}\left[1 - \frac{1}{20}\left(\frac{6\pi t}{t_{\rm max}}\right)^{2/3}\right]. \tag{5.4}$$

The first term on the right hand side describes the expansion of the critical density background Universe. We can use above expression to derive the linear theory prediction for the density contrast

$$\delta_{\rm lin} = \frac{3}{20}\left(\frac{6\pi t}{t_{\rm max}}\right)^{2/3}. \tag{5.5}$$

So we see that turnaround occurs when the linear density contrast is $\delta_{\rm lin}(\pi) \approx 1.06$. At this time the overdensity separates from the uniform expansion of the background Universe and starts to contract even in physical coordinates[1]. The collapse will stop at the final time $t_{\rm fin} = 2\pi$ when the linear theory predicts

$$\delta_{\rm lin}(t_{\rm fin}) = \frac{3}{20}(12\pi)^{3/2} \approx 1.686. \tag{5.6}$$

Consequently we can consider any region for which linear theory predicts an overdensity of 1.686 as being just collapsed. We will use the factor $\delta_{\rm lin}^{\rm fin}$ when we estimate the abundance of dark matter haloes with the Press & Schechter approach in §5.2. In fact the actual overdensity will become infinite at $t_{\rm fin}$. But we are not expecting the collapse to continue until the region collapses to a point. In contrast we expect the dark matter to virialise [2] when its radius shrunk by approximately a factor of two compared to the maximum extension. The common notion for such a virialised dark matter overdensity is **halo**.
The non-linear overdensity of the virialised object can be calculated from the fact that the density of the spherical region will increase by a factor of 8 until virialisation, whereas the background will have expanded by a factor of about 4 by this time. The non-linear density contrast at turnaround is $1 + \delta_{\rm turn} = 5.55$ and hence at virialisation we obtain $1 + \delta_{\rm vir} \approx 178$. This number enables us to estimate the radius-mass relation of dark matter haloes. Linear perturbation theory fails as soon as the overdensity δ approaches unity. But since most of the observable and thus interesting structure in the Universe has overdensities far in excess of unity, we will have to deal with them using a fully non-linear theory. It is important to note that above reasoning, including the numerical values, is true only for an Einstein-de-Sitter Universe.

5.2 Press & Schechter Theory of Peaks

We saw in the last section, that initial overdensities will be amplified by gravitational growth and eventually become bound objects. An important ingredient for theories of structure formation is the abundance of such bound dark matter clumps. To first order the abundance of a halo of mass M will be a function of mass only.
An approximate, but intuitive, approach to this mass function was introduced by [Press & Schechter, 1974]. As ingredients they just used the spherical top hat model and linear growth theory. The assumption underlying this derivation of the mass-function is that the probability distribution of an overdensity of mass M is Gaussian with zero mean and standard deviation $\sigma(M)$, where $\sigma(M)$ is the root mean square overdensity within spheres of radius R. Linear growth leaves the shape of the initially Gaussian fluctuations unaffected and hence we can write for the probability density

$$P(\delta_M)d\delta_m = \frac{1}{\sqrt{2\pi\sigma^2(M)}}\exp\left[-\frac{\delta_M^2}{\sigma^2(M)}\right]. \tag{5.7}$$

[1] Note that the size of the region was decreasing in comoving coordinates from begin on
[2] Virialisation refers to the fact, that there is a equilibrium between kinetic energy and potential energy of the halo. The corresponding dark matter particles form a bound substructure.

As σ is a monotonically decreasing function of mass, inhomogeneities on large scales are smaller in amplitude than those on small scales. Therefore small scale inhomogeneities will be the first to cross the critical density threshold $\delta_c(z)$ that is needed to transform an overdensity into a virialised object, an effect which is termed the **bottom up** picture of structure formation. Hence the probability to have overdensities of mass M exceeding a density thereshold δ_c is given by

$$f(M,\sigma) = \mathrm{erf}\left(\frac{\delta_c}{\sqrt{2}\sigma}\right), \qquad \mathrm{erf}(x) = \frac{1}{\sqrt{\pi}}\int_x^\infty \exp\left[-x^2\right]dx. \tag{5.8}$$

Guided by linear theory and the spherical collapse model Press & Schechter assumed $\delta_c \approx 1.686$ for the Einstein-de Sitter case. The above probability is equivalent to the fraction of points that exceeds the threshold. Actually we are interested in the number of collapsed objects of a certain mass, thus we have to calculate the number of objects, which are collapsing at a certain time by subtracting $P(M+dM) - P(M)$ and multiplying by the maximum possible number density of objects $\bar{\rho}/M$

$$n(M)dM = \frac{\bar{\rho}}{M}\left[P(M+dM) - P(M)\right]dM = \frac{\bar{\rho}}{M}\left|\frac{df(\delta,\sigma)}{d\sigma}\right|\frac{d\sigma}{dM}dM. \tag{5.9}$$

After some algebra we obtain

$$n(M)dM = \frac{\bar{\rho}}{M}\sqrt{\frac{2}{\pi}}\exp\left[-\frac{\delta_c^2}{\sigma^2(M)}\right]\frac{\delta_c}{\sigma^2(M)}\frac{d\sigma}{dM}dM. \tag{5.10}$$

This equation is often written in terms of the **peak height**

$$\nu := \left[\frac{\delta_c}{\sigma(M)}\right]^2, \tag{5.11}$$

which yields the well known form of the massfunction

$$\frac{M}{\bar{\rho}}n(M)dM = f(\nu)d\nu = \frac{1}{\nu}\sqrt{\frac{\nu}{2\pi}}\exp\left[-\frac{\nu}{2}\right]. \tag{5.12}$$

A problem which arises in the above heuristic reasoning is that we did not account for the possibility that a structure collapsing at z can be part of a larger structure collapsing at the same time, a subtlety termed the **cloud in cloud problem**. Furthermore only half of the points are associated with an overdensity and collapse. This problem can be eluded by multiplying the number density with a factor of two. The Press & Schechter mass-function underestimates the abundance of massive halos in N-body simulations and has been improved by [Sheth & Tormen, 1999] to give a better fit to the simulations

$$\nu f(\nu) = A(p)\left[1 + \frac{1}{(q\nu)^p}\right]\left(\frac{q\nu}{2\pi}\right)^{1/2}\exp\left[-\frac{q\nu}{2}\right]. \tag{5.13}$$

The parameters used by Sheth & Tormen are $q = 0.707$ and $p = 0.3$ and the choice $q = 1$, $p = 0$ recovers the Press & Schechter formula. The prefactor A of the Sheth & Tormen mass function is determined by the constraint

$$\int n(M)MdM = \int f(\nu)d\nu = \bar{\rho}. \tag{5.14}$$

Figure 5.1 shows both theoretical massfunctions and the actually measured massfunction for simulation outputs at redshift $z = 0$ and $z = 0.23$. We clearly see the failure of the Press & Schechter for the high mass haloes probed in our simulation. For the mass function at $z = 0.23$ we scaled $\sigma(M)$ using the linear growth factor

$$\sigma(M,z) = \frac{D_1(z)}{D_1(0)}\sigma(M,0). \tag{5.15}$$

Often one defines a characteristic mass scale M_* which is collapsing at present time and hence has $\nu(M_*,z) = 1$.

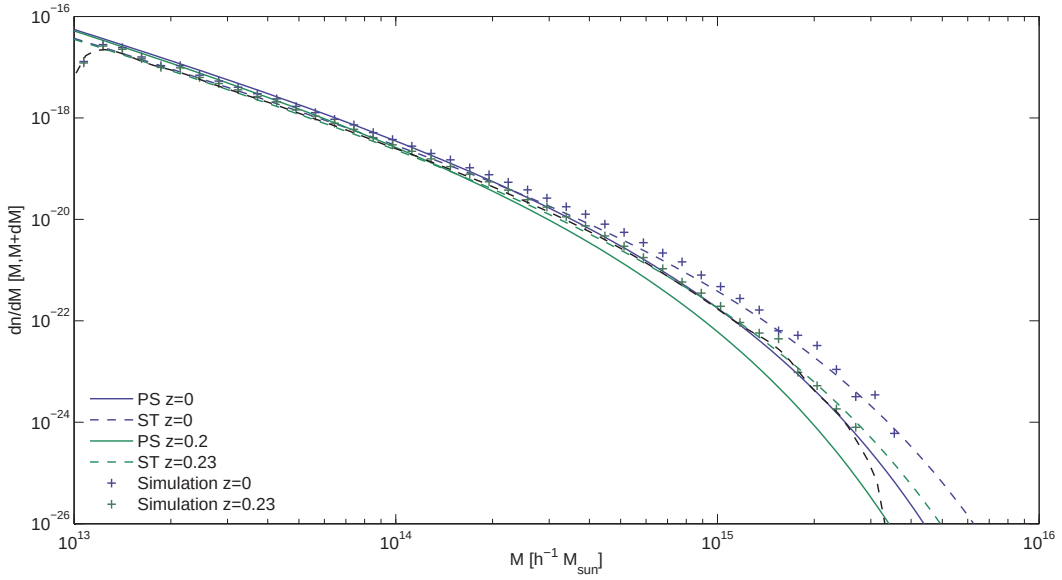

Figure 5.1: Mass-function as measured for the simulation outputs at redshift $z = 0$ (blue) and $z = 0.23$ (green). For comparison we show the [Press & Schechter, 1974] (solid) and [Sheth & Tormen, 1999] (dashed) mass-functions. Press & Schechter underestimates the abundance of massive haloes, whereas Sheth & Tormen gives a reasonable fit to the measurement.

5.3 Mass Dependent Halo Bias

Following an approach presented in [Cooray & Sheth, 2002] we can consider the space divided up in cells of comoving volume V containing different amounts of mass M which leads to different densities δ_0. Each of this cells will contain a specific number of halos of mass m denoted by $N(m|M,V)$. We can now calculate the overdensity of such halos with respect to the mean number of collapsed objects of a certain mass given by the Press & Schechter or Sheth & Tormen approach

$$\delta_{\mathrm{h}}(m) = \frac{N(m|M,V)}{n(m)V} - 1. \tag{5.16}$$

$N(m|M,V)$ can be considered as a modified version of the known mass function, accounting for the overdensity δ_0 of the cell under consideration.

$$\tilde{\nu} = \frac{[\delta_{\mathrm{c}}(z_1) - \delta_0(z_1)]^2}{\sigma^2(m) - \sigma^2(M)} \tag{5.17}$$

Carrying out the manipulations up to lowest order in the large cell limit we get an equation that tells us that the overdensity of halos is proportional to the overdensity in mass.

$$\delta_{\mathrm{h}}(m) = \left(1 + \frac{\nu - 1}{\delta_{\mathrm{c}}(z_1)} + \frac{2p}{\delta_{\mathrm{c}}(z_1)} \frac{1}{1 + (q\nu)^p}\right) \delta_0 = b(m)\delta_0 \tag{5.18}$$

The overdensity of halos in large cells is linearly dependent on the overdensity of the mass in this cell. Massive halos with $M > M_*$ are said to be biased relative to the dark matter and have $b(m, z_1) > 1$. The bias is dependent on the halo mass m and the redshift of virialisation z_1. This proportionality directly affects the halo-halo autocorrelation as well as the halo-halo power spectrum.

$$\xi^{\mathrm{hh}}(r|M_1, M_2) = b(M_1)b(M_2)\xi^{\mathrm{lin}}(r) \tag{5.19}$$

Bias also refers to the fact, that the galaxy-clustering will be enhanced with respect to the mass by a scale independent factor b. As we will see this galaxy bias naturally arises from the halo model description of the galaxy clustering. The scale independence was subject to numerical and analytical investigations which came to the conclusion, that bias in fact is changing with radial distance.

5.4 Halo Density Profiles

Halos can be considered as peaks in the initial density field. Massive halos therefore correspond to higher peaks in the initial fluctuation field. From spherical top hat collapse we know that virialised objects have a mean mass excess of about $\delta \approx 180$ (for an Einstein-de Sitter toy model) compared to the uniform background density. The sphere within which the mean density is $\delta_{\rm vir}$ times the background density is bounded by the virial radius $r_{\rm vir}$, and contains the total mass of the halo $M_{\rm vir}$. The spherically averaged radial distribution of mass within a halo is called the **halo density profile**. This profile is considered to depend in first order only on the mass of the halo, and can be understood as an average over all halos of a given mass. A profile introduced by Navarro, Frenk & White (NFW) [Navarro *et al.* , 1996] has been extensively studied and provides good fits to N-body simulations.

$$\rho(r|m) = \frac{\rho_{\rm s}}{\left(\frac{r}{r_{\rm s}}\right)^{\alpha}\left(1+\frac{r}{r_{\rm s}}\right)^{\beta}} = \frac{\rho_{\rm s}}{\left(y\right)^{\alpha}\left(1+y\right)^{\beta}}. \tag{5.20}$$

In the last equality we introduced the parametrisation $y := r/r_{\rm s}$. This profile has the logarithmic slope

$$\frac{d\ln\rho}{d\ln r} = -\alpha - \beta\frac{y}{1+y}, \tag{5.21}$$

That is, it decreases as $r^{-\alpha}$ for small scales and as $r^{-\alpha-\beta}$ for larger scales. Parameters $\alpha = 1, \beta = 2$ were proposed by NFW but there is no consensus about the inner slope, leading to different values for α in the literature [Cooray & Sheth, 2002]. The free parameters of the model are the **scale radius** $r_{\rm s}$ and the density at this radius $\rho_{\rm s}$. The latter follows from the condition

$$M = \int_0^{r_{\rm vir}} \rho(r|M) 4\pi r^2 dr, \tag{5.22}$$

which for the NFW profile leads to

$$\rho_{\rm s} = \frac{M}{4\pi r_{\rm s}^3\left(\ln(1+c) - \frac{c}{1+c}\right)}. \tag{5.23}$$

Here we introduced the **concentration parameter**

$$c = \frac{r_{\rm vir}}{r_{\rm s}}. \tag{5.24}$$

In the easyest case the concentration parameter will be a function of halo mass only, and can be modeled by a power law

$$c(M) = c_0\left(\frac{M}{M_*}\right)^{\gamma}. \tag{5.25}$$

Here M_* is the non-linear mass scale and we find for the cosmology used in our simulations, that $M_*(z=0) = 2.73\times10^{12}\ h^{-1}M_\odot$ and $M_*(z=0.23) = 1.47\times10^{12}\ h^{-1}M_\odot$. According to [Cooray & Sheth, 2002] the halo concentration follows a log-normal distribution around the mean

$$\bar{c}(M,z) = \frac{9}{1+z}\left[\frac{M}{M_*}\right]^{-0.13}. \tag{5.26}$$

The negative exponent in above formula expresses the fact that more massive haloes are more centrally concentrated.

5.5 Halo Model & Halo Occupation Distribution

The **halo model** assumes that all the mass in the Universe is partitioned up into distinct units, which are small compared to the distance between this units. These finite clumps of matter are often called **halos**. In Figure 5.2 we show the projection of the dark matter density

field calculated with a N-body code together with the positions of a synthetic galaxy sample. From a phenomenological point of view, one sees in N-body simulations that the matter clumps are connected by tubelike matter **filaments** and that there are also large **voids**, which are almost devoid of matter. A comprehensive review of the halo model was compiled by [Cooray & Sheth, 2002].

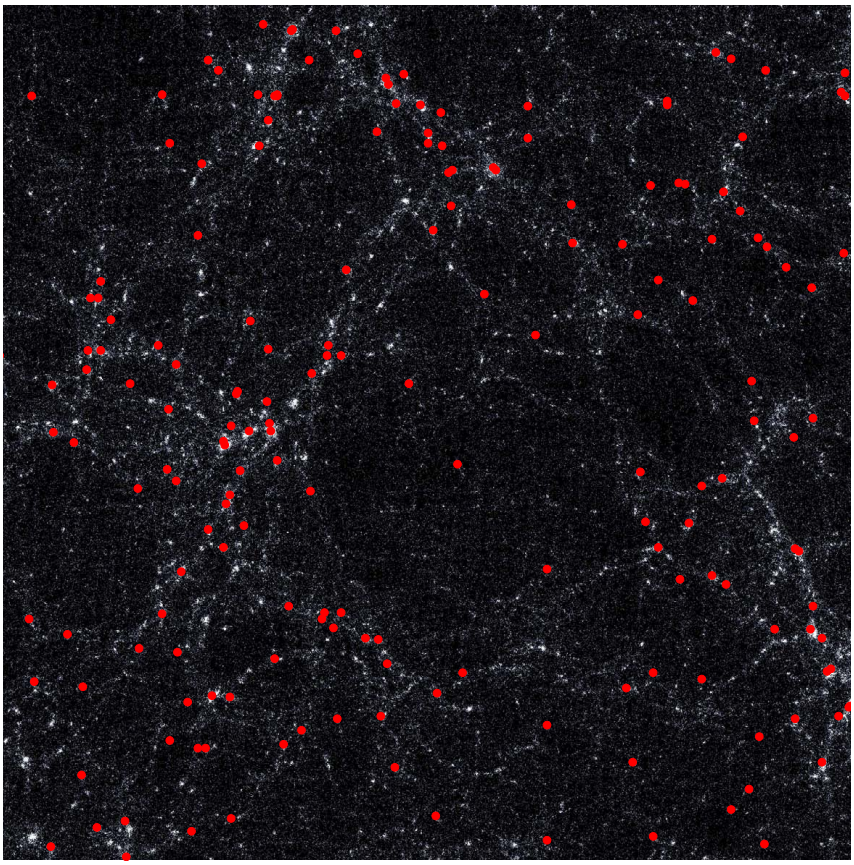

Figure 5.2: Dark matter density field in a box of width $\Delta x = \Delta y = 200\ h^{-1}$Mpc and thickness $\Delta z = 100\ h^{-1}$Mpc. We overplot the positions of bright LRGs from our best fit model at redshift $z = 0.23$.

This clumpiness of the dark matter leads one to model the clustering by an appropriate superposition of small and large scale contributions. On small scales the statistics are mainly influenced by the inner structure of the halo, whereas on large scales the spatial distribution of the halos becomes important.
If we want to use the halo model to calculate clustering statistics we have to put together the following ingredients:

- a mass function, which describes the abundance of haloes of a given mass
- a halo biasing scheme, which describes how strongly the haloes are clustered with respect to the matter
- a profile which describes how the dark matter and the galaxies are distributed within their host halo
- the occupation statistics, which describe how many central and satellite galaxies reside on average within a halo of given mass and the statistic which describes the distribution of the actual number around the mean

The **halo occupation distribution** quantifies the conditional probability $P(N|M)$ that a dark matter halo of mass M contains N galaxies of a certain type. In principle physics of galaxy formation should determine the relation between galaxy and dark matter distribution, but it is reasonable to assume that galaxies are, at least to some degree, biased tracers of the underlying dark matter density field and its haloes.

While the exact spatial distribution of galaxies within their host halo will depend on baryonic processes, such as gas dynamics, radiative cooling and star formation, the large scale distribution of the haloes themselves is entirely determined by the gravitational clustering. So the HOD provides a framework in which the background cosmological evolution can be supplemented by a phenomenological description of galaxy formation. Having determined the free parameters of the HOD we can in principle extract all the needed information from the model: the small and large scale clustering, the bias, properties of host haloes and redshift space effects. Due to its conceptual simpleness it provides intuitive physical interpretations for simulations and observations.
The basic principles of a HOD were first introduced by [Neyman & Scott, 1952], who disentangled galaxy clustering into clustering of clusters and the distribution of galaxies within clusters. This theoretical approach caused new excitement in the community when analytical tools for the prediction of the clustering properties of haloes [Sheth & Tormen, 1999] and for the mass distribution within the haloes [Navarro *et al.* , 1996] became available. It was recognised that the occupation statistics could be used to extend the calculations for dark matter clustering to biased tracers, such as haloes and galaxies [Seljak, 2000a, Peacock & Smith, 2000, Berlind & Weinberg, 2002].
The occupation number for galaxies of a certain brightness will be mainly influenced by the host halo mass and provides a means to constrain theories of galaxy formation. Bright galaxies will not be able to form in light haloes, since there is not enough cold gas and thus it is intuitive to translate thresholds in luminosity into thresholds in mass, including some mechanism to account for the scatter introduced by e.g. merging processes.
The halo occupation distribution was used successful in the literature for a wide variety of studies. It was used to interpret the LRG clustering in the SDSS by [Reid & Spergel, 2008, Reid *et al.* , 2008], redshift space distortions were studied by [Tinker, 2007] and the supernovae–galaxy correlation was modeled by [Padmanabhan *et al.* , 2008].
We will not explore the analytical modelling of the dark matter or galaxy clustering with the halo model, but it is helpful to develop an understanding, which quantities contribute to the clustering statistics.
Figure 5.3 gives a schematic overview of the halo model. In the top left panel we show two nearby dark matter haloes together with the galaxies hosted by the haloes. The haloes are distinct dark matter clumps defined by their virial radii and are non-overlapping by definition. A basic building block of the correlation functions in the halo model is the clustering of the haloes themselves. This clustering can be approximated by a phenomenological bias and the linear matter correlation

$$\xi^{\mathrm{hh}}(r|M_1, M_2) \approx b(M_1)b(M_2)\xi^{\mathrm{lin}}(r). \tag{5.27}$$

The **matter-matter autocorrelation** shown in the top right panel of Figure 5.3 is a sum of the correlation between the dark matter particles within one halo and the correlation of the dark matter particles within two distinct haloes. The one-halo term is essentially a convolution of the dark matter profile with itself, whereas the two halo term is a superposition of the halo profile of the two haloes and the clustering of the haloes themselves.
To model galaxy–dark matter cross-clustering correctly we have to distinguish the contributions of central and satellite galaxies, where the latter has to be described by the satellite profile. The centrals are allways assumed to sit at the haloes centre of mass. In the bottom left panel of Figure 5.3 we show schematically the following terms that can contribute to to the **galaxy-matter cross-correlation**.

one halo	two halo
central	central
satellite	satellite

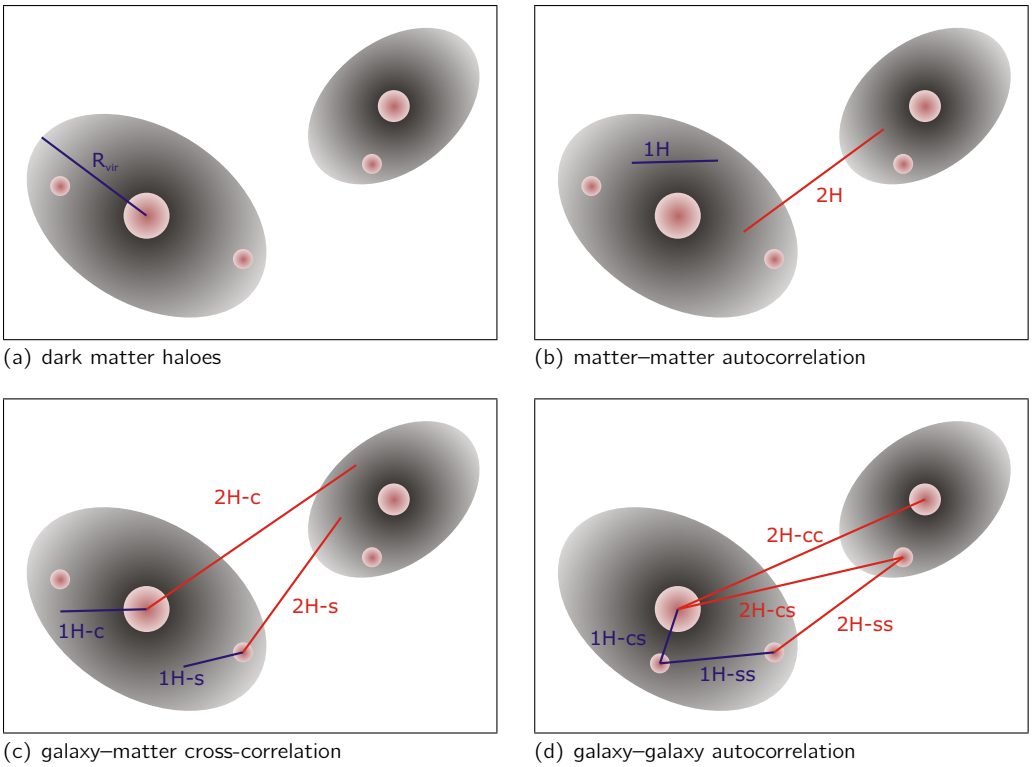

(a) dark matter haloes

(b) matter–matter autocorrelation

(c) galaxy–matter cross-correlation

(d) galaxy–galaxy autocorrelation

Figure 5.3: Visualisation of the terms contributing to the correlation functions in the halo model. Ellipses are dark matter haloes whereas the red circles are galaxies residing in this haloes. We denote one and two halo terms by 1H and 2H and central and satellite contributions by c and s, respectively.

Finally, the bottom right panel of Figure 5.3 visualises the terms contributing to the **galaxy-galaxy autocorrelation**:

one halo	two halo
central-satellite	central-central
satellite-satellite	central-satellite
–	satellite-satellite

CHAPTER 6

Gravitational Lensing

We will now review the theoretical foundations of light deflection by gravitational fields. In the context of general relativity light propagates on the null geodesics of the spacetime metric. The general setup of gravitational lensing is shown in Figure 6.1. Light, or more generally radiation, from a source is deflected by the gravitational potential of the energy density distribution along the line of sight, and is finally observed as an image by the observer. If the there is only one dominant deflector along the line of sight, which has a radial extension much smaller than the angular diameter distances to the lens and to the source, we can approximate the deflected light ray by two straight rays which kink in the lens plane. This bending of light toward the observer depends on the distances between source, lens and observer and on the total mass of the lens. Strong gravitational lensing leads to multiple images of a source and can even produce arcs and rings.
We will first give an overview over general lensing theory and then focus on weak-lensing, especially galaxy-galaxy lensing. For a more detailed treatment we refer the reader to textbooks on general relativity and the excellent review by [Bartelmann & Schneider, 2001].

6.1 Basic Principles of Gravitational Lensing

We will consider general relativity in its weak field limit, i. e. we decompose the metric into a flat background metric plus a small perturbation $g_{\mu\nu} = \eta_{\mu\nu} + h_{\mu\nu}$

$$ds^2 = -(1+2\Phi)dt^2 + (1-2\Phi)\left(dx^2 + dy^2 + dz^2\right). \tag{6.1}$$

Consequently the light geodesic can be decomposed in a straight zero order null curve and a perturbation on it $x^\mu(\lambda) = x^{(0)\mu} + x^{(1)\mu}$. This means that the smooth bending of the light ray can be approximated by a kink in the lens plane with a deflection angle given by (see e. g. [Carroll, 2004])

$$\hat{\alpha} = 2\int \nabla_\perp \Phi ds. \tag{6.2}$$

The easyest case to consider is a light ray passing a gravitational point source with impact parameter b, for which general relativity predicts a **deflection angle** of[1]

$$\hat{\alpha} = \frac{4GM}{c^2 b}. \tag{6.3}$$

Alltogether, we will adopt the following assumptions widely used in lensing theory: First the

[1] Remarkably thats twice the value which can be obtained from Newtonian gravity by treating light as a particle.

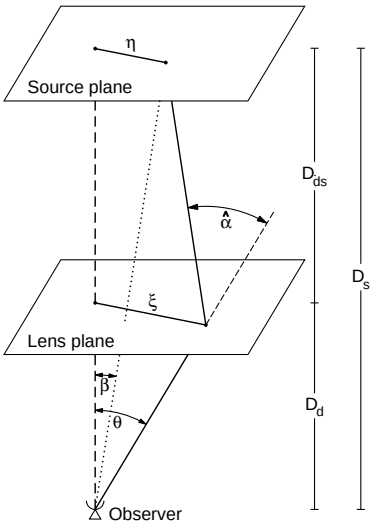

Figure 6.1: Setup for the lensing from [Bartelmann & Schneider, 2001]. A photon emitted in the source plane travels on a null geodesic until it is deflected by the energy distribution in the lens plane. Finally the photon that in the absence of lensing would be observed under an angle $\boldsymbol{\beta}$ is observed under the angle $\boldsymbol{\theta}$.

gravitational field is assumed to be weak, i. e. the motion of rigid bodies can be described by Newtonian gravity. Second the extent of the lens mass is negligible compared to the lens-source and observer-lens distance, which implies that we only have to consider the two dimensional projection of the mass to the lens plane. Third, and most important for the weak field approach to be valid is that the involved radii are large compared to the **Schwarzschild radius** $r = 2GM/c^2$. According to the second point made above, in the following we will be concerned with two dimensional vectors, representing either distances or angles. The conversion of lengths perpendicular to the line of sight into distances can be easily performed using the angular diameter distance.
In the weak field limit, applicable to almost all astrophysical relevant situations, the total deflection can be calculated by a superposition of deflections caused by point masses

$$\hat{\boldsymbol{\alpha}}(\boldsymbol{\xi}) = \frac{4G}{c^2} \int d^2\xi' \int d\chi \rho(\boldsymbol{\xi}, \chi) \frac{\boldsymbol{\xi} - \boldsymbol{\xi}'}{|\boldsymbol{\xi} - \boldsymbol{\xi}'|^2}, \tag{6.4}$$

where χ is the distance along the line of sight and ρ is the density.
This definition can be further simplified by the definition of the **projected surface mass density**

$$\Sigma(\boldsymbol{\xi}) = \int d\chi \rho(\boldsymbol{\xi}, \chi). \tag{6.5}$$

With the knowledge of the deflection angle we can now write down the **lens equation** for the angles defined in Figure 6.1

$$\boldsymbol{\beta}(\boldsymbol{\theta}) = \boldsymbol{\theta} - \frac{D_{\mathrm{ds}}}{D_{\mathrm{s}}} \hat{\boldsymbol{\alpha}}(\boldsymbol{\theta}) = \boldsymbol{\theta} - \boldsymbol{\alpha}(\boldsymbol{\theta}). \tag{6.6}$$

Note that we redefined $\boldsymbol{\alpha}$ and that above equation is only true, if the distance to lens and source galaxies is the same for all galaxies in the sample. We will come back to this issue below. Above equation is an implicit equation for $\boldsymbol{\theta}$, i. e. for given galaxy position $\boldsymbol{\beta}$ there can be more than one solution, an effect which can lead to multiple images in the strong lensing regime.
We can now define the **critical surface mass density** and the **convergence**

$$\Sigma_{\mathrm{crit}} := \frac{c^2 D_{\mathrm{s}}}{4\pi G D_{\mathrm{ds}} D_{\mathrm{d}} (1 + z_{\mathrm{d}})}, \qquad \kappa := \frac{\Sigma}{\Sigma_{\mathrm{crit}}}, \tag{6.7}$$

where D_s, D_d, D_{ds} are the angular diameter distances to the source, to the lens and between lens and source, respectively. From (6.4) one easily sees that $\boldsymbol{\alpha}$ can be written as the gradient of the **lensing potential**

$$\psi(\boldsymbol{\theta}) = \frac{1}{\pi} \int d^2\theta' \kappa(\boldsymbol{\theta}') \ln |\boldsymbol{\theta} - \boldsymbol{\theta}'|, \tag{6.8}$$

as $\boldsymbol{\alpha} = \boldsymbol{\nabla}\psi$. The lensing potential is the two dimensional analogue of the gravitational potential and satisfies a Poisson equation[2]

$$2\kappa = \boldsymbol{\nabla}^2\psi = \partial_1^2\psi + \partial_2^2\psi. \tag{6.9}$$

We will now consider the case that the angular scale of the source is much smaller than the scale over which the mass distribution in the lens plane changes significantly. In this limit we can expand the deflection around the solution for the centre of the source, and the distortion of images is described by the Jacobian matrix

$$\boldsymbol{\beta} = \boldsymbol{\beta}_0 + \mathcal{A}(\boldsymbol{\theta}_0)(\boldsymbol{\theta} - \boldsymbol{\theta}_0), \tag{6.10}$$

where

$$\mathcal{A}(\boldsymbol{\theta}) = \frac{\partial\boldsymbol{\beta}}{\partial\boldsymbol{\theta}} = \left(\delta_{ij} - \frac{\partial^2\psi(\boldsymbol{\theta})}{\partial\theta_i\partial\theta_j}\right) = \begin{bmatrix} 1-\kappa & 0 \\ 0 & 1-\kappa \end{bmatrix} + \begin{bmatrix} -\gamma_1 & -\gamma_2 \\ -\gamma_2 & \gamma_1 \end{bmatrix}. \tag{6.11}$$

In above equation we introduced the components of the complex **shear** $\gamma = \gamma_+ + i\gamma_\times$

$$\gamma_+ = \frac{1}{2}\left(\partial_1^2\psi - \partial_2^2\psi\right), \qquad \gamma_\times = \partial_1\partial_2\psi. \tag{6.12}$$

It is important to note that the shear transforms under a rotation of the coordinate frame by an angle φ, as $\gamma' = \gamma \exp[i2\varphi]$, i. e. it is a polar rather than a vector.
The magnification describes the ratio of the flux observed for the image to the flux one would observe for the unlensed image and is given by the determinant of the Jacobian

$$\mu = \frac{1}{(1-\kappa)^2 - |\gamma|^2}. \tag{6.13}$$

For axisymmetric mass distributions one can derive [Schneider, 2006]

$$|\gamma| = \bar{\kappa}(\theta) - \kappa(\theta), \tag{6.14}$$

where $\bar{\kappa}(\theta)$ is the mean convergence within a circular annulus of radius θ. We will not show the derivation here but rather consider the more general case of non-axisymmetric lenses in the context of galaxy-galaxy lensing in §6.4 below.

6.2 Weak Lensing

The matter distribution of elliptical galaxies can be probed at small scales using velocity dispersion measurements and a bit further out using kinematic tracers such as satellite galaxies. Other measurements, such as X-ray emission or strong lensing, have been performed on individual clusters, but so far this analysis has not converged to a single picture, owing to the lack of statistical power. Weak lensing in contrast can be used to investigate the dark matter distribution around a large number of central galaxies and to probe it out to several 10 h^{-1}Mpc. In most cases the lens is not strong enough to form multiple images or arcs. If the light coming from a distant galaxy population passes through the gravitational field of a foreground mass ensemble the shape of the galaxy images is stretched by the tidal component of the gravitational field and the apparent brightness is changed by the magnification associated with gravitational lensing. As most galaxies have an intrinsic ellipticity, we are not able to directly infer the tidal

[2] If not otherwise stated all derivatives are with respect to components of vector $\boldsymbol{\theta}$, i.e. $\partial_1 = \partial/\partial\theta_1$.

gravitational field from the shape of the images. Under the assumption of randomly oriented intrinsic ellipticity with net ellipticity small compared to Poisson noise, we can infer the strength of the gravitational field using a set of images.
The above equations can be conveniently rewritten in terms of the **reduced shear**

$$g(\boldsymbol{\theta}) = \frac{\gamma(\boldsymbol{\theta})}{1-\kappa(\boldsymbol{\theta})}. \tag{6.15}$$

So that the Jacobian matrix for the lensing becomes

$$\mathcal{A} = (1-\kappa)\begin{bmatrix} 1-g_1 & -g_2 \\ -g_2 & 1+g_1 \end{bmatrix}, \tag{6.16}$$

and the eigenvalues reduce to $\lambda_\pm = 1 \pm |g|$.
For elliptical images with axis ratio a/b and position angle of the major axis φ we can define the complex **ellipticity** by[3]

$$e_\mathrm{i} = e_+ + ie_\times = \frac{1-(a/b)^2}{1+(a/b)^2}\exp[2i\varphi]. \tag{6.17}$$

The **weak lensing** regime regime is defined by $|\gamma| \ll 1$, $\kappa \ll 1$ and hence we have $g \approx \gamma$.
The ellipticity of a single source galaxy contains little information, since the intrinsic ellipticity is unknown. We will consider an ensemble of galaxy images close to the reference point $\boldsymbol{\theta}_0$ such that the local expansion of the lens equation (6.10) is valid. We will further assume that the expectation of the source ellipticities vanishes

$$\langle e_\mathrm{s}\rangle = 0. \tag{6.18}$$

Assuming that all sources are at the same redshift, the ellipticity of a circular source is given by the ratio of the eigenvalues of $\mathcal{A}$. This remains true for the net ellipticity of an ensemble of images if the net ellipticity of the sources vanishes. The ratio of the eigenvalues can be rewritten using the reduced shear and further simplified using the weak lensing approximation

$$|e| = \frac{\lambda_-}{\lambda_+} = \frac{1-|g|}{1+|g|} \approx 1 - 2\,|\gamma|\,. \tag{6.19}$$

Above equation is just another way of stating

$$e_\mathrm{i} = e_\mathrm{s} - 2g. \tag{6.20}$$

Using $\langle e_\mathrm{s}\rangle = 0$ and (6.17) we obtain:

$$\gamma \approx \frac{\langle e_\mathrm{i}\rangle}{2} \approx \frac{1-(a/b)^2}{1+(a/b)^2}\frac{\exp[2i\varphi]}{2} \tag{6.21}$$

We will see below that this expression has to be adapted for real measurements.

6.3 Galaxy-Galaxy Lensing

Galaxy-galaxy lensing measures the tangential elongation of background galaxies by the dark mass around the lens galaxy. These shape distortions are generally very weak and hence large numbers of lenses have to be stacked to obtain sufficient signal-to-noise.

The quantity most directly related to galaxy-galaxy lensing is the tangential shear γ_t. It describes the distortion of the image shape perpendicular to the line connecting the image and the lens galaxy and is given by the 2-d shear rotated to the frame defined by the image and the lens (see Figure 6.2)

$$\gamma_\mathrm{t}(\boldsymbol{\theta}) = -\gamma_+(\boldsymbol{\theta})\cos(2\beta) + \gamma_\times(\boldsymbol{\theta})\sin(2\beta), \tag{6.22}$$

[3] More generally this quantity is defined by the tensor of second brightness moments.

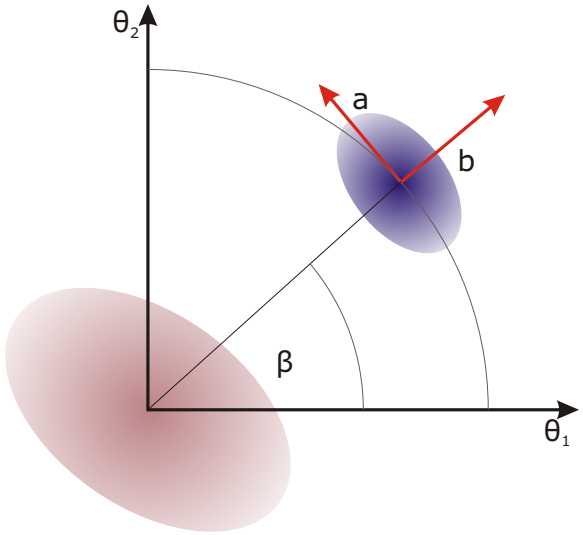

Figure 6.2: The dark halo at the origin of the Cartesian frame (θ_1, θ_2) leads to a tangential stretching of the images of background galaxies. The shear can be determined from the ratio of the major-axis a, b of background galaxies, measured in a frame defined by the axis connecting the halo and the galaxy.

where β is the angle between the x-axis and the line defined by the lens and the image. As we will show in §6.4, the circular averaged tangential shear is related to the **excess surface mass density** [Miralda-Escude, 1996]

$$\Delta\Sigma(R) = \bar{\Sigma}(R) - \Sigma(R) = \langle\gamma_t(R,\varphi)\rangle_\varphi \, \Sigma_{\rm crit}, \tag{6.23}$$

where $\Sigma(R)$ is the projected surface mass density and $\bar{\Sigma}(R)$ is its average over a circular aperture

$$\bar{\Sigma}(R) = \frac{2}{R^2}\int_0^R \Sigma(R')R'dR'. \tag{6.24}$$

For the interpretation one assumes that the lensing is associated with the overdensity around this galaxy and hence with the galaxy-matter cross-correlation

$$\Sigma(R) = \int_{-\chi_{\rm max}}^{\chi_{\rm max}} \bar{\rho}\left[1 + \xi_{\rm gm}(\sqrt{R^2+\chi^2})\right] d\chi. \tag{6.25}$$

Note that the constant $\bar{\rho}\chi_{\rm max}$ cancels out when calculating $\Delta\Sigma$, so that we can omit it in the following. This relation reveals the potential of galaxy-galaxy lensing – from the measurement of the tangential shear one can recover the dark-matter density field.

To calculate $\gamma_{\rm t}$ one measures the ellipticity of the images around a lens galaxy in a fixed Cartesian frame, calculates $\gamma = \gamma_+ + \gamma_\times$ in this frame and then transforms it to the tangential frame.

If we use a sample of source galaxies, with a radial distribution $W(\chi_{\rm s})$ instead of an exact distance the critical surface mass density is no longer a constant and has to be included in the integral in (6.7)

$$\kappa(\boldsymbol{\theta}) = 4\pi G\int_{-\infty}^{\infty} g(\chi)\rho(\boldsymbol{\theta},\chi)d\chi, \tag{6.26}$$

where

$$g(\chi) = D_{\rm A}(\chi)\int_\chi^{+\infty}\frac{D_{\rm A}(\chi_{\rm s}-\chi)}{D_{\rm A}(\chi_{\rm s})}W(\chi_{\rm s})d\chi_{\rm s}, \tag{6.27}$$

is an effective critical surface mass density for the source distribution.

Measuring γ with sufficient signal-to-noise requires large numbers of background galaxies,

since the shape distortions due to a typical dark matter halo associated with the lens galaxy are very weak. As an additional problem it was shown that the background galaxies have non-zero intrinsic ellipticities [Hirata *et al.* , 2007]. The signal is therefore calculated by stacking thousands of lens galaxies resulting in a shear signal, which is an average over the properties of galaxies in a certain luminosity bin, or equivalently haloes within a certain mass bin [Miralda-Escude, 1991, Cacciato *et al.* , 2008].
The fact that lensing can only be detected, when the signal of many lenses is stacked hampers the interpretation in terms of the connection between galaxies and dark matter haloes. The galaxies reside in haloes of different mass and hence the lensing signal is a nontrivial average of the lensing produced by haloes of very different masses. Furthermore one has to distinguish between central and satellite galaxies as they cause different lensing signals. This requires knowledge about the satellite/central fraction and the spatial distribution of satellites within their dark matter haloes. Both effects have been studied using numerical N-body simulations [Mandelbaum *et al.* , 2005, Hayashi & White, 2007].

6.4 Derivation of the Mass-Shear Relation

For the analysis of galaxy-galaxy lensing we have to relate the tangential shear to the excess surface mass density. To do so we consider the two dimensional version of Gauss theorem on a ball with radius $R = \theta D_\mathrm{d}$ around the origin of a (θ_1, θ_2) coordinate system

$$\int_{B_R} d^2R' \boldsymbol{\nabla}^2_{R'} \psi(R', \varphi') = \oint_{\mathcal{C}(B_R)} dS \boldsymbol{n} \cdot \boldsymbol{\nabla} \psi(R', \varphi'), \tag{6.28}$$

$$\int_{B_\theta} d^2\theta' \boldsymbol{\nabla}^2_{\theta'} \psi(\theta', \varphi') = \oint_{\mathcal{C}(B_\theta)} dS \boldsymbol{n} \cdot \boldsymbol{\nabla} \psi(\theta', \varphi'), \tag{6.29}$$

where ψ is an arbitrary scalar function and $\boldsymbol{n}$ is the outwards pointing normal to the circle. Recalling the definitions of the convergence and shear

$$2\kappa = \left(\partial^2_{\theta_1} + \partial^2_{\theta_2}\right) \psi, \qquad 2\gamma_1 = \left(\partial^2_{\theta_1} - \partial^2_{\theta_2}\right) \psi, \tag{6.30}$$

we can define a quantity $m(\theta)$ considering ψ in equation (6.29) as the deflection potential

$$m(\theta) := \int_{B_\theta} d^2\theta' \boldsymbol{\nabla}^2_{\theta'} \psi(\boldsymbol{\theta}') = 2 \int_{B_\theta} d^2\theta' \kappa(\boldsymbol{\theta}') \tag{6.31}$$

$$= \theta \int_0^{2\pi} d\varphi' \partial_\theta \psi(\boldsymbol{\theta}'), \tag{6.32}$$

where we rewrote the directional derivative $\boldsymbol{n} \cdot \boldsymbol{\nabla} \psi = \partial_\theta \psi$. Differentiation of m with respect to θ yields

$$\frac{dm}{d\theta} = \frac{m}{\theta} + \theta \int_0^{2\pi} d\varphi' \partial^2_\theta \psi(\boldsymbol{\theta}'). \tag{6.33}$$

We now consider a point on the θ_1-axis, such that

$$\partial^2_\theta \psi = \partial^2_{\theta_1} \psi = \kappa + \gamma_1 = \kappa - \gamma_\mathrm{t}. \tag{6.34}$$

Above equality is independent of the choice of the polar angle φ and hence valid for all points on the circle. The integral over φ yields an angular average over the circle of radius θ, such that

$$\frac{dm}{d\theta} = \frac{m}{\theta} + 2\pi\theta \Big(\langle \kappa(\theta, \varphi) \rangle_\varphi - \langle \gamma_\mathrm{t}(\theta, \varphi) \rangle_\varphi \Big). \tag{6.35}$$

These angular averages can also be obtained by rewriting the lhs of Gauss theorem

$$m(\theta) = 4\pi \int_0^\theta d\theta' \theta' \langle \kappa(\theta', \varphi) \rangle_\varphi \;\Rightarrow\; \frac{dm}{d\theta} = 4\pi\theta \langle \kappa(\theta, \varphi) \rangle_\varphi . \tag{6.36}$$

To conclude we divide (6.35) and (6.36) by $2\pi\theta$ and equate

$$\frac{1}{2\pi\theta}\frac{dm}{d\theta} = 2\langle\kappa(\theta,\varphi)\rangle_\varphi = \frac{1}{\pi\theta^2}\int_{B_\theta} d^2\theta'\kappa(\theta') + \langle\kappa(\theta,\varphi)\rangle_\varphi - \langle\gamma_t(\theta,\varphi)\rangle_\varphi \tag{6.37}$$

The first term on the rhs is the average convergence within a circle $\bar{\kappa}(\theta)$. Changing the variables back to lengths we see

$$\langle\gamma_t(\theta,\varphi)\rangle_\varphi = \frac{1}{\pi R^2}\int_{B_R} d^2R'\kappa(R',\varphi') - \langle\kappa(R,\varphi)\rangle_\varphi \tag{6.38}$$

$$= \bar{\kappa}(R) - \langle\kappa(R,\varphi)\rangle_\varphi\,, \tag{6.39}$$

which upon multiplication with the critical surface mass density yields the result (6.23)

$$\Sigma_c\,\langle\gamma_t(R,\varphi)\rangle_\varphi = \bar{\Sigma}(R) - \Sigma(R), \tag{6.40}$$

where we implicitly defined $\Sigma(R) := \Sigma_c\,\langle\kappa(R,\varphi)\rangle_\varphi$ as the angular averaged surface mass density. In this derivation we did not make use of axial symmetry, but rather defined our observable as the angular average of the measured tangential shear. The benefit of this procedure is that we obtained a result, which is valid even for unsymmetric lenses, leading to the validity of equation (6.23) not only for the stacked set of lenses, but for each single lens.

6.5 The Lens-Galaxy Sample

Our goal is to create galaxy catalogues for the haloes identified in large scale cosmological simulations. Due to the limited mass resolution we can only identify haloes above $1.3\times10^{13}\ h^{-1}M_\odot$, i. e. the most massive haloes in the Universe. Consequently we have to look for a galaxy sample that occupies such massive haloes and for which there are well constrained clustering and galaxy-galaxy lensing measurements. A well suited candidate is the Luminous Red Galaxy (LRG) sample that consists of early type galaxies, selected in the Sloan Digital Sky Survey [York *et al.* , 2000] based on cuts in colour and luminosity. The galaxies typically have a strong break at 4000$\mathring{A}$ and a passively evolving stellar population. As the LRGs are strongly clustered and have a low space density, they are an efficient probe of the large scale structure of the Universe, which makes them well suited for cosmological parameter constraints [Tegmark *et al.* , 2006].
LRGs are hosted by a variety of environments from the field to rich clusters, but the majority resides in group to cluster sized haloes [Vikhlinin *et al.* , 1999]. Studies on LRG host halo shapes and masses [Mandelbaum *et al.* , 2006a] have proven that they are good tracers of the most massive galactic haloes.
We use galaxy-galaxy lensing and clustering measurements for the LRG sample from the SDSS by [Mandelbaum *et al.* , 2006a]. The lens sample consists of 43 335 LRGs with spectroscopic redshifts in the range $0.15 < z < 0.35$. The upper cutoff in redshift was chosen in order to have a sufficient number of background galaxies for the lensing.
[Mandelbaum *et al.* , 2006a] split this LRG sample into two equal signal-to-noise bins: LRGfaint and LRGbright. LRGbright is the brightest 1/3 of the total number density $\bar{n}_{tot} = 1.2\times10^{-4}\ h^3\ \mathrm{Mpc}^{-3}$. Properties of the two samples are listed in Table 6.1, and here we also quote estimates for the low mass cutoff of the two samples. The effective redshift of both lens samples is $z_{eff} = 0.24$, leading us to use a simulation snapshot from $z = 0.23$ to calculate our theoretical predictions.

The source sample consists of over 30 million galaxies with r-band magnitude brighter than 21.6 from the SDSS imaging sample. For the shear measurements a Gaussian profile with elliptical isophotes is fit to the data and the **ellipticity components** are calculated

$$(e_+, e_\times) = \frac{1-(b/a)^2}{1+(b/a)^2}(\cos 2\varphi, \sin 2\varphi), \tag{6.41}$$

	$\bar{n}_{\rm meas}[h^3\ {\rm Mpc}^{-3}]$	M_r	$M_{\rm cut}[10^{13}\ h^{-1}M_\odot]$
LRGfaint	4×10^{-5}	<-22.3	2.5
LRGbright	8×10^{-5}	>-22.3	6

Table 6.1: Properties of the LRG subsamples as defined in [Mandelbaum *et al.* , 2006a]. The masses were estimated using the abundance and the Sheth & Tormen mass-function under the assumption that the LRGs occupy the most massive haloes. For the bright sample a hard threshold in mass was assumed for the central galaxies, whereas for the faint sample a top-hat window, with upper cut given by the bright sample, was applied.

where a, b are the lengths of the major axis and φ is the position angle of the major axis. In the weak lensing regime these ellipticity components directly relate to the **shear**

$$(\gamma_+, \gamma_\times) = \frac{1}{2R} \langle (e_+, e_\times) \rangle \,, \tag{6.42}$$

where R is the empirical shear responsivity. One further difficulty arises in the calculation of $\Sigma_{\rm crit}$ for the source-lens setup, since the source galaxies have no spectroscopic redshift information. Here different techniques are used to infer to the photometric redshift distribution for subsamples of the source galaxies and we refer the reader to [Mandelbaum *et al.* , 2006a] for technical details. To estimate the covariance matrices of the measurement, the survey area was split into 200 subregions, from which 2500 bootstrap resamplings were generated.

CHAPTER 7

Methodology

This chapter is devoted to the methods used to examine the N-body simulations and to generate galaxy catalogues. We will start with a short description of the simulations, the N-body code and the halo finder, since most of the results are based on simulation outputs. As the goal is to fit projected correlation functions, to galaxy-galaxy clustering and galaxy-galaxy lensing measurements, we have to develop a method that can perform the calculations fast, for a large range of scales and furthermore exactly. We use a Fast Fourier Transform (FFT) method that works with different box sizes, to obtain the high resolution with reasonable grid sizes and compare this method to a slower, but exact, direct summation method. With these tools at hand we proceed with the fitting procedure and finally comment on redshift space distortions.

7.1 The zHORIZON Simulations

We use the Zürich horizon "zHORIZON" simulations, a suite of 30 pure dissipationless dark matter simulations of the ΛCDM cosmology in which the matter density field is sampled by $N_p = 750^3$ dark matter particles. The box length of 1500 h^{-1}Mpc together with the cosmological parameters given in Table 2.1 then imply a particle mass of $M_{\rm dm} = 5.55 \times 10^{11}\ h^{-1} M_\odot$. This simulation volume enables high precession studies of the fluctuations in the ΛCDM model on scales up to a few hundred comoving megaparsecs [Smith, 2008].
The simulations were carried out on the ZBOX2 and ZBOX3 computer-clusters of the Institute for Theoretical Physics at the University of Zurich using the publicly available GADGET-2 code [Springel, 2005]. This code was used to calculate the nonlinear gravitational evolution of the N equal mass particles. The cosmological parameters are similar to the best fit parameters published by the WMAP team [Spergel *et al.* , 2003, Spergel *et al.* , 2007].
As noted above we are not considering the gas dynamics of the baryons but we have to account for their gravitational potential anyway. This is done by considering the total matter density $\Omega_{\rm m} = \Omega_{\rm b} + \Omega_{\rm dm}$ for the simulations.
The transfer function to initial redshift $z_i = 50$ was calculated using the CMBFAST code of [Seljak & Zaldarriaga, 1996]. For each simulation a realisation of the power spectrum and the corresponding gravitational potential were calculated. Particles were then placed on a cartesian grid of spacing $\Delta x = 2\ h^{-1}$Mpc and displaced according to a second order equivalent of the Zeldovich approximation (see §3.2 on Page 18). The displacements and initial conditions were computed with the 2LPT code of [Scoccimarro, 1998]. We show projections of the dark matter density field at redshifts $z = 20, 10, 3, 2, 1, 0.5$ in Figure 7.1. Here we also see the motion of the particles away from the uniform initial grid and the evolution towards the large scale structure with haloes, filaments and voids.

Unfortunately we can not fully profit from the statistical power of all 30 simulations of the same cosmology because there is no snapshot at the redshift required for our LRG studies in 22 out of the 30 simulations. This limits our effective volume to $V = 27\ h^{-3}\mathrm{Gpc}^3$. In Table 7.1 we quote the redshifts available from the first eight volumes of the zHORIZON simulations. The forces in cosmological N-body simulations have to be softened in order to avoid two particle collisions. The force **softening length** of the simulations used for this work was set to $7 \times 10^{-2}\ h^{-1}\mathrm{Mpc}$ and consequently we should not trust results on scales below the softening length.

snapshot	016	015	014	013	012	011	010	009	008
z	0.0	0.08	0.15	0.23	0.32	0.41	0.51	0.62	0.74

snapshot	007	006	005	004	003	002	001	000
z	0.86	1.00	2.00	3.00	5.00	10.00	15.00	20.00

Table 7.1: Redshifts available from the first eight volumes of the zHORIZON simulations.

7.2 N-Body Codes

Modern cosmology is highly dependent on computer simulations. Due to the lack of analytic formalisms to treat the non-linear gravitational dynamics and hydrodynamics the simulations are sometimes the only way to confront experimental data with theoretical predictions [Bertschinger, 1998].
GADGET-2 is a massively parallel TreeSPH code, which can follow the dynamics of collisionless fluids with the N-body method and can treat ideal gases by the smoothed particle hydrodynamics method (SPH). We however switch off the gas dynamics part since we are mainly interested in large scale effects, which are governed by the collissionless dynamics of the dark matter distribution. For cosmological N-body simulations the direct calculation of the gravitational force needs $\mathcal{O}(N^2)$ operations and is hence computationally expensive and many methods have been invented to perform this task in a more efficient way. In GADGET-2 the gravitational forces can be computed with a pure Tree code, which uses a hierarchical multipole expansion of the gravitational field. To speed the method further up GADGET-2 offers a TreePM method, which uses the exact Tree method for small scales and high speed Fast Fourier Transforms (FFTs) to solve Poissons equation on large scales. These so called particle mesh (PM) methods are the fastest way to calculate gravitational forces, but at scales close to the mesh size the force is heavily suppressed.
In principle the continuous dark matter density field would be described by Boltzmanns equation coupled to Poissons equation in an expanding Friedmann-Lemaître Universe. However, to make the problem computationally treatable the phase space density is sampled by a finite number of tracers. We will refer to these tracers as dark-matter particles, but note that their masses are orders of magnitude above the expected masses for real dark-matter particles such as WIMPs or Axions. The Hamiltonian of the system is given by [Springel, 2005]

$$H = \sum_{i=1}^{N} \frac{\boldsymbol{p}_i^2}{2m_i a^2} + \frac{1}{2} \sum_{i,j=1}^{N} \frac{m_i m_j \varphi(\boldsymbol{x}_i - \boldsymbol{x}_j)}{a}. \tag{7.1}$$

Here we used comoving coordinates and defined canonical momenta by $\boldsymbol{p}_i = a^2 m_i \dot{\boldsymbol{x}}_i$. Periodic boundary conditions are assumed for the box. The Tree code groups distant particles into cells and allows their gravitational action to be accounted for by a single multipole force. So the computation of the gravitational force on a single particle reduces from $\mathcal{O}(N)$ operations to $\mathcal{O}(\log N)$ operations. The accuracy of the method can be adapted to the specific requirements by choosing an appropriate opening criterion, at which the code uses a finer subdivision of space.

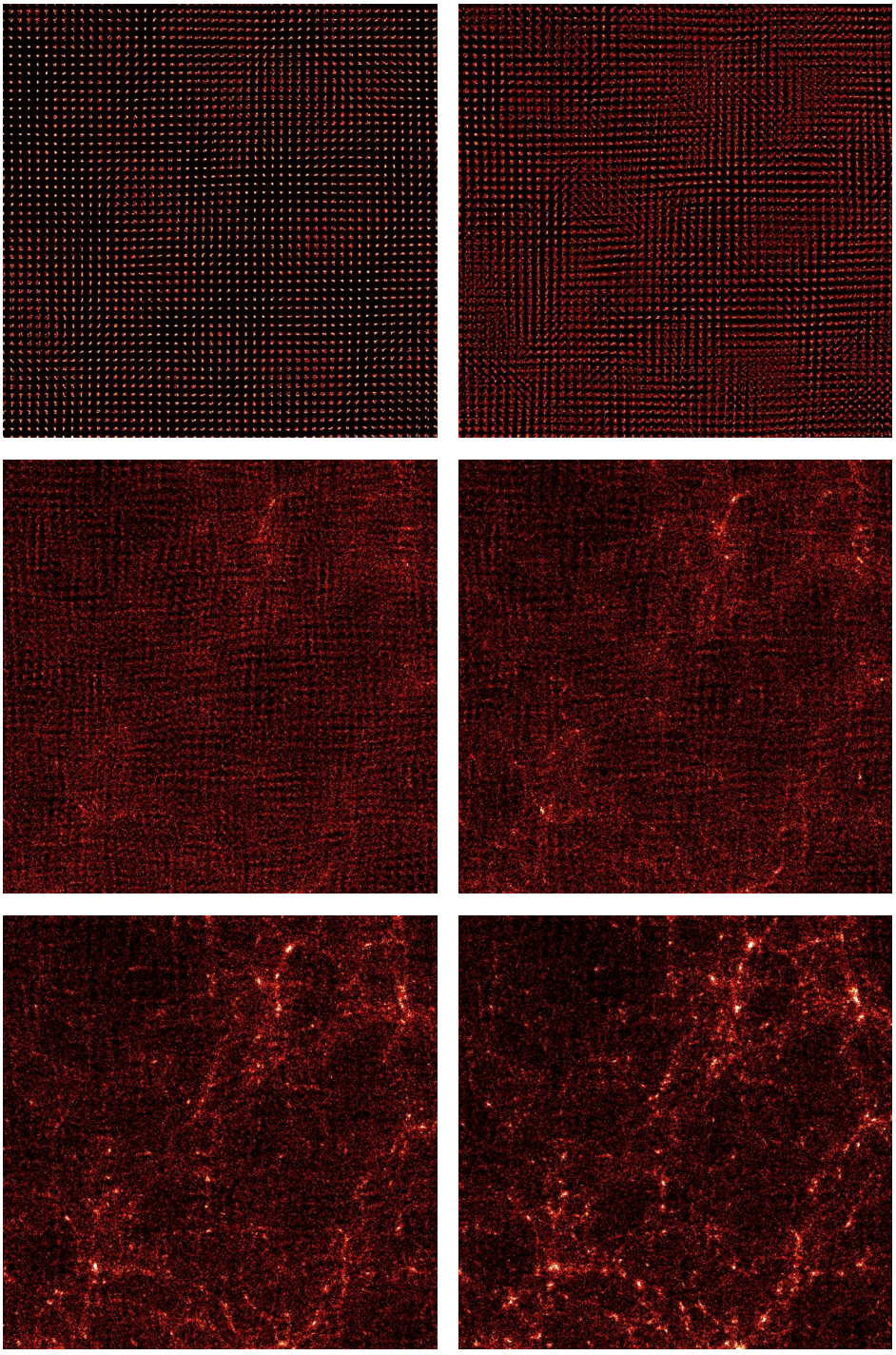

Figure 7.1: Dark matter clustering pattern in the simulations for redshifts $z = 20, 10, 3, 2, 1, 0.5$ from left to right and top to bottom. We show the projection of a slice of thickness $\Delta z = 50\ h^{-1}$Mpc and width $\Delta x = \Delta y = 100\ h^{-1}$Mpc. Note the first picture which shows how the particles are evolving from the initially homogeneous distribution on the grid.

Finally, time integration of the force uses a quasi-symplectic leapfrog scheme with adaptive timesteps.

Boundary Conditions

Cosmological simulations are usually carried out for a cubic domain of space. Conceptually this domain is cut from the surrounding Universe and one must somehow define the boundary conditions. The common solution to this problem is to impose **periodic boundary conditions**

$$\delta(x, y + L, z) = \delta(x, y, z), \tag{7.2}$$

and equivalently for the other directions. With this assumption the Universe is considered as being composed of an infinite number of simulation volumes, glued at their faces.
When we calculate correlation functions and power spectra from the simulation data periodic boundary conditions have to be considered as well. Owing to this fact, we have to reorganise the box before doing the radial averages for $\xi(r)$ according to the scheme drawn in Figure 7.2.

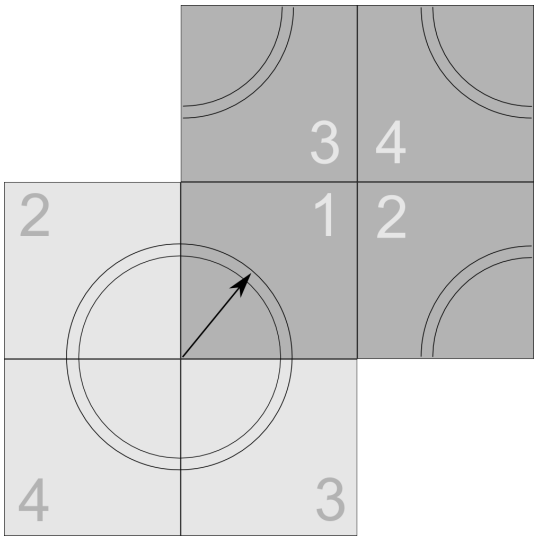

Figure 7.2: Two dimensional scheme of the calculation of the correlation function on the grid. The correlation around the origin of the dark gray field can only be calculated for $r \leq L/2$. We have to consider the periodic boundary conditions and shift the four dark gray subboxes to their corresponding light gray positions.

7.3 Identification of Gravitationally Bound Objects - The Halo Finder

When the evolution of the density field under gravity is finished, we want to investigate the clustering of the dark matter. We already noted that the haloes are a fundamental building block of the large scale structure, leading to the problem of their identification in the dark matter density field. The results of the spherical top-hat collapse model imply that a halo should be a bound dark matter clump of overdensity $\delta \approx 180$ for the Einstein-de Sitter case. There are two main methods that are used for the identification of haloes in the N-body simulations: The so called **spherical overdensity** halo finder [Lacey & Cole, 1994] tries to localise all peaks in the density field and associates all particles in a sphere with mean density 180 times the background density to the halo.
The **Friends-of-Friends** FoF halo finder [Davis *et al.* , 1985] is based on the definition of a **linking length** h. In a first step all particles with separation less than h are identified as friends.

Then a halo is defined as the set of particles that are connected by at least one friendship, i. e. which are friends-of-friends. The linking length has to be carefully chosen in order to identify all structures exceeding a certain threshold ρ. In a simulation with average particle mass M_p a sphere of radius

$$h = \sqrt[3]{\frac{2M_p}{4/3\pi\bar{\rho}}}, \tag{7.3}$$

which is situated in a region with density exceeding ρ will contain on average two or more particles. In turn, in regions exceeding ρ, particles will be typically closer than h and will hence be linked by the FoF algorithm. Another important parameter for the FoF halo finder is the minimum number of particles N_min per halo. This number is used to reject spurious haloes that are formed by particles not belonging to a gravitationally bound object. Thus with a sufficiently high N_min, one will be able to reject all of those spurious objects.
The big advantage of the FoF halo finder, is that it can identify the full triaxial halo profile without imposing a spherical profile. But there are also some shortcomings of the FoF halo finder. The most serious ones are the junction of nearby haloes and the poor distinction of small mass haloes from the background noise.
One possibility to obtain a more robust estimate for the actual halo parameters is to iteratively remove unbound particles. This is done by calculating the particle's potential energy in the gravitational field produced by the other particles of the assumed halo. Then this energy is compared to the particle's kinetic energy. If there are particles with positive total energy then they are considered as unbound and removed.
The dark matter haloes used for this work were identified using the `B-FoF` algorithm kindly provided by Volker Springel, where the linking length was set to 0.2 times the mean interparticle spacing. The minimum particle number per halo was set to $N_\mathrm{min} = 30$, hence the lightest haloes have a mass of $1.65 \times 10^{13}\ h^{-1}M_\odot$.

7.4 Grid Based Analysis I - Basic Principles

As we saw in §4 the correlation function and power spectrum are given by integrals over a continuous density field. In the N-body simulations the dark matter density field is however sampled by a finite number of tracer particles. We have to account for the finite sampling by translating the definitions for the Fourier transforms. The overdensity in k-space is given by a sum over the tracer particles at positions $\boldsymbol{r}_i$

$$\hat{\delta}^\mathrm{d}(\boldsymbol{k}) \quad = \quad \frac{1}{N_\mathrm{p}} \sum_{i=1}^{N_\mathrm{p}} \exp\left[i\boldsymbol{k}\cdot\boldsymbol{r}_i\right] - \delta^\mathrm{D}(\boldsymbol{k}). \tag{7.4}$$

When we calculate the power spectrum of the discrete tracers, the answer will be different from the exact answer for a continuous field. A bit of algebra reveals

$$\left\langle |\delta(\boldsymbol{k})|^2 \right\rangle = \left\langle \left|\delta^\mathrm{d}(\boldsymbol{k})\right|^2 \right\rangle + \frac{1}{N}, \tag{7.5}$$

where the additional term is the **shot noise** [Jing, 2005].
We want to calculate clustering statistics of a vast amount of points in space, making direct summation techniques a bit tedious. So our approach is to interpolate the particles on a cubic mesh and use well developed Fast Fourier Transformations (FFTs) to calculate the spectra. We consider a cubic mesh with spacing $\Delta r = \frac{L}{N_\mathrm{c}}$. Here L denotes the box length ($L = 1500\ h^{-1}$Mpc in our case) and N_c denotes the number of grid cells per dimension.
The FFT can be described by the following conventions for the discrete Fourier transforms

$$\delta(\boldsymbol{x}_i) = \sum_{j=1}^{N_\mathrm{c}^3} \exp\left[-i\boldsymbol{k}_j\cdot\boldsymbol{x}_i\right]\hat{\delta}(\boldsymbol{k}_j), \tag{7.6}$$

$$\delta(\boldsymbol{k}_j) = \frac{1}{N_\mathrm{c}^3} \sum_{i=1}^{N_\mathrm{c}^3} \exp\left[i\boldsymbol{k}_j \cdot \boldsymbol{x}_i\right] \hat{\delta}(\boldsymbol{x}_i), \tag{7.7}$$

where the k-modes are integer multiples of the fundamental mode $k_0 = 2\pi/L$ and all sums run over all grid cells. The Kronecker-Delta on the grid is consequently given by

$$\delta^\mathrm{K}_{kl} = \frac{1}{N_\mathrm{c}^3} \sum_{j=1}^{N_\mathrm{c}^3} \exp\left[i\boldsymbol{k}_j \cdot (\boldsymbol{x}_k - \boldsymbol{x}_l)\right]. \tag{7.8}$$

By Nyquist theorem we are not able to resolve modes above the Nyquist wavenumber

$$k_\mathrm{Ny} = \frac{\pi}{L} N_\mathrm{c}, \tag{7.9}$$

which is equivalent to a minimum resolution of two grid cells. But this is only an upper boundary for the scales at which we can trust the FFT results. In fact there are artefacts caused by convolution and alias (finite sampling) effects that become important already at lower scales. As a first step the N_p particles under consideration[1] are assigned to the cubical mesh. The density at the mesh position $\boldsymbol{x}_i$ can be expressed as a convolution of the assignment filter with the particle field $n(\boldsymbol{r}) = \sum_{j=1}^{N_p} \delta^\mathrm{D}(\boldsymbol{r} - \boldsymbol{r}_j)$

$$n(\boldsymbol{x}_i) = \int d^3r n(\boldsymbol{r}) W(\boldsymbol{r} - \boldsymbol{x}_i) = \sum_{j=1}^{N_p} W(\boldsymbol{r}_j - \boldsymbol{x}_i). \tag{7.10}$$

We use the **nearest gridpoint** (NGP) or **cloud-in-cell** (CIC) mass assignment schemes [Hockney & Eastwood, 1988] with window functions

$$W_\mathrm{CIC}(x - x_i) = \begin{cases} 1 - \frac{|x - x_i|}{\Delta r}, & \text{if } |x - x_i| \leq \Delta r \\ 0, & \text{otherwise} \end{cases} \tag{7.11}$$

$$W_\mathrm{NGP}(x - x_i) = \begin{cases} 1, & \text{if } |x - x_i| \leq \frac{\Delta r}{2} \\ 0, & \text{otherwise} \end{cases} \tag{7.12}$$

The Fourier transform of the density field (7.7) can then be computed using the publicly available `FFTW` routines. The convolution with the window function of the NGP or CIC assignment in real space, leads to a multiplication with the Fourier transformed window in Fourier space. We could thus correct for the convolution by dividing out the Fourier transform of the NGP or CIC window function respectively

$$\delta^c_{\boldsymbol{k}} = \frac{\delta_{\boldsymbol{k}}}{\hat{W}(\boldsymbol{k})}, \tag{7.13}$$

where

$$\hat{W}_\mathrm{CIC}(\boldsymbol{k}) = \prod_{i=1,2,3} \left[\frac{\sin\left(\frac{\pi k_i}{2k_\mathrm{Ny}}\right)}{\left(\frac{\pi k_i}{2k_\mathrm{Ny}}\right)} \right]^2, \qquad \hat{W}_\mathrm{NGP}(\boldsymbol{k}) = \prod_{i=1,2,3} \left[\frac{\sin\left(\frac{\pi k_i}{2k_\mathrm{Ny}}\right)}{\left(\frac{\pi k_i}{2k_\mathrm{Ny}}\right)} \right]. \tag{7.14}$$

A more carefull analysis of [Jing, 2005] reveals that this simple correction scheme is not valid for a field sampled by discrete tracers. In this case the real power spectrum is convolved with the assignment window and iterative schemes have to be used for the recovery of the power spectrum. These corrections are not yet implemented in the code and thus we decide not to use any correction.

Often the analysis of gravitational clustering is carried out in Fourier space. In this case the power spectrum, the clustering strength for a mode of wavenumber k, is the quantity of most interest. From the Fourier-modes on the grid, one can calculate the absolute value and

[1] Here particles refers to DM particles, galaxies and haloes equivalently.

perform a radial averaging of modes in a thin shell around k to obtain an estimator for the power spectrum $P(k) = \left\langle |\delta_k|^2 \right\rangle$.

$$P(k) = \frac{L^3}{C\left(\boldsymbol{k}_i \in [k - dk, k + dk]\right)} \sum_{|\boldsymbol{k}_i| \in [k-dk, k+dk]} P(\boldsymbol{k}_i). \tag{7.15}$$

Here C denotes the number of cells within a bin in k.
We are however interested in a clustering analysis in real space. So why should we calculate the Fourier transformed density field? As we saw in §4, power spectrum $P(\boldsymbol{k}) = |\hat{\delta}_{\boldsymbol{k}}|^2$ and correlation function $\xi(\boldsymbol{r})$ are related by a three dimensional Fourier transform. We will now show that a similar relation is true for the density fields on the grid. To do so, we first write down the definition of the correlation function on the grid, where the spatial average translates to an average over all grid cells

$$\xi(\boldsymbol{r}_i) = \langle \delta(\boldsymbol{x})\delta(\boldsymbol{x} + \boldsymbol{r}_i)\rangle_{\boldsymbol{x}} = \frac{1}{N_c^3} \sum_j^{N_c^3} \delta(\boldsymbol{x}_j)\delta(\boldsymbol{r}_i + \boldsymbol{x}_j). \tag{7.16}$$

This relation can be rewritten using the Fourier transformation (7.6) twice

$$\begin{aligned}
\xi(\boldsymbol{r}_i) &= \frac{1}{N_c^3} \sum_m^{N_c^3} \delta(\boldsymbol{x}_m)\delta(\boldsymbol{r}_i + \boldsymbol{x}_m) && (7.17)\\
&= \frac{1}{N_c^3} \sum_m^{N_c^3} \left\{ \sum_j^{N_c^3} \exp\left[-i\boldsymbol{k}_j \cdot \boldsymbol{x}_m\right]\delta(\boldsymbol{k}_j) \right\} \left\{ \sum_l^{N_c^3} \exp\left[i\boldsymbol{k}_l \cdot (\boldsymbol{x}_m + \boldsymbol{r}_i)\right]\delta^\dagger(\boldsymbol{k}_l) \right\} && (7.18)\\
&= \frac{1}{N_c^3} \sum_m^{N_c^3} \sum_{j,l}^{N_c^3} \exp\left[i\boldsymbol{k}_l \cdot \boldsymbol{r}_i\right] \exp\left[i\boldsymbol{x}_m \cdot (\boldsymbol{k}_l - \boldsymbol{k}_j)\right]\delta(\boldsymbol{k}_j)\delta^\dagger(\boldsymbol{k}_l) && (7.19)\\
&= \sum_j^{N_c^3} \exp\left[i\boldsymbol{k}_j \cdot \boldsymbol{r}_i\right]\delta(\boldsymbol{k}_j)\delta^\dagger(\boldsymbol{k}_j). && (7.20)
\end{aligned}$$

For the last equality we used the Delta function (7.4). We see that the three dimensional correlation function $\xi(\boldsymbol{r}_i)$ on the grid can be obtained by calculating a Fourier transform (7.6) of $\delta^\dagger(\boldsymbol{k}_j)\delta(\boldsymbol{k}_j)$. Hence, we first calculate the the absolute value $\delta^\dagger(\boldsymbol{k}_j)\delta(\boldsymbol{k}_j)$ for each mode on the grid and then use the inverse FFT to calculate $\xi(\boldsymbol{r}_i)$. For this procedure the assumption of spherical symmetry of the correlation function is not required, which allows us to study redshift space distortions. Finally, averaging in radial bins provides an estimator for $\xi(r)$.
We already noted that the FFT technique is limited to scales larger than the grid size $r > \Delta r$. Consequently small scales can only be resolved if one increases the number of grid cells. In §7.6 we will show how this can be circumvented.

7.5 Projected Correlation Functions

Even if there is a spectroscopic redshift measurement, the radial distance as inferred from Hubbles law is obscured by the peculiar motions of the galaxies within their clusters and the large scale flows towards overdensities in the large scale structure. It is very difficult to account for all these effects and a perfect reconstruction of the real space correlation from the measured redshift space correlation is infeasible in practice. What we however can do is to integrate the correlation along the line of sight, i. e. count all particles that are within a cylindrical shell around a certain galaxy. This quantity has the advantage, that integrating along the line of sight over a sufficiently long distance can average out the distortions. Calculated for dark matter–galaxy pairs, the projected galaxy-matter cross-correlation, is furthermore closely related to gravitational lensing.

For a given radially averaged correlation function $\xi(r)$ the projected correlation is given by an integral along the line of sight

$$w(R) = \int_{-\chi_{\max}}^{\chi_{\max}} \xi(\sqrt{R^2+\chi^2}) d\chi \tag{7.21}$$

$$= 2\int_{R}^{\sqrt{R^2+\chi_{\max}^2}} \xi(x) \frac{x}{\sqrt{x^2-R^2}} dx. \tag{7.22}$$

Here we used isotropy and symmetry of the correlation to rewrite the boundaries. In practice we spline-fit the measured correlation function $\xi(r_i)$ and numerically integrate the spline fitted function.
If $\xi(r)$ follows a power law $\xi(r) = (r/r_0)^{-\gamma}$, then the above integral can be calculated for $\chi_{\max} \to \infty$

$$w(R) = r_0 \left(\frac{r}{r_0}\right)^{1-\gamma} \frac{\Gamma(1/2)\Gamma(\gamma/2-1/2)}{\Gamma(\gamma/2)}. \tag{7.23}$$

We see that for a power law correlation the projection follows a power law too, but with a shallower slope.
Another possibility to calculate $w(R)$ is to consider the full three dimensional correlation function $\xi(\boldsymbol{r})$ and integrate it along the line of sight

$$w(R) = \int_{-\chi_{\max}}^{\chi_{\max}} \xi(x, y, \chi) d\chi. \tag{7.24}$$

We use this method when we calculate the projections from the simulation data, since the above method uses the full information about the distribution of the particles and isotropy is not required. Using our FFT method we obtain a gridded correlation function $\xi(x_i, y_j, z_k)$ and from it we can calculate

$$w(x_i, y_j) = \sum_{k=-k_{\max}}^{k_{\max}} \xi(x_i, y_j, z_k) \Delta z, \tag{7.25}$$

where $k_{\max}$ is chosen to satisfy $z_{k_{\max}} = \chi_{\max}$. The above result can then be averaged over a circular annulus to yield an estimate for $w(R_s)$ in a radial bin

$$w(R_s, R_{s+1}) = \frac{1}{C\left(R_s < \sqrt{x_i^2+y_j^2} < R_{s+1}\right)} \sum_{(i,j):R_s<\sqrt{x_i^2+y_j^2}<R_{s+1}} w(x_i, y_j). \tag{7.26}$$

Here we used C to denote the total number of grid cells with radii between the bin boundaries. This procedure is especially useful if we want to estimate projected quantities in redshift space, where the integration of the redshift space monopole of the correlation function as in Equation (7.22) would not lead to the correct answer.
Finally we shall also require $\Delta w(R_s, R_{s+1})$, this can be obtained by first computing

$$\bar{w}(R_s) = \frac{1}{C\left(\sqrt{x_i^2+y_j^2} < R_s\right)} \sum_{(i,j):\sqrt{x_i^2+y_j^2}<R_s} w(x_i, y_j). \tag{7.27}$$

This is however only the value at the bin boundary. In fact we would have to average $\bar{w}(R)$ over the bin (R_s, R_{s+1}) to obtain the quantity corresponding to $w(R_s, R_{s+1})$. Numerically this would require us to measure $\bar{w}(R)$ for a number of radii within a bin and sum over the appropriately weighted contributions. For the sake of speed we will choose another approach. Assuming a shallow slope we can approximate $\bar{w}(R)$ by a straight line

$$\bar{w}(R) = \bar{w}(R_s) + \frac{\bar{w}(R_{s+1}) - \bar{w}(R_s)}{R_{s+1} - R_s}(R - R_s) \quad \forall R \in (R_s, R_{s+1}). \tag{7.28}$$

The average is then given by

$$\bar{w}(R_s, R_{s+1}) = \frac{2}{R_{s+1}^2 - R_s^2} \int_{R_s}^{R_{s+1}} R' dR' \bar{w}(R') \tag{7.29}$$

$$= \bar{w}(R_s) + \frac{1}{3}\left[\bar{w}(R_{s+1}) - \bar{w}(R_s)\right] \frac{2R_{s+1}^3 - 3R_sR_{s+1}^2 + R_s^3}{(R_{s+1}+R_s)(R_{s+1}-R_s)^2}. \tag{7.30}$$

Finally we can calculate the bin value for $\Delta\Sigma$

$$\Delta\Sigma(R_s, R_{s+1}) = \bar{\rho}\Big[\bar{w}(R_s, R_{s+1}) - w(R_s, R_{s+1})\Big]. \tag{7.31}$$

We discussed extensively how the excess surface mass density can be derived from the cross-correlation function and its projection. Especially in terms of lensing one might want to go the reverse way and calculate the projected correlation function $w_{\rm gm}$ from the measured $\Delta\Sigma_{\rm gm}$. As a first step we differentiate (6.23) w. r. t. R

$$\Delta\Sigma'(R) = -\frac{2}{R}\left[\frac{2}{R^2}\int_0^R d\tilde{R}\tilde{R}w(\tilde{R}) - w(R)\right] - w'(R) \tag{7.32}$$

$$= -\frac{2}{R}\Delta\Sigma(R) - w'(R). \tag{7.33}$$

We obtain an equation that relates $\Delta\Sigma(R)$ and its radial derivative to the derivative of $w(R)$. Integration of this relation from a fiducial radius R_0 to R yields

$$w(R) = \int_{R_0}^R w'(\tilde{R})d\tilde{R} + w(R_0) \tag{7.34}$$

$$= -\int_{R_0}^R \left\{\frac{2}{\tilde{R}}\Delta\Sigma(\tilde{R}) + \Delta\Sigma'(\tilde{R})\right\} d\tilde{R} + w(R_0). \tag{7.35}$$

Hence this method determines the projected correlation function up to the amplitude $w(R_0)$. In principle w can then be used to calculate $\xi(r)$ using an Abel integral equation. All this reasoning assumed that we have perfect knowledge about $\Delta\Sigma(R)$ and its derivative. In practice one has to measure $\Delta\Sigma$ in relatively coarse bins to get sufficient signal-to-noise, but even in this case the bin entries will be noisy. An integration of this noisy signal and the even noisier derivative will obscure the result in Equation (7.35). So we conclude that there is not much hope to obtain useful results by this inversion method. It should be much more efficient to confront measured excess surface mass densities directly with the theoretical prediction.

7.6 Grid Based Analysis II - Density Superposition

The grid based clustering analysis described in §7.4 has the problem that its resolution is limited to two grid spacings. Increasing the number of cells per dimension helps to obtain a higher resolution, but with the cost of grid sizes growing by the third power of the refinement. Since it is our goal to resolve the clustering down to $r_{\rm min} \approx 0.1\ h^{-1}$Mpc this would require a FFT with $N_{\rm c} = 15000^3$. In the following we will describe a technique that we have developed to estimate small scale power spectra and correlation functions from cosmological simulations using Fourier transforms. This technique was first introduced by [Jenkins *et al.* , 1998, Smith *et al.* , 2003]. To become familiar with the method we consider a one dimensional grid $\mathcal{G}$ with N cells and length L. Furthermore, we assume that a density field on $x \in (0, L)$ has been assigned to the grid points using one of the mentioned assignment schemes. We now partition the fine grid $\mathcal{G}$ using a coarse grid $\tilde{\mathcal{G}}$ with M grid cells as shown in Figure 7.3.

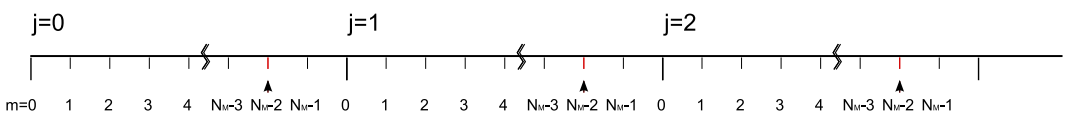

Figure 7.3: One dimensional grid partitioned into M coarse grid cells indexed by j.

The density at an arbitrary point x_l of $\mathcal{G}$ can then be written as

$$\delta(x_l) = \delta\left(x_m + j\frac{L}{M}\right), \tag{7.36}$$

where x_m is the position of the particle within the j-th coarse mesh cell. Inspired by our previous notes on the grid based analysis, we will now perform a FT of the density on above introduced mesh

$$\hat{\delta}(k_s) = \frac{1}{N}\sum_{l=0}^{N-1} \exp\left[ik_s x_l\right]\delta(x_l). \tag{7.37}$$

We may now split the sum into one over all the coarse-mesh-cells $j \in [0, M-1]$ and one over the cell positions within the first coarse-mesh-cell $x_m \in [0, L/M]$.

$$\begin{aligned}\hat{\delta}(k_s) &= \frac{1}{N}\sum_{m=0}^{N_M-1}\sum_{j=0}^{M-1} \exp\left[ik_s\left(x_m + j\frac{L}{M}\right)\right]\delta\left(x_m + j\frac{L}{M}\right) &(7.38)\\ &= \frac{1}{N}\sum_{m=0}^{N_M-1} \exp\left[ik_s x_m\right]\sum_{j=0}^{M-1} \exp\left[ik_s j\frac{L}{M}\right]\delta\left(x_m + j\frac{L}{M}\right). &(7.39)\end{aligned}$$

Here we introduced $N_M := N/M$ to denote the number of fine mesh cells within one coarse mesh cell. If we now choose our fundamental mode for the FT as

$$k_0 = M\frac{2\pi}{L} \Rightarrow k_s = sk_0, \tag{7.40}$$

the exponential $\exp\left[ikjL/M\right]$ in (7.39) vanishes, and by defining $\tilde{\delta}(x_l) := \sum_j \delta(x_l + jL/M)$ we can write

$$\hat{\delta}(k_s) = \frac{1}{N}\sum_{m=0}^{N_M-1} \exp\left[ik_s x_m\right]\tilde{\delta}(x_m). \tag{7.41}$$

This means that we have to perform a FT for the N_M cells of the first coarse grid cell and obtain the correct density field for the modes $\hat{\delta}(k_s)$.
If we wanted to increase the range of correlation functions or power spectra obtained using the FFT techniques described in §7.4, we would have to increase the number of cells per dimension by a factor M, which consequently would increase the size of the arrays by a factor M^3 in the 3-d case. This can easily lead to large arrays and FFTs. Instead of performing a N^3 FFT we could take the box, partition it using a coarse grid with M cells per dimension and then put a reasonable Fourier grid of dimension $N_M = N/M$ on each of the coarse grid cells. By summing up the contributions of all corresponding points in the coarse grid cells and performing the FFT for the summed subgrid (7.41), we obtain an estimate for the high k, small scale modes with a reasonable amount of operations. Compared to a M times larger grid we loose the modes

$$k_s = sR\frac{2\pi}{L} \quad R = 1\ldots M-1, s = 0\ldots N_M - 1, \tag{7.42}$$

equivalently we are considering only each M-th mode.
The correlation function can now be obtained by transforming the absolute value of the modes back to real space

$$\begin{aligned}\tilde{\xi}(x_q) &= \sum_{s=0}^{N_M-1} \exp\left[-ik_s x_q\right]\hat{\delta}(k_s)\hat{\delta}^{\dagger}(k_s) &(7.43)\\ &= \frac{1}{N^2}\sum_{s,l,m=0}^{N_M-1} \exp\left[ik_s(x_l - x_q - x_m)\right]\tilde{\delta}(x_l)\tilde{\delta}(x_m) &(7.44)\\ &= \frac{1}{N}\sum_{m=0}^{N_M-1} \tilde{\delta}(x_m + x_q)\tilde{\delta}(x_m), &(7.45)\end{aligned}$$

where $x_q \in (0, L/M)$ and we introduced $\tilde{\xi}$ to account for the fact that this result is obtained on the grid $\tilde{\mathcal{G}}$ with N_M cells. The first equality follows from the correspondence of power spectrum and correlation function and in the second line we plugged in (7.41) twice. The last equality

then follows from the Kronecker Delta emerging from the sum over s. The above expression can be recast if we use the definition of $\tilde{\delta}$

$$\tilde{\xi}(x_q) = \frac{1}{N}\sum_{m=0}^{N_M-1}\sum_{g,j=0}^{M-1}\delta(x_q+x_m+jL/M)\delta(x_m+gL/M) \tag{7.46}$$

$$= \frac{1}{N}\sum_{m=0}^{N_M-1}\sum_{j=0}^{M-1}\delta(x_q+x_m+jL/M)\delta(x_m+jL/M) + \tag{7.47}$$

$$\frac{1}{N}\sum_{m=0}^{N_M-1}\sum_{j\neq g=0}^{M-1}\delta(x_q+x_m+jL/M)\delta(x_m+gL/M) \tag{7.48}$$

$$= \frac{1}{N}\sum_{m=0}^{N-1}\delta(x_q+x_m)\delta(x_m) + \frac{1}{N}\sum_{m=0}^{N_M-1}\sum_{g\neq j=0}^{M-1}\delta\big(x_q+x_m+(j-g)L/M\big)\delta(x_m) \tag{7.49}$$

$$= \xi(x_q) + \frac{1}{N}\sum_{m=0}^{N_M-1}\sum_{j=1}^{M-1}(M-j)\Big[\delta\big(x_q+x_m+jL/M\big)+\delta\big(x_q+x_m-jL/M\big)\Big]\delta(x_m) \tag{7.50}$$

$$= \xi(x_q) + \frac{1}{N}\sum_{m=0}^{N_M-1}\sum_{j=1}^{M-1}(M-j)\Big[\delta(x_q+x_m+jL/M)+\delta\big(x_q+x_m+(M-j)L/M\big)\Big]\delta\big(x_m\big) \tag{7.51}$$

$$= \xi(x_q) + \sum_{j=1}^{M-1}\frac{M}{N}\sum_{m=0}^{N_M-1}\delta\big(x_q+x_m+jL/M\big)\delta\big(x_m\big) \tag{7.52}$$

$$= \xi(x_q) + \sum_{j=1}^{M-1}\xi_M\big(x_q+jL/M\big) = \xi(x_q)+\xi_{\mathrm{corr}}(x_q) \tag{7.53}$$

In the second line we split the double sum over g, j into equal and unequal pairs and used (7.36) to obtain to the third line. The second term in (7.49) is obtained from a shift of the coordinate frame. In (7.50) we re-summed the double sum over the unequal pairs i, g and in (7.51) we substitute $M-j \to j$ after having shifted the density by a full period L. Here ξ_M is used to denote a correlation, in which the averaging is done only over one coarse box. In the last line we see that the result is the desired correlation function on $\mathcal{G}$ plus a correction term arising from the neglected modes. Exact calculation of the correction term leads to the same computational cost as calculating the exact correlation on the grid $\mathcal{G}$. The correction term can be estimated assuming that the average over one cell of the coarse grid $\tilde{\mathcal{G}}$ is equivalent to an average over the full grid $\mathcal{G}$: $\xi_M \approx \xi$.

The three dimensional case is a straightforward generalisation of the above reasoning and using the notation $\boldsymbol{j} = j_x\boldsymbol{e}_x + j_y\boldsymbol{e}_y + j_z\boldsymbol{e}_z$ finally yields

$$\tilde{\xi}(\boldsymbol{x}_q) = \xi(\boldsymbol{x}_q) + \sum_{j_x,j_y,j_z=1}^{M-1}\xi_M\big(\boldsymbol{x}_q+\boldsymbol{j}L/M\big) \tag{7.54}$$

$$= \xi(\boldsymbol{x}_q) + \xi_{\mathrm{corr}}(\boldsymbol{x}_q) \tag{7.55}$$

The correlation is a monotonically decreasing function of r and hence we need to estimate the magnitude of the argument of $\xi_M\big(\boldsymbol{x}_q+\boldsymbol{j}L/M\big)$ from below in order to find an upper bound for $\xi_{\mathrm{corr}}(r)$.

$$\boldsymbol{x}_q^2 + \boldsymbol{j}^2\left(\frac{L}{M}\right)^2 - 2|\boldsymbol{x}_q||\boldsymbol{j}|\frac{L}{M} \leq \left|\boldsymbol{x}_q+\boldsymbol{j}\frac{L}{M}\right|^2 \tag{7.56}$$

Finally we are interested in the angular average of the correlation function and thus set $r = |\boldsymbol{x}_q|$.

$$\xi_{\mathrm{corr}}(r) \leq \sum_{j_x,j_y,j_z=1}^{M-1}\xi\left(\sqrt{r^2+|\boldsymbol{j}|^2\,(L/M)^2 - 2r|\boldsymbol{j}|L/M}\right). \tag{7.57}$$

If we assume a power law correlation $\xi(r) = \alpha r^{-\gamma}$, we can estimate the effect of the correction.

$$\frac{\xi_{\text{corr}}(r)}{\xi(r)} \leq \sum_{j_x,j_y,j_z=1}^{M-1} \left(1 + \frac{|\boldsymbol{j}|^2}{r^2}\left(\frac{L}{M}\right)^2 - 2\frac{|\boldsymbol{j}|}{r}\frac{L}{M}\right)^{-\gamma/2} . \tag{7.58}$$

In Figure 7.4 we evaluate Equation (7.58) for three different refinements[2]. Finally we can conclude, that the correlation function obtained in this fashion will be close to the true correlation function only over a certain range of scales. At the small scale end it is limited by the mesh resolution and the corresponding Nyquist wavelength (see Table 7.2), whereas at the large scale end it is limited by the correction term in Equation 7.57.
We calculate the actual correlation functions using a set of different coarse grid sizes and then piece them together at the transition points estimated from the range of validity. If not otherwise stated results are obtained using a $N_c = 512$ FFT grid.

refinement M	1	3	9	12	20	30
λ_{Ny} [h^{-1}Mpc]	5.86	1.95	0.65	0.48	0.19	0.1
box length L_M [h^{-1}Mpc]	1500	500	167	125	75	50

Table 7.2: Resolution of the correlations from FFT when using only each Mth Fourier mode.

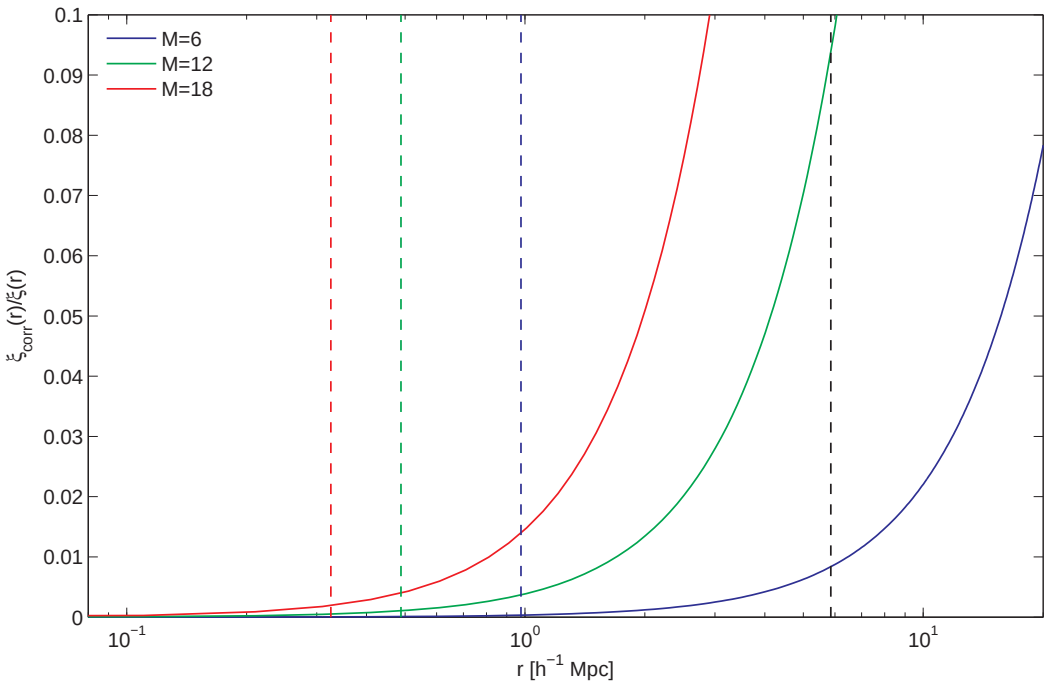

Figure 7.4: Upper bound on the correction term ξ_{corr} for a power law correlation function with slope $\gamma = -1.8$. We show the ratio of correction and real correlation function for three different refinements assuming a box with width $L = 1500\ h^{-1}$Mpc and a FFT with $N_M = 512^3$ cells. The vertical dashed lines show the corresponding Nyquist wavelengths $\lambda_{\text{Ny}} = 2\Delta r$. The black dashed line is for $M = 1$.

[2]The matter correlation in our simulations is well approximated by $\gamma \approx -1.9$ on scales $1\ h^{-1}\text{Mpc} \leq r \leq 50\ h^{-1}\text{Mpc}$.

7.7 Maximum Likelihood Parameter Estimation

We are using data with correlated bin entries. When fitting to these data we hence need to consider the **covariance matrix** of the bin entries x_i

$$C_{ij} = \mathrm{cov}(x_i, x_j) = \langle x_i x_j \rangle - \langle x_i \rangle \langle x_j \rangle . \tag{7.59}$$

The diagonal entries of this matrix contain the variance of the bin entries σ_i^2, whereas the off-diagonal elements describe the correlation of different bin entries. If we assume that the data follow a multi variate Gaussian distribution, the probability density function of the data $\boldsymbol{x}$ given the mean $\boldsymbol{\mu}$ and covariance matrix C reads as

$$f(\boldsymbol{x}, \boldsymbol{\mu}) = \frac{1}{(2\pi)^{p/2} \det C^{1/2}} \exp\left[-\frac{1}{2}(\boldsymbol{x} - \boldsymbol{\mu})' C^{-1} (\boldsymbol{x} - \boldsymbol{\mu})\right]. \tag{7.60}$$

Our model is described by a set of parameters $\boldsymbol{\theta}$, which only indirectly influence the mean vector $\boldsymbol{\mu}$. In our inference we would like to calculate the conditional probability of our model given the data $P(\boldsymbol{\theta}|\boldsymbol{x})$. Using Bayes theorem, this can be related to the conditional probability of the data given the model

$$P(\boldsymbol{\theta}|\boldsymbol{x}) = \frac{P(\boldsymbol{x}|\boldsymbol{\theta}) P(\boldsymbol{\theta})}{P(\boldsymbol{x})}, \tag{7.61}$$

where the a posteriori probability of the data $P(\boldsymbol{x})$ and the prior probability of the model $P(\boldsymbol{\theta})$ are unknown.
For constant priors, the inference depends only on ratios of the **likelihood function**

$$L(\boldsymbol{\theta}|\boldsymbol{x}) := \alpha P(\boldsymbol{x}|\boldsymbol{\theta}). \tag{7.62}$$

The goal of the inference procedure is to maximise the likelihood. For convenience one often works with the natural logarithm of the likelihood and denotes this quantity log-likelihood. For the case of the multivariate Gaussian distribution (7.60) we would have to maximise

$$-\ln L(\boldsymbol{\theta}|\boldsymbol{x}) = \ln (2\pi)^{p/2} \det C + \frac{1}{2}(\boldsymbol{x} - \boldsymbol{\mu})' C^{-1} (\boldsymbol{x} - \boldsymbol{\mu}). \tag{7.63}$$

The first summand is a constant and the second one is a quantity known as the χ^2

$$\chi^2 = (\boldsymbol{x} - \boldsymbol{\mu})' C^{-1} (\boldsymbol{x} - \boldsymbol{\mu}). \tag{7.64}$$

If we are now interested in the probability distribution for a certain parameter we have to **marginalise** over all other parameters. The probability of the data $\boldsymbol{x}$ given one set of parameters $\boldsymbol{\theta}_1$ is given by the sum

$$P(\boldsymbol{x}|\boldsymbol{\theta}_1) = \sum_{\boldsymbol{\theta}_2} P(x|\boldsymbol{\theta}_1, \boldsymbol{\theta}_2) P(\boldsymbol{\theta}_2|\boldsymbol{\theta}_1), \tag{7.65}$$

the last expression under the sum is the probability of parameter set two given a certain value for parameter set one. But as the prior probability of the parameters is unknown, we assume it to be constant and factor it out as a normalisation constant. Again using Bayes law, we can infer the probability of $\boldsymbol{\theta}_1$ given the data

$$P(\boldsymbol{\theta}_1|\boldsymbol{x}) = \frac{P(\boldsymbol{\theta}_1) P(\boldsymbol{\theta}_2|\boldsymbol{\theta}_1)}{P(\boldsymbol{x})} \sum_{\boldsymbol{\theta}_2} P(\boldsymbol{x}|\boldsymbol{\theta}_1, \boldsymbol{\theta}_2). \tag{7.66}$$

Again we have no knowledge about the prefactor so that we use it for normalisation

$$P(\boldsymbol{\theta}_1|\boldsymbol{x}) = \frac{\sum_{\boldsymbol{\theta}_2} P(\boldsymbol{x}|\boldsymbol{\theta}_1, \boldsymbol{\theta}_2)}{\sum_{\boldsymbol{\theta}_1} \sum_{\boldsymbol{\theta}_2} P(\boldsymbol{x}|\boldsymbol{\theta}_1, \boldsymbol{\theta}_2)} = \frac{\sum_{\boldsymbol{\theta}_2} P(\boldsymbol{x}|\boldsymbol{\theta}_1, \boldsymbol{\theta}_2)}{\sum_{\boldsymbol{\theta}} P(\boldsymbol{x}|\boldsymbol{\theta})}. \tag{7.67}$$

The χ^2 distribution

Having performed a χ^2 minimisation as described above, we will have to check how well our model can describe the data. This question can be answered using the χ^2-test (see e. g. [Barlow, 1997]). One expects the deviation of the fit from the data to be around the size of the error of the corresponding measurement leading to a total χ^2 equal to the number of measured points. However, if we minimise χ^2 we have to subtract the number of free parameters from the number of measurements to obtain the number of **degrees of freedom** N_{dof}. The probability distribution for χ^2 is given by

$$f(\chi^2, N_{\mathrm{dof}}) = \frac{2^{-N_{\mathrm{dof}}/2}}{\Gamma(N_{\mathrm{dof}}/2)} \chi^{N_{\mathrm{dof}}-2} \exp\left[-\chi^2/2\right]. \tag{7.68}$$

The important quantity is the probability to get a χ^2 larger than the actual one

$$P(\chi^2, N_{\mathrm{dof}}) = \int_{\chi^2}^{\infty} f(\tilde{\chi}^2, N_{\mathrm{dof}}) d\tilde{\chi}^2. \tag{7.69}$$

The bare χ^2 values resulting from a fitting procedure are usually normalized with the number of degrees of freedom $\tilde{\chi}^2 = \chi^2/N_{\mathrm{dof}}$. We will drop the tilde and quote only the reduced χ^2.

7.8 Generation of LRG Galaxy Catalogues

We are creating galaxy catalogues using the identified haloes from the zHORIZON-simulations. These simulations provide only the dark matter distribution and we can identify virialised dark matter clumps as haloes using a FoF halo finder as described above. If we now want to predict observable quantities we need to understand how certain galaxy types populate the dark matter haloes. The halo occupation distribution (HOD) provides a solution to this problem. This model assumes that there is a relation between halo mass and galaxy luminosity, i.e. certain classes of galaxies live preferentially in haloes of a typical mass. More specifically, the halo occupation distribution assumes that the probability of finding a halo that hosts N_{tot} galaxies depends mainly on the halo mass M. Thus we can write the probability distribution as $P(N_{\mathrm{tot}}|M)$.
If we want to use this model to put galaxies into our simulations we have to answer the following two questions:

1. How many galaxies will reside in a halo of a certain mass?
2. How are they distributed within the halo?

Detailed studies of haloes and subhaloes in N-body simulations [Kravtsov *et al.* , 2004] suggest a division of galaxies into central and satellite galaxies. A popular and reasonable assumption is that there is a central galaxy, which sits at the halo centre of mass and additional satellite galaxies which surround it. The common assumption is that the central galaxy is in general more luminous than the satellites in the same halo.
The mass dependence of the galaxy number has been parametrised in different ways in the literature for threshold samples. For instance [Reid & Spergel, 2008] study LRGs using the Counts in Cylinders statistic and use the following parametrisation to populate their haloes[3][4]

$$N_{\mathrm{cen}}(M) = \frac{1}{2}\mathrm{erfc}\left[-\frac{\ln M/M_{\mathrm{cut}}}{\sigma}\right], \qquad N_{\mathrm{sat}}(M) = \left(\frac{M - M_{min}}{M_1}\right)^{\alpha}, \tag{7.70}$$

where

$$\mathrm{erf}(x) = \frac{2}{\sqrt{\pi}} \int_{-\infty}^{x} \exp\left[-t^2\right] dt \qquad \mathrm{erfc}(x) = 1 - \mathrm{erf}(x). \tag{7.71}$$

[3] They use a spherical overdensity instead of a FoF halo finder to define their haloes
[4] We switched the parameters M_{cut} and M_{min} to avoid confusion with our model.

Furthermore [Padmanabhan *et al.* , 2008] use a similar model when they study the galaxy-quasar cross-correlation.

$$N_{\rm cen}(M) = \frac{1}{2}{\rm erfc}\left[-\frac{\ln M/M_{\rm cut}}{\sqrt{2}\sigma}\right], \qquad N_{\rm sat}(M) = \left(\frac{M-\kappa M_{cut}}{M_1}\right)^{\alpha} \tag{7.72}$$

We will adopt the first parametrisation for our luminosity-threshold sample and an adapted version of it for the luminosity-bin sample. The adaption is necessary because there is a conceptional difference between luminosity-threshold and luminosity-bin samples. A threshold in luminosity can be translated into a threshold in mass by introducing a smoothing of the step to account for the scatter in the luminosity-mass relationship as shown in the above equations. This procedure becomes a bit more involved if one tries to model luminosity bins. Here we in fact have to model an upturn and a decay of the galaxy number, i. e. we will end up with a window. The properties of this window are not clear ab initio, especially the assumption of a symmetric window, which we will consider, is ad hoc and driven by simplicity rather than physical arguments.

7.8.1 General Considerations

The first galaxy put into a halo is assumed to be a central galaxy and is located on the position of the dark matter particle closest to the halo centre of mass. Its velocity is set to the mean halo velocity. Further galaxies are put on randomly chosen dark matter particles, where we take care to avoid two galaxies on the same dark matter particle. The modelling of the mean number of satellites differs for the two LRG samples and will be described in detail below. However, for both samples we draw the actual number of satellites from a Poisson distribution

$$P(N_{\rm sat} = k|\,\langle N_{\rm sat}\rangle) = \frac{\langle N_{\rm sat}\rangle^k}{k!}\exp\left[-\langle N_{\rm sat}\rangle\right]. \tag{7.73}$$

The assumption of a Poisson distribution is again based on subhalo counts in high resolution simulations [Kravtsov *et al.* , 2004]. In such simulations, which resolve both the haloes and their substructure, satellite galaxies can be associated with the subhaloes. Our simulations lack sufficient resolution to do so, and we instead place them on randomly chosen dark matter particles. This approach has the advantage that we can assign the dark matter particles velocity as the galaxy peculiar velocity, which will prove beneficial when we investigate the effect of redshift space distortions. Furthermore an assumption of a density profile for the haloes is not required and we can sample from their full triaxial dark matter distribution. This in turn assumes that the galaxies are distributed around the halo centre like the dark matter.
In the catalogues we save information about the host halo mass and whether the galaxy is a satellite or not, which might be useful for further projects.
The random numbers are generated using the `Fortran` implemented random number generator and are reinitialised using system time at each generation run. Poisson distributed random numbers are generated using a rejection method for $\langle N_{\rm sat}\rangle < 60$ and are drawn from a Gaussian distribution using the Box-Muller transform for higher $\langle N_{\rm sat}\rangle$.

7.8.2 The HOD Adaption Algorithm

For the actual fitting procedure we generate a grid of parameters in the φ-dimensional parameter space spanned by $\{M_1, \alpha, M_{\rm min}, \sigma\}$ and $\{M_1, M_{\rm cut,2}, \alpha, M_{\rm min}, \sigma\}$, for the bright and faint sample respectively[5]. The spacing for α and σ is linear, whereas for M_1, $M_{\rm min}$ and $M_{\rm cut,u}$ we choose linear spacing in $\log_{10}$. Then we use the list of parameter sets to calculate $M_{\rm cut,1}$ or $M_{\rm cut}$ for the faint and bright sample respectively by imposing the number density constraint

$$\int dM n(M)\,\langle N_{\rm tot}\rangle\,(M) = \bar{n}_{\rm meas}. \tag{7.74}$$

[5]For the meaning of the parameters see subsections about faint and bright sample below.

This saves computation time and avoids throwing away most of the galaxy catalogues due to wrong number densities. For the mass function we use a spline fit to the mass function as measured from the simulation, since there are differences at the percent level compared to the Sheth & Tormen description (see Figure 5.1 on Page 34).
This integration over the fitted mass function does not guarantee that we will obtain the actual measured number density for our galaxy catalogue, since the actual density is subject to Poisson noise. Therefore we include the number density in our χ^2, which is then a combination of contributions from the galaxy-galaxy lensing, the galaxy-galaxy clustering and the number densities

$$\begin{aligned}
\chi^2_{\bar{n}} &= \left(\frac{\bar{n}_{\mathrm{sim}} - \bar{n}_{\mathrm{obs}}}{\sigma_{\mathrm{obs}}}\right)^2, \\
\chi^2_{w} &= (\boldsymbol{w}_{\mathrm{sim}} - \boldsymbol{w}_{\mathrm{obs}})\, C^{-1}_{w,\mathrm{obs}}\, (\boldsymbol{w}_{\mathrm{sim}} - \boldsymbol{w}_{\mathrm{obs}})', \\
\chi^2_{\Delta\Sigma} &= (\boldsymbol{\Delta\Sigma}_{\mathrm{sim}} - \boldsymbol{\Delta\Sigma}_{\mathrm{obs}})\, C^{-1}_{\Delta\Sigma,\mathrm{obs}}\, (\boldsymbol{\Delta\Sigma}_{\mathrm{sim}} - \boldsymbol{\Delta\Sigma}_{\mathrm{obs}})', \\
\chi^2_{\mathrm{tot}} &= \chi^2_{\bar{n}} + \chi^2_{w} + \chi^2_{\Delta\Sigma}. \qquad (7.75)
\end{aligned}$$

Here we used vectors $\boldsymbol{\Delta\Sigma}$ and $\boldsymbol{w}$ to account for the fact that we have the data in a binned form and hence $w_i = w(r_i)$ where i is the bin number.
If we considered ϵ parameter realisations per dimension in parameter space, we would have to evaluate ϵ^{φ} points in total. So a scanning of parameter space becomes a computationally demanding task, which has to be tackled using parallelisation strategies. Therefore the list of parameters is split into subsamples, which are then distributed to different nodes on a computer cluster. We used the `ZBOX2` cluster of the University of Zurich, which provides 4 processors per node with a shared memory of 8 GB.
Figure 7.5 gives a schematic overview of the algorithm that we use to generate the galaxy catalogues for the N_{sample} points in parameter space. For each point in parameter space we generate $N_{\mathrm{real}} = 4$ galaxy catalogues on the same simulation and average the calculated statistics over the four realisations to remove part of the scatter, intrinsic to the HOD procedure. To speed these processes up we generate the catalogues using `OPENMP` parallelisation. We loop over the N_{groups} haloes and check whether to put a central or not. If there is a central we put it onto the central dark matter particle and draw the actual number of satellites from the Poisson distribution. The satellites are then distributed on the N_{dm} dark matter particles associated with the halo.
The generation of the galaxy catalogues is relatively memory consuming, since the dark matter particle positions have to be kept in memory for this process. When all catalogues are generated, we deallocate the dark matter positions and load the gridded dark matter distribution for three different coarse grids $M = 3$, $M = 10$ and $M = 20$ to memory. Then we start to evaluate the projected galaxy matter cross correlation and the projected galaxy galaxy autocorrelation. The routines for normalisation of the gridded density field, for calculating the complex product and finally, for calculation of the statistics involve sums over all grid cells and are therefore `OPENMP` parallelised too. In the end we calculate χ^2 as described in Equation (7.75) and store the number densities and χ_{gg}, χ_{Σ} and $\chi_{\bar{n}}$. Using four processors, which have all access to shared memory storage we can generate the four catalogues in about 170 s. The evaluation of the catalogues takes another 270 s, which in total gives 440 s. This means for say $\alpha = 5$ parameters per dimension we need 76 h of computing time.
Further speedup could only be achieved by distributing subsamples of the model list to different nodes of a computer cluster. To our perception there is no further possibility for speedup of the evaluation side. In terms of the catalogue generation a remarkable speedup could be achieved if we did not have to sample from the dark matter distribution. Assuming a profile for the satellite distribution around the halo centre, one would only need the halo positions and masses to determine the galaxy positions. A common assumption in the literature is to distribute the galaxies according to a spherical NFW profile. For the velocities of the satellites one would then have to sample from a velocity distribution. Often one assumes as Gaussian with dispersion σ_v, which for the NFW profile was computed by [Lokas & Mamon, 2001]. This method could be further improved if one accounted for the triaxiality of the halo. This triaxial

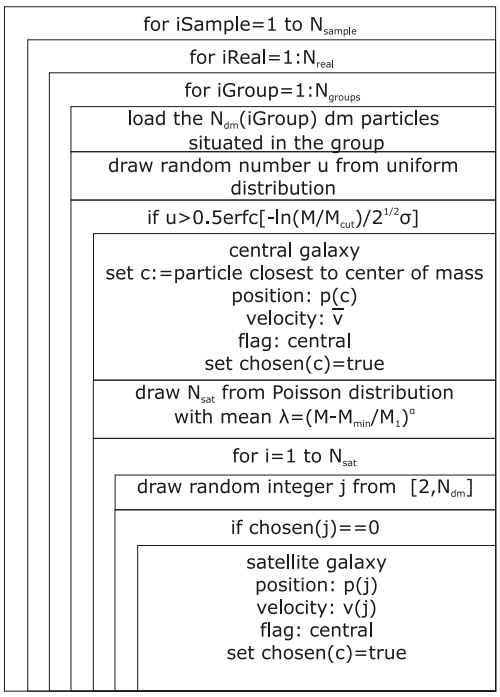

Figure 7.5: Program scheme for the generation of a luminosity threshold galaxy catalogue and N_{sample} sets of HOD parameters. We use N_{real} to denote the number of galaxy catalogues per model over which we average and N_{group} to denote the number of haloes identified in the simulation.

mass distribution can be obtained from the inertia tensor of the halo. The major axes can then be used to map the spherical NFW profile to an ellipsoidal NFW profile.

7.8.3 Modelling of the Bright LRG Sample

The number of central LRGs is either one or zero, i. e. it follows a Bernoulli distribution with success probability p

$$P(N_{\text{cen}} = 1) = p, \qquad P(N_{\text{cen}} = 1) = 1 - p, \tag{7.76}$$

where the expectation value of N_{cen} equals the success probability $\langle N_{\text{cen}} \rangle = p$. In a first step we decide whether a halo hosts a central galaxy, where the mean number of central galaxies follows a step, smoothed with an error function

$$p = \langle N_{\text{cen}} \rangle = \frac{1}{2}\text{erfc}\left[-\frac{\ln M/M_{\text{cut}}}{\sqrt{2}\sigma}\right]. \tag{7.77}$$

This galaxy is put to the centre of the halo and is assigned the peculiar velocity of its host halo as described above. The bright subsample of the SDSS LRGs is a luminosity-threshold sample and hence it is reasonable to assume that the satellites brighter than the threshold will only live in haloes which already host a central galaxy with luminosity exceeding this threshold. This suggests that the probability of $N_{\text{sat}} = k$ satellite galaxies in a halo can be written as

$$P(N_{\text{sat}} = k) = P(N_{\text{sat}} = k|N_{\text{cen}} = 1)P(N_{\text{cen}} = 1) + P(N_{\text{sat}} = k|N_{\text{cen}} = 0)P(N_{\text{cen}} = 0) \tag{7.78}$$

$$= P(N_{\text{sat}} = k|N_{\text{cen}} = 1)P(N_{\text{cen}} = 1) \tag{7.79}$$

$$= P(N_{\text{sat}} = k|N_{\text{cen}} = 1)\langle N_{\text{cen}} \rangle . \tag{7.80}$$

In the first line we used the law of total probability and in the second line we made use of $P(N_{\text{sat}} = k|N_{\text{cen}} = 0) = 0$. So it remains to model the conditional probability for k satellites

given that there is already a central. We will model this number with a Poisson distribution with mean

$$\langle N_{\mathrm{sat}} \rangle_{\mathrm{c}} (M) = \begin{cases} \left(\frac{M - M_{\mathrm{min}}}{M_1} \right)^{\alpha}, & \text{if } M > M_{\mathrm{min}} \wedge N_{\mathrm{cen}} \neq 0 \\ 0, & \text{otherwise} \end{cases} \tag{7.81}$$

Here we introduced the subscript c to account for the fact that this is the conditional expectation value, i. e. the expectation of the satellite number calculated for the haloes hosting a central. The total expectation can now be written as

$$\begin{aligned} \langle N_{\mathrm{tot}} \rangle (M) &= \langle N_{\mathrm{sat}} \rangle (M) + \langle N_{\mathrm{cen}} \rangle (M) && (7.82) \\ &= \sum_k k P(N_{\mathrm{sat}} = k) + \langle N_{\mathrm{cen}} \rangle (M) && (7.83) \\ &= \langle N_{\mathrm{cen}} \rangle (M) \left[\sum_k k P(N_{\mathrm{sat}} = k | N_{\mathrm{cen}} = 1) + 1 \right] && (7.84) \\ &= \langle N_{\mathrm{cen}} \rangle (M) \left[\langle N_{\mathrm{sat}} \rangle_{\mathrm{c}} (M) + 1 \right]. && (7.85) \end{aligned}$$

The above introduced model has five free parameters $\{M_1, M_{\mathrm{cut}}, M_{\mathrm{min}}, \alpha, \sigma\}$, which can be varied to adapt the model to the data. The shape of this distribution is shown in Figure 7.6. When fitting to the data we first calculate M_{cut} for each point in the four dimensional parameter space spanned by $\{M_1, \alpha, \sigma, M_{\mathrm{min}}\}$ demanding for the right abundance.

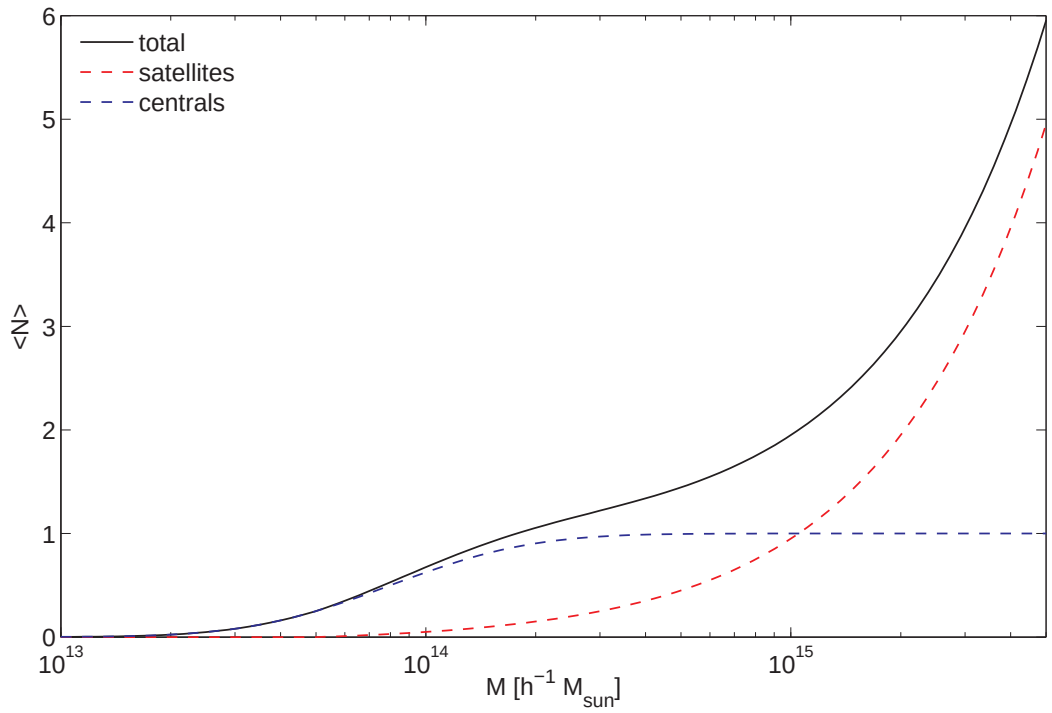

Figure 7.6: Development of the galaxy number with changing mass for the luminosity threshold sample. We show the number of central galaxies (blue dashed), satellite galaxies (red dashed) and the total number of galaxies (black solid). Note that this does not reflect the real distribution we found for our sample.

7.8.4 Modelling of the Faint LRG Sample

The faint subsample of the LRGs is a luminosity-bin rather than a threshold sample. Hence the problem of translation of luminosity-bin into a mass-bin arises. Furthermore we have to drop the requirement that there has to be a central galaxy from the luminosity bin in order to host a

satellite from the same bin. This is due to the fact, that a satellite from this fainter luminosity bin may live in a halo that already hosts a central from the bright sample. In order to simplify our analysis we are not using the galaxy catalogues for the bright sample to generate the satellites, but rather consider centrals and satellites as two independent samples such that the probability for the satellites is independent of the probability for the centrals $\langle N_{\rm sat}\rangle_{\rm c} = \langle N_{\rm sat}\rangle$. Hence the total number of galaxies in a halo can be written as

$$p = \langle N_{\rm tot}\rangle\,(M) = \langle N_{\rm cen}\rangle\,(M) + \langle N_{\rm sat}\rangle\,(M). \tag{7.86}$$

In the first step we consider the central galaxies. The window is modeled as a symmetric, smoothed box shown in Figure 7.7

$$\langle N_{\rm cen}\rangle = \frac{1}{4}\mathrm{erfc}\left[-\frac{\ln M/M_{\rm cut,1}}{\sqrt{2}\sigma}\right]\mathrm{erfc}\left[\frac{\ln M/M_{\rm cut,2}}{\sqrt{2}\sigma}\right], \tag{7.87}$$

where $M_{\rm cut,1} < M_{\rm cut,2}$ and we have $M_{\rm cut,2}$ as an additional free parameter. The functional form ensures $0 \leq \langle N_{\rm cen}\rangle \leq 1$ and is sufficiently variable for our modelling. The satellite number is drawn from a Poisson distribution with mean given by (7.81). Again we calculate $M_{\rm cut,1}$ for each point in the five dimensional parameter space spanned by $\{M_1, M_{\rm cut,2}, M_{\rm min}, \alpha, \sigma\}$, demanding for the right number density according to Equation (7.74).

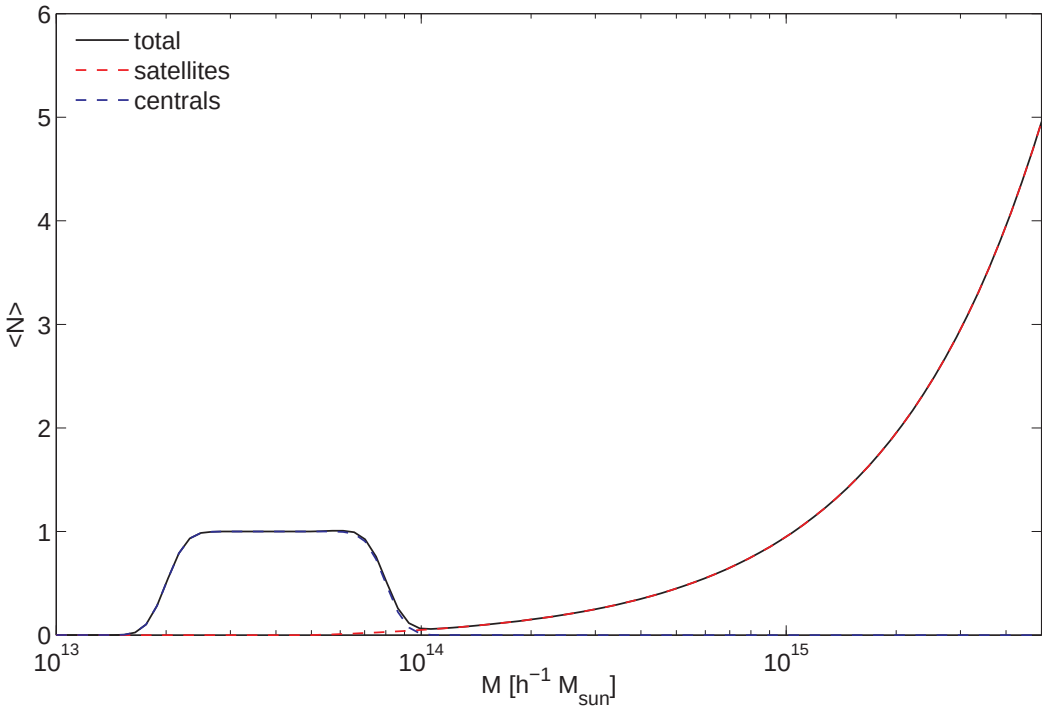

Figure 7.7: Development of the galaxy number with changing mass for the luminosity bin sample. We show the number of central galaxies (blue dashed), satellite galaxies (red dashed) and the total number of galaxies (black solid).

7.9 Redshift Space Distortions

So far we performed our analysis of correlation functions in real space, where the three dimensional position of galaxies and dark matter is known. Concerning observations such a treatment is a bit idealistic, angular positions on the sky can be easily measured, whereas the determination of the distance to a galaxy is a bit more involved. We will in the following discuss the

effects arising in redshift surveys such as the SDSS.
Considering only **Hubble's law**

$$\boldsymbol{u} = H\boldsymbol{r}, \tag{7.88}$$

it seems to be evident to use the recessional velocity $\boldsymbol{u}$ of a galaxy, or equivalently the redshift z of its spectral lines, as a distance measure

$$\chi \approx \frac{z}{H_0} \qquad z \ll 1 \tag{7.89}$$

Three dimensional positions obtained in this fashion are termed **redshift space** positions. However, the assumption of perfect Hubble law distance–velocity relation is distorted by the **peculiar velocities** $\boldsymbol{v}$ of galaxies with respect to the Hubble flow. These peculiar velocities arise from the gravitational instability and hence the apparent clustering in redshift space is different from the real space clustering. However, large galaxy surveys, such as SDSS and 2dFGRS use the redshift as a proxy for distance. Consequently, the statistics derived from these surveys are different from the real space predictions. In this context it is useful to develop an understanding of the consequences of working in redshift rather than real space.
There are essentially two effects, which influence the shape of power spectrum and correlation function measured in redshift space.

large scales On large scales galaxies that fall into clusters lead to a **squashing** of the correlation, i. e. an enhancement of the power spectrum for modes parallel to the line of sight. Galaxies between us and the cluster have an enhanced velocity and seem to be further away than they actually are, whereas galaxies situated at the opposite side of the cluster have a velocity smaller than the Hubble velocity and are hence moved toward us.

small scales On small scales the virial motion or velocity dispersion of galaxies within their host halo leads to an elongation of the cluster along the line of sight. This elongation effect leads to a suppression of the clustering along the line of sight, and is termed the **finger-of-god effect**.

Altogether these effects give rise to a positive quadrupole anisotropy on large scales, which approaches zero at intermediate scales and becomes negative at small scales.
To make the issue more easily tractable we will impose the **plane-parallel approximation**, which states that the redshift axis has a fixed direction (which we take as the x-axis) and we consider only far away regions that subtend a small angle on the sky. Consequently, we can assume the distortions to occur all along this axis. Furthermore, we will neglect the velocity dispersion since it should be subdominant on large and intermediate scales. A more detailed discussion of this limit is presented in [Scoccimarro, 2004].
The relation between redshift space position $\boldsymbol{r}_\mathrm{s}$ and real space position $\boldsymbol{r}$ reads as

$$\boldsymbol{r}_s = \boldsymbol{r} + \frac{\hat{\boldsymbol{x}} \cdot \boldsymbol{v}}{H}\hat{\boldsymbol{x}}. \tag{7.90}$$

Here $\hat{\boldsymbol{x}}$ is the unit vector in x-direction. We will now follow an simplified but analytically tractable argument of [Kaiser, 1987]. As a starting point to calculate the relation between real and redshift space clustering we use the fact that the number of objects is not changed under the distortion.

$$n_s(\boldsymbol{r}_s)d^3r_s = n(\boldsymbol{r})d^3r \qquad \Rightarrow \qquad n_s(\boldsymbol{r}_s) = n(\boldsymbol{r})J \tag{7.91}$$

Here we introduced the Jacobian of the transformation J. As we saw in Equation (7.90) the distortions affect only the radial position and leave the angular coordinates unaffected

$$J = \left|\frac{d^3r}{d^3r_s}\right| = \frac{dr}{dr_s}\frac{r^2}{r_s^2} = \left(1 + \frac{\partial}{\partial x}\left[\frac{\boldsymbol{v}\cdot\hat{\boldsymbol{x}}}{H_0}\right]\right)^{-1}\left(1 + \frac{\boldsymbol{v}\cdot\hat{\boldsymbol{x}}}{H_0 x}\right)^{-2} \tag{7.92}$$

Now Kaiser recognised that large scale modes (corresponding to $k \approx x^{-1}$, where x is the survey dimension) will be sparsely sampled and hence the derivative kv/H is more important than the

correction v/Hx by a factor $kx \ll 1$ for almost all modes. Linearising above equation and dividing by the mean density we arrive at

$$\delta_s = \delta - \frac{\partial}{\partial x}\left[\frac{\boldsymbol{v}\cdot\hat{\boldsymbol{x}}}{H}\right]. \tag{7.93}$$

We can now derive the power spectrum of the redshift space overdensity by performing a Fourier transform

$$\hat{\delta}_s(\boldsymbol{k}) = \delta(\boldsymbol{k}) - i\int d^3r \exp\left[-i\boldsymbol{k}\cdot\boldsymbol{r}\right] f(\Omega_\mathrm{m})\frac{\partial}{\partial x}\int d^3k' \exp\left[i\boldsymbol{k}'\cdot\boldsymbol{x}\right]\delta(\boldsymbol{k})\frac{\boldsymbol{k}'\cdot\hat{\boldsymbol{x}}}{k'^2}. \tag{7.94}$$

In the last equation we used the result (3.24) from linear theory $v(\boldsymbol{k}) = iaHf(\Omega_\mathrm{m})\delta(\boldsymbol{k})/k$, where $f(\Omega_\mathrm{m}) = d\ln D_1/d\ln a$ and D_1 is the growth factor. Hence the real and redshift space density fields are related as

$$\hat{\delta}_{\mathrm{m,s}}(\boldsymbol{k}) = \hat{\delta}_{\mathrm{m,r}}(\boldsymbol{k})\left[1 + f(\Omega_\mathrm{m})\mu^2\right], \tag{7.95}$$

where $\mu = \boldsymbol{k}\cdot\hat{\boldsymbol{x}}/k$. From this it is only a small step to the redshift space power spectrum

$$P_s(k) = P(k)\left[1 + f(\Omega_\mathrm{m})\mu^2\right]^2. \tag{7.96}$$

However, if we want to consider galaxies rather than the underlying dark matter, we have to introduce the bias b. This affects only the first term, since the second is an velocity effect and velocities depend on the dark matter clustering rather than the galaxy clustering. So the relation for the galaxy power spectrum is

$$P_{\mathrm{gg,s}}(k) = P(k)b^2\left[1 + \beta\mu^2\right]^2, \tag{7.97}$$

where $\beta = f(\Omega_\mathrm{m})/b$.
Using above description for the redshift space power spectrum we can now derive the linear theory prediction for the correlation function

$$\begin{aligned}\xi(r,\nu) &= \frac{V}{2\pi^2}\int_{-1}^{1} d\mu \int_0^\infty dk k^2 P_{\mathrm{lin}}(k)\exp\left[i\boldsymbol{k}\cdot\boldsymbol{x}\right]\left[1+\beta\mu^2\right]^2 &(7.98)\\ &= \alpha_0\xi_0(r)L_0(\nu) + \alpha_2\xi_2(r)L_2(\nu) + \alpha_4\xi_4(r)L_4(\nu), &(7.99)\end{aligned}$$

where ν is the angle between $\boldsymbol{r}$ and the line of sight $\nu = \hat{\boldsymbol{x}}\cdot\boldsymbol{r}/r = x/r$, L_l are the Legendre polynomials and the j_i are the spherical Bessel functions ($j_i(x) = \sqrt{\frac{1}{2x}}J_i(x)$). The prefactors introduced in the above equation are defined by

$$\alpha_0 = 1 + \frac{2}{3}\beta + \frac{1}{5}\beta^2, \tag{7.100}$$

$$\alpha_2 = \frac{4}{3}\beta + \frac{4}{7}\beta^2, \tag{7.101}$$

$$\alpha_4 = \frac{8}{35}\beta^2. \tag{7.102}$$

The real space multipoles can be calculated from

$$\xi_i(r) = \frac{V}{2\pi^2}\int_0^\infty dk k^2 P_{\mathrm{lin}}(k) j_i(kr). \tag{7.103}$$

Above result is obtained using the plane wave expansion

$$\exp\left[i\boldsymbol{k}\cdot\boldsymbol{x}\right] = \sum_{l=0}^{\infty}(2l+1)i^l j_l(kr)L_l(\mu)L_l(\nu), \tag{7.104}$$

where ν and μ are the polar angles of $\boldsymbol{r}$ and $\boldsymbol{k}$, respectively. The orthogonality of the Legendre polynomials helps to integrate out the polar angle in Fourier space.

$$\int_{-1}^{1} d\mu L_l(\mu)L_m(\mu) = \frac{2}{2+l}\delta_{lm} \tag{7.105}$$

A contour plot of the redshift space correlation function is shown in Figure 7.8. We are now interested in the projected correlation function $w_{gg}^{(s)}(R)$ and have to perform an integration of (7.99) along the line of sight.

$$w_{gg}^{(s)}(R) = \int_{-\chi_m}^{\chi_m} \xi(r,\nu) d\chi = \tag{7.106}$$

$$= 2\int_0^{\chi_m} \xi\left(\sqrt{\chi^2+R^2},\nu\right)_{\nu=\frac{\chi}{\sqrt{\chi^2+R^2}}} d\chi \tag{7.107}$$

$$= 2\int_0^{\chi_m} \left\{\alpha_0\xi_0\left(\sqrt{\chi^2+R^2}\right)L_0(\nu) + \alpha_2\xi_2\left(\sqrt{\chi^2+R^2}\right)L_2(\nu) + \alpha_4\xi_4\left(\sqrt{\chi^2+R^2}\right)L_4(\nu)\right\}_{\nu=\frac{\chi}{\sqrt{\chi^2+R^2}}} d\chi \tag{7.108}$$

Above result can be used to calculate the linear theory predictions for the projected correlation functions in redshift space.
In the simulations we are using comoving coordinates and measure positions in units of h^{-1}Mpc. Hence in the distant observer approximation redshift space displacements can be assigned by

$$\boldsymbol{r}_s = \boldsymbol{r} + \frac{\boldsymbol{v}\cdot\hat{\boldsymbol{z}}}{100}. \tag{7.109}$$

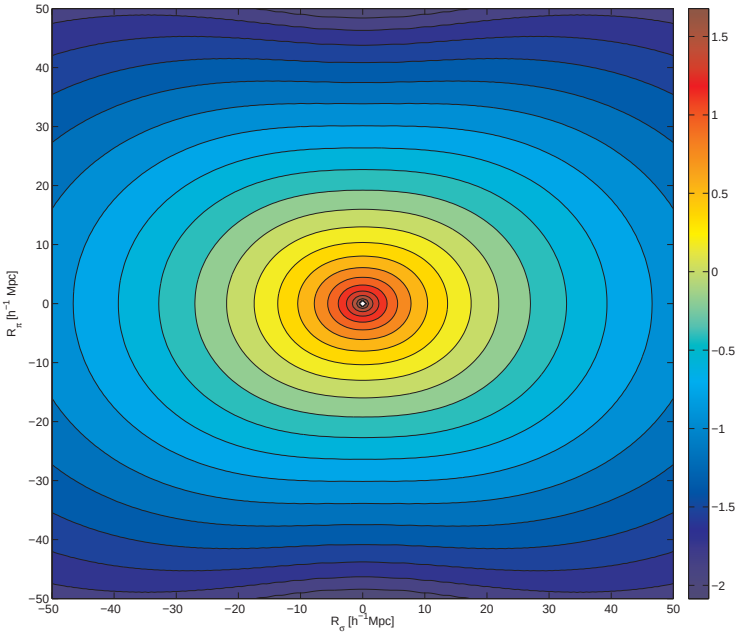

Figure 7.8: Contour plot of the 10-based logarithm of the galaxy autocorrelation function calculated using Kaiser's approximation. Horizontal R_σ axis is transverse to the line of sight R_π. The plot was generated assuming a bias of $b = 2.2$

CHAPTER 8

Results

After having laid down the basic theory and having explained our methodology we will now proceed to describe our findings. We start with the discussion of our new FFT based algorithm for the calculation of correlation functions. Then we will continue with the HOD fitting: Starting with an investigation of the influence of the HOD parameters on the spectra, we will pursue with the discussion of the best fit HOD for the bright and faint LRG sample. These best fit models are used afterwards to investigate the behaviour of the cross-correlation coefficient and to develop a new technique for the recovery of the dark matter correlation function. Subsequently, we will quantify the influence of redshift space distortions on projected correlation functions. Finally we will comment on a different scheme for the galaxy distribution and the effect of spatial resolution on our results.

8.1 Correlation Functions from the Grid Based Analysis

In Figure 8.1 we compare the matter-matter autocorrelation function ξ_{mm} obtained with a 1024-cell FFT method to the result obtained with a tree based direct summation method. We show both correlation functions and their fractional difference, as well as the galaxy-galaxy autocorrelation function ξ_{gg} and the galaxy-matter cross-correlation function ξ_{gm} for a LRG catalogue. The matter autocorrelation is chosen for this comparison, since the large number of dark matter particles provides the lowest noise on the correlation function and thus facilitates the extraction of the differences of the two calculation techniques. The FFT based correlation agrees with the direct summation result to better than 3% on scales between $1\ h^{-1}\mathrm{Mpc} \leq r \leq 60\ h^{-1}\mathrm{Mpc}$. The fractional difference becomes less well constrained above that scale. In this context it is important to note that the dark matter correlation calculated by the direct summation method uses only a subset of the full dark matter distribution. One randomly samples from the dark matter particles to make the computations faster. The results we compare to are obtained from a sampling of $\tilde{N}_{\mathrm{p}} = 1 \times 10^6$, corresponding to a dilution by a factor $\tilde{N}_{\mathrm{p}}/N_{\mathrm{p}} \approx 1/470$. This relatively coarse subsampling is possible since the variance of the power spectrum and correlation function is affected by shot noise, which is proportional to $1/\tilde{N}_{\mathrm{p}}$. Around the BAO scale there are fluctuations on the 5% level in the direct summation code that arise from the sampling. Furthermore we note that the FFT based method shows unphysical artefacts when one approaches the Nyquist wavelength. These effects become especially pronounced if the sample under consideration has a low number density. We conclude that besides of the first promising results, there are still some systematic effects, about which we have to gain a better understanding.

The FFT based method is trivially parallelisable and the computation time for the correlation

function is dominated by the calculation of an effective FFT scheme and the mass assignment.

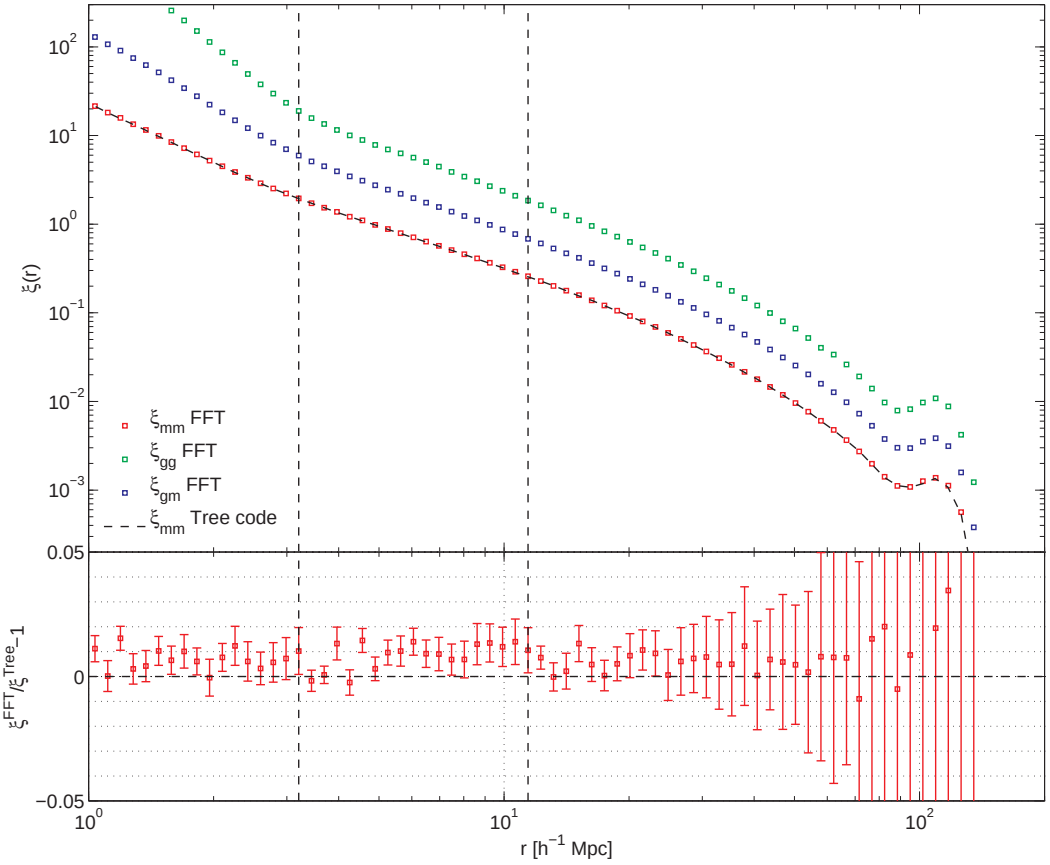

Figure 8.1: *Top panel:* Comparison of the correlation functions obtained from our FFT method and with the direct summation code. Coloured squares show the matter autocorrelation (red), galaxy-matter cross-correlation (blue) and galaxy autocorrelation (green), whereas the dashed line shows the matter correlation from the direct summation. Note that our method is exact on the 3% level over a wide range of scales. The vertical dashed lines are included to show the radial scale at which we stack the correlations obtained with different resolution FFTs. We show correlations from an ensemble average over eight simulations. *Bottom panel:* Fractional difference of the two measurements and associated standard deviation over the eight simulation volumes. Our method provides an efficient method to probe the clustering around the BAO scale at $r \approx 105\ h^{-1}$Mpc.

8.2 Generation of LRG Galaxy Catalogues

We decided to use an algorithm based on a grid of parameters to obtain a HOD that can reproduce the galaxy-galaxy clustering, the galaxy-galaxy lensing and the abundance of the sample. Therefore we generate $\epsilon = 5$ different values for each of the φ parameters to be estimated. This gives a total of 5^{φ} models, for which galaxy catalogues have to be generated and the clustering statistics have to be calculated. The spacing of the parameters is chosen linear for σ, α and logarithmic for $M_1, M_{\rm cut}, M_{\rm min}$. In Table 8.1 we quote the limits of the parameter space. For the actual fitting we used the full covariance matrix provided by Mandelbaum et al. and an error of 10% on the abundance $\bar{n}$. In total we have 55 data points and 4/5 free parameters, i.e. the number of degrees of freedom amounts to $N_{\rm dof} = 51/50$ for the bright and faint sample respectively.
Table 8.2 shows the results for the best fit HOD parameters together with the resulting χ^2.

	bright		faint	
M_1	5	80	8	80
$M_{\mathrm{cut},2}$	–	–	3	20
M_{min}	2	60	3	40
σ	0.1	2.2	0.2	2
α	0.1	2.0	0.05	1.5

Table 8.1: Limits on the grid of HOD parameters used for the fitting, the spacing is linear for α, σ and linear in $\log_{10}$ for the masses. The masses are given in units of $10^{13}\ h^{-1}M_{\odot}$.

	χ^2	$\bar{n}$	M_1	$M_{\mathrm{cut,l}}$	$M_{\mathrm{cut,u}}$	α	σ	M_{min}	model
bright	4.47	4.78	40	17.8	—	1.05	1.68	4.6	434
bright-d	1.24	4.73	10	17.8	—	0.1	1.68	25.6	144
faint	8.02	9.36	45	5	12.4	0.4	1.55	5.7	2284

Table 8.2: Best fit parameters for the faint and bright sample obtained with the full covariance matrix. For comparison we also quote the HOD for a fit of the bright sample using the diagonal errors only. The number densities are in units of $1 \times 10^{-5}\ h^3\ \mathrm{Mpc}^{-3}$, masses in units of $10^{13}\ h^{-1}M_{\odot}$. Note that we quote the reduced χ^2.

8.2.1 Influence of the HOD Parameters on the Projected Correlations

In Figure 8.2 we examine the effect of the variation of single HOD parameters on the shape of the projected correlation function for the bright LRG sample. We show the correlation of a fiducial model in green, for lower value of the parameter under consideration in red and for a higher value in blue.

The top left panel of Figure 8.2 shows variation of M_1. As expected, lower M_1 leads to more satellites and hence to a strong increase of the small scale clustering and the overall bias, since the bright LRG satellites live in high mass, high bias haloes. A higher value for M_1 causes less satellites and hence smaller clustering on small scales. The variation of M_{cut} is shown in the top right panel of Figure 8.2. The cutoff mass influences on the one hand the total number of centrals, but on the other hand includes or excludes intermediate mass haloes. A high M_{cut} (blue) emphasises the influence of the higher biased, high mass haloes and hence leads to an increased overall clustering amplitude. The satellite slope α is varied in the centre left panel of Figure 8.2, it influences the number of satellites as it either leads to a high number of satellites in the rare high mass haloes or to intermediate satellite numbers for the more abundant low mass haloes. A lower value (red) increases the satellite number and thus the small scale clustering. Changing α by a factor of 2 has no effect on the overall clustering amplitude, since this parameter influences only the slope of the satellite fraction. The centre right panel of Figure 8.2 shows a variation of M_{min}, this is a cutoff and normalisation scale for the satellites and hence influences predominantly the small scale clustering. For high M_{min} (blue) there will be almost no satellites and hence the small scale correlation breaks down. Finally, the bottom panel of Figure 8.2 shows the variation of σ, a parameter that affects the smoothness of the step described by M_{cut}. A high σ (blue) makes the step smoother and includes more low bias, low mass haloes, leading to a lower overall clustering amplitude.

Figure 8.3 repeats the above discussion for the lensing signal $\Delta\Sigma$. We see that its shape is almost robust to the change of the parameters and follows approximately a power law. It is however strongly affected in its amplitude by M_{cut} and σ as we can see in the top right and bottom panel of Figure 8.3. A higher M_{cut} includes more high mass, high bias haloes and thus increases the overall amplitude of the clustering, raising the surface mass density in the peaks. A lower value for the smoothing factor σ emphasises the influence of low bias, low mass haloes and thus decreases the overall clustering amplitude. The top left panel of Figure 8.3 shows that the high satellite number, resulting from a low M_1 can also increase the amplitude of the lensing signal.

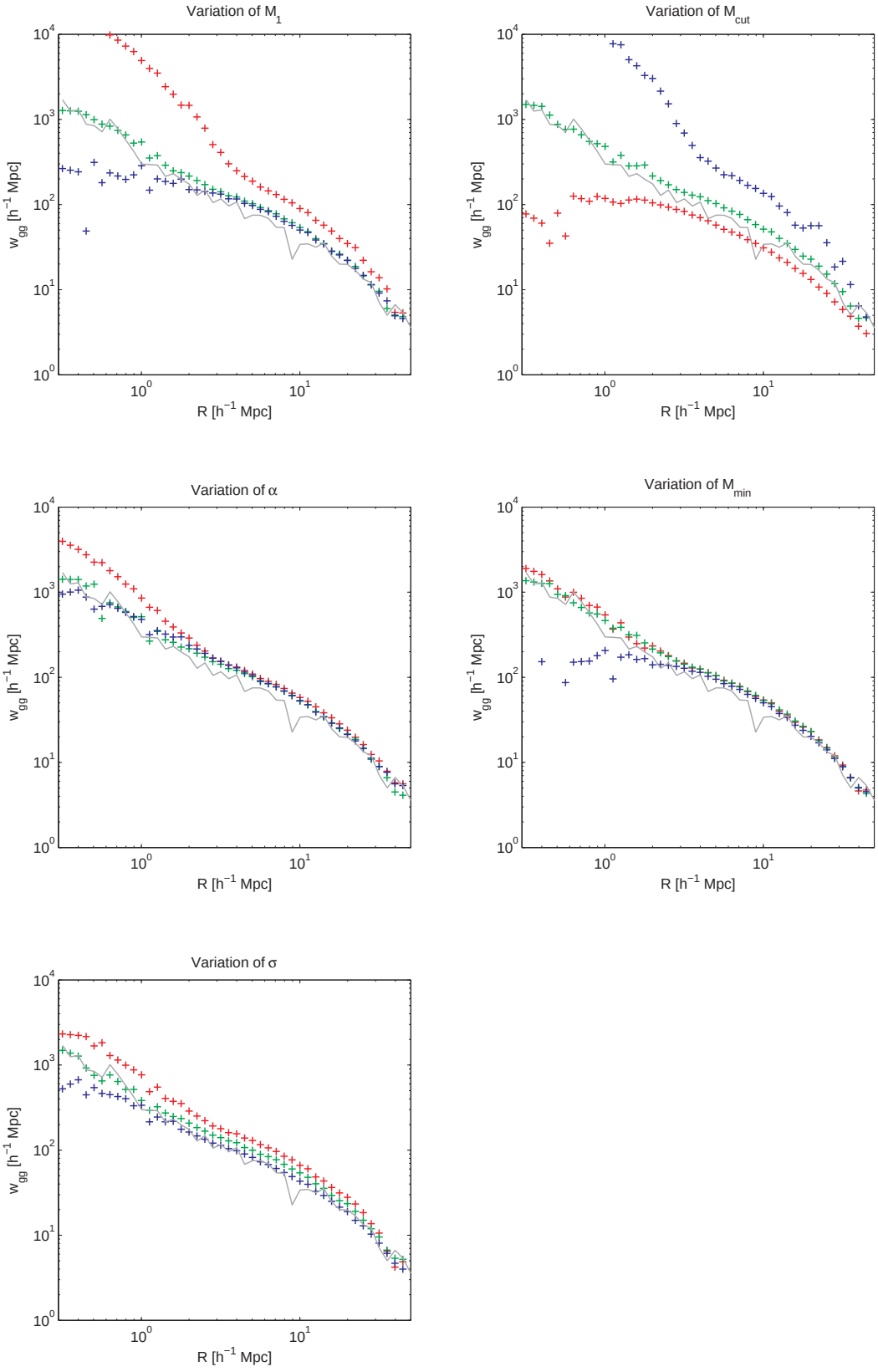

Figure 8.2: Sensitivity of the projected galaxy clustering on variation of single parameters of the five parameter HOD with respect to a fiducial model. Red, green and blue are used for lower, central and larger value of the corresponding parameter. Light gray line shows observed gg correlation for the bright LRG subsample. For interpretation see text.

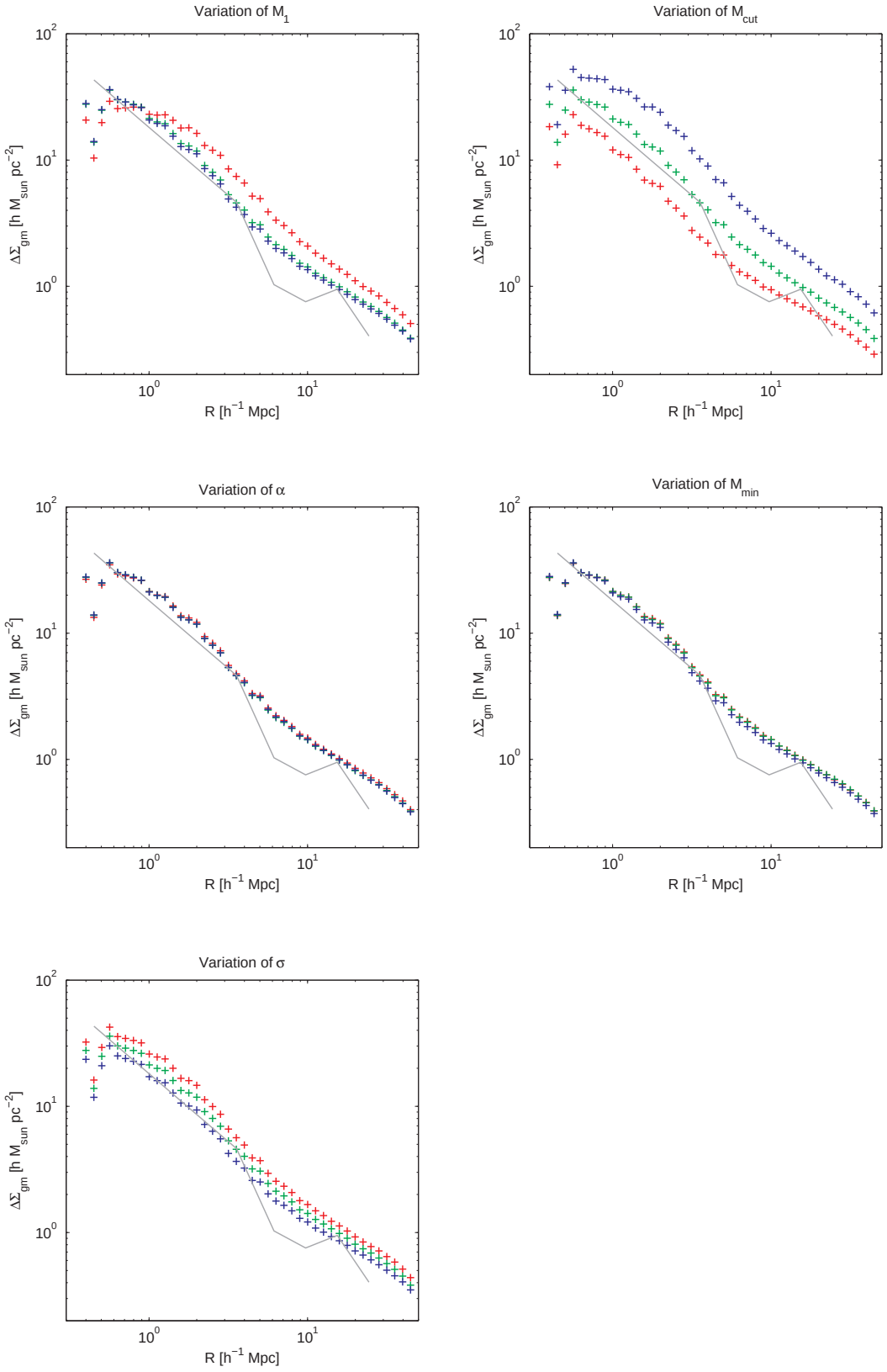

Figure 8.3: Sensitivity of lensing signal $\Delta\Sigma$ on variation of single parameters of the five parameter HOD with respect to a fiducial model. Red, green and blue are used for lower, central and larger value of the corresponding parameter. Light gray line shows measured excess surface mass density for the bright LRG subsample. For interpretation see text.

8.2.2 Best Fit HOD: Bright sample

Before we present the actual best fit results, we mention a few comments concerning the observed data. First we note that there is a pronounced feature in the $\Delta\Sigma$ measurement at scales of $6-9\ h^{-1}$Mpc (see right panel of Figure 8.4). One might argue that this feature could be explained in terms of the halo model, as the transition from the one halo to the two halo term. However we expect this transition to appear on smaller scales. We therefore consider that this feature is likely due to either a measurement error or the errorbars are underestimated. We were not able to reproduce this feature with any of the tested models in that pronounced form. Furthermore, we note that even the clustering data are poorly constrained with fractional errors exceeding 40% at smallest and largest scales and only at the 10% level in between.
Figure 8.4 shows the best fit results for $\Delta\Sigma$ and $w_{\rm gg}$ and the corresponding HOD parameters are quoted in Table 8.2. By eye the prediction seems to be a good fit to the data, but the $\chi^2_{\rm tot} = 4.47$ obtained from the covariance matrix is still rather high, giving $P(\chi^2 > 4.47) \approx 0$ according to (7.69). Interestingly the χ^2 inferred from 615 models changes approximately by a factor of 4 if we use the diagonal errors instead of the full covariance matrix. At the same time the inferred best-fit parameters change remarkably (see the second row of Table 8.2).
In principle the covariance matrix and the mean should be predicted from the theory. Since an external covariance estimator based on the cosmic variance can not account for all the systematic and measurement errors, we instead use the covariance matrix obtained from the measured correlation and lensing. We therefore consider that the large difference in χ^2 is likely to be due to wrong off-diagonal entries. A further issue arises from the noise in the matrix, which might affect the inversion. However, the mathematically correct way is to use the covariance matrix and hence this is the way we choose to obtain our best fit values. For the discussion of bootstrap covariance estimators we refer the reader to §9 and [Norberg *et al.* , 2008].
A closer look at the left panel of Figure 8.4 reveals that the galaxy-galaxy correlation as measured from the simulation gets noisy at the smallest scales corresponding to the one halo regime, which in the halo model is governed by central-satellite or satellite-satellite pairs. This scatter is reasonable from the small satellite fraction of only 4.5%.
We measure the bias under the assumption of scale independence on linear scales $16\ h^{-1}\text{Mpc} \leq r \leq 97\ h^{-1}\text{Mpc}$ that are not yet obscured by the BAO and obtain consistent results of $b = 2.20 \pm 0.03$ and $b = 2.21 \pm 0.02$ from $\xi_{\rm gg}$ and $\xi_{\rm gm}$ respectively.

8.2.3 Best Fit HOD: Faint sample

Again we start with some general observations. The lensing signal for the faint sample in the right panel of Figure 8.5 roughly follows a power law, with a little dip at the largest scales. This sample has a number density of $\bar{n}_{\rm faint} = 8 \times 10^{-5}\ h^3\text{Mpc}^{-3} = 2\bar{n}_{\rm bright}$, leading to much smaller fractional errors for the galaxy-clustering.
In Table 8.2 we show the parameters of the best fit HOD that yield $\chi^2_{\rm tot} = 8.02$. We used 5 free parameters for the fitting procedure and thus considered 3125 points in parameter space. Figure 8.5 shows the clustering and lensing signal of of the best fit model together with the observed spectra. The predicted clustering in the left panel of Figure 8.5 compares rather well with the observed clustering except for the outermost bins. In this context we should mention, that these bins are strongly correlated, i.e. a larger value for one of the bins would increase the others as well. Despite this apparent agreement between theory and observation one should be cautious with the interpretation of log-log plots. The right panel of Figure 8.5 shows that the observed and predicted lensing signal compare very well except for the pre last and the first bin.
We measured the bias for scales $16\ h^{-1}\text{Mpc} \leq r \leq 97\ h^{-1}\text{Mpc}$ and obtain $b = 1.97 \pm 0.03$ and $b = 1.97 \pm 0.02$ from auto- and cross-correlation, respectively. The satellite fraction is 10% and explains the better constrained small scale clustering.
We furthermore note the coincidence of the upper cutoff for $M_{\rm cut,2}$ of the faint sample and the lower cutoff $M_{\rm cut}$ of the bright sample in Table 8.2. This coincidence was obtained from two independent fitting procedures and strengthens the fitting results. On the other hand we

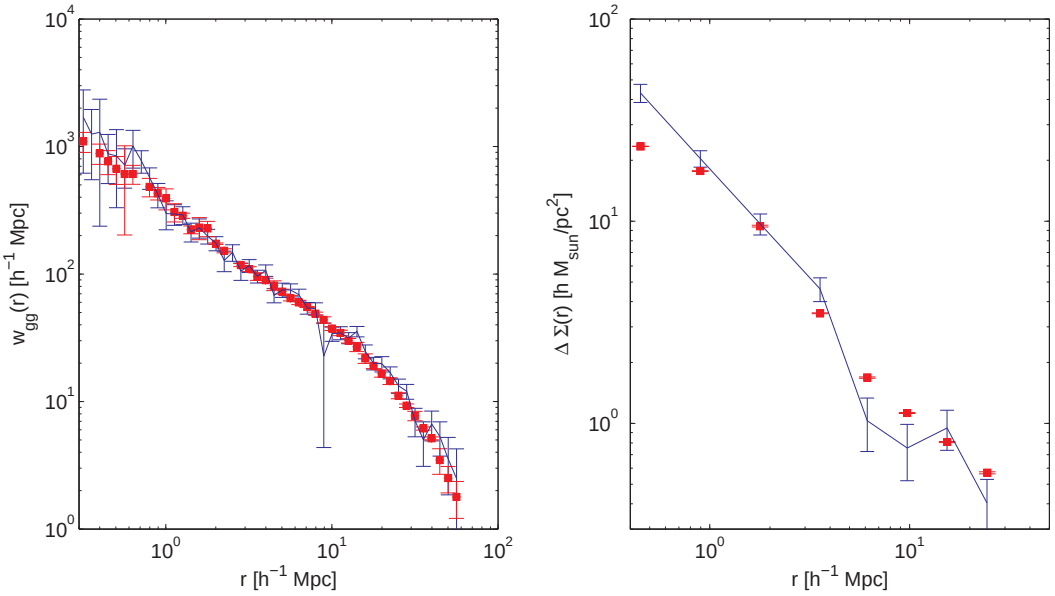

Figure 8.4: *Left panel:* Measured SDSS galaxy autocorrelation for the **bright** LRG subsample from [Mandelbaum *et al.* , 2006a] with diagonal errors (blue). Best fit HOD model for one simulation averaged over four catalogues shown with corresponding standard deviations (red). *Right panel:* Corresponding excess surface mass density measured from galaxy-galaxy lensing (blue line) with diagonal errors. Results from best fit HOD model are shown with standard deviations (red).

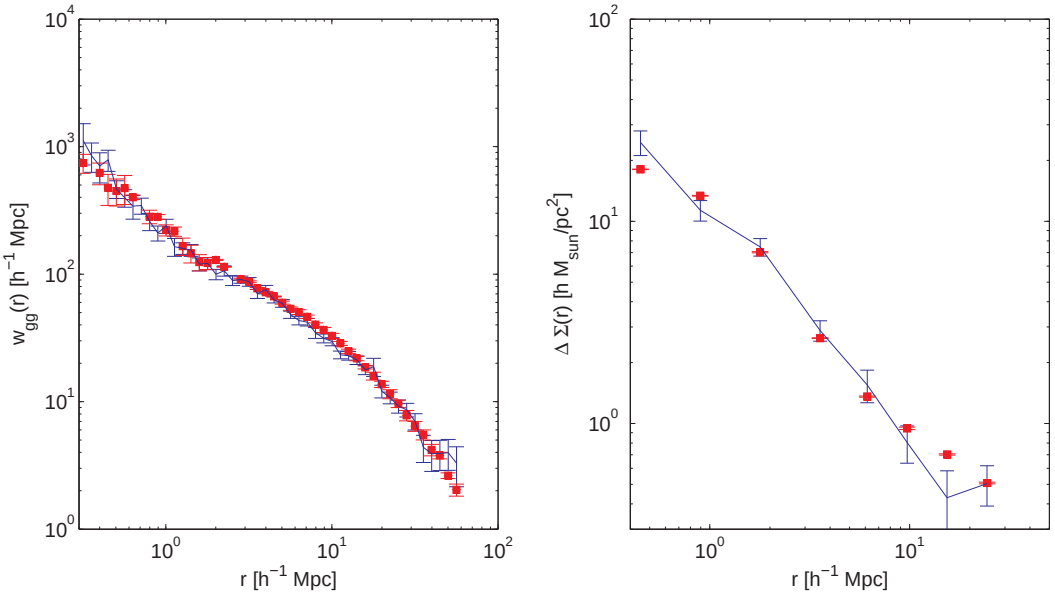

Figure 8.5: *Left panel:* Measured SDSS galaxy autocorrelation for the **faint** LRG subsample from [Mandelbaum *et al.* , 2006a] with diagonal errors (blue). Best fit HOD model for one simulation averaged over four catalogues shown with corresponding standard deviations (red).*Right panel:*Corresponding excess surface mass density measured from galaxy-galaxy lensing (blue line) with diagonal errors. Results from best fit HOD model are shown with standard deviations (red).

have to admit that the $\chi^2 = 8.02$ implies that our model is not a very good description of the data giving $P(\chi^2 > 8.02) \approx 0$ according to (7.69). We hence consider that our modelling of the window is probably not a good description of the luminosity bin sample.
To finish this section, we have to add a remark on the smallest bin of the lensing signal calculated from the simulations in the right panels of Figures 8.4 and 8.5. As we will discuss

below in §8.5, our calculation method artificially truncates the correlation on small scales and hence we miss signal for $\bar{\Sigma}$. This leads to wrong predictions concerning the lensing signal and the first bin should be excluded from the total χ^2. We will however keep the obtained best fit model, since the total χ^2 is dominated by the autocorrelation. Furthermore, the gravitational force softening length of 70 h^{-1} kpc becomes relevant at the scales of the lowest bin and higher resolution simulations are required to probe these scales.

8.3 Cross-Correlation Coefficient

We introduced the cross-correlation coefficient of of the correlation function for two tracer populations A and B as

$$r_{\mathrm{cc}} = \frac{\xi_{\mathrm{AB}}}{\sqrt{\xi_{\mathrm{AA}}\xi_{\mathrm{BB}}}}. \tag{8.1}$$

In this section we will start to look at the cross-correlation coefficient of the haloes as fundamental building blocks of the large scale structure. Afterwards we will turn towards the cross-correlation coefficient of the galaxies and the matter and examine how the cross-correlation is affected by the additional small scale clustering. Finally we will consider the cross-correlation coefficient of the excess surface mass density, since this is the quantity available from observations.

8.3.1 Haloes

As shown in the top panel of Figure 8.6 the cross-correlation coefficient calculated from $\xi(r)$ drops below unity at about 10 h^{-1}Mpc for haloes due to stochasticity that is introduced by the nonlinear gravitational clustering. Interestingly this behaviour is independent of the halo mass down to the cluster radius. It can be modeled using perturbation theory as

$$r_{\mathrm{cc}}(r) \approx 1 - b_2^2 \frac{\xi_{\mathrm{lin}}(r)}{4}, \tag{8.2}$$

where b_2 is the second order bias [McDonald, 2006]. The second order bias is a free parameter and we chose it in order to reproduce the shape of the cross-correlation. In the top panel of Figure 8.6 we see that the decrease of r_{cc} towards small scales is well reproduced by perturbation theory.

We already noted that cross-correlation coefficient of the galaxies and the matter can be used to infer to the correlation function or power spectrum of the underlying dark matter density field. It is a key issue in cosmology to reconstruct this quantity since it contains a wealth of information that can be used to determine neutrino mass or cosmological parameters.

It is however not possible to measure ξ_{gm} directly. The best thing we can do is to measure its projection along the line of sight by galaxy-galaxy lensing. Projections are easier to obtain also for the clustering, since projection helps to remedy redshift space distortions without assumptions about the nonlinear clustering. This leads us to look at the cross-correlation coefficients calculated from projected statistics and we show the corresponding results for the haloes in Figure 8.6. Interestingly the cross-correlation coefficient first decreases with decreasing radius to turn up at the cluster radius as a consequence of the halo exclusion.

8.3.2 Galaxies: Projected Correlation

We will now turn to towards the galaxies. The following discussion will be based on the LRG catalogues of the best fit models described above. If the cross-correlation coefficient was unity down to the nonlinear scales (for example given by a typical halo radius R_0) we could reconstruct the matter correlation from measurable quantities such as $w_{\mathrm{gg}}(R)$ and $\Delta\Sigma(R)$. To examine these effects we use our galaxy catalogues as described in §8.2. In a first step we

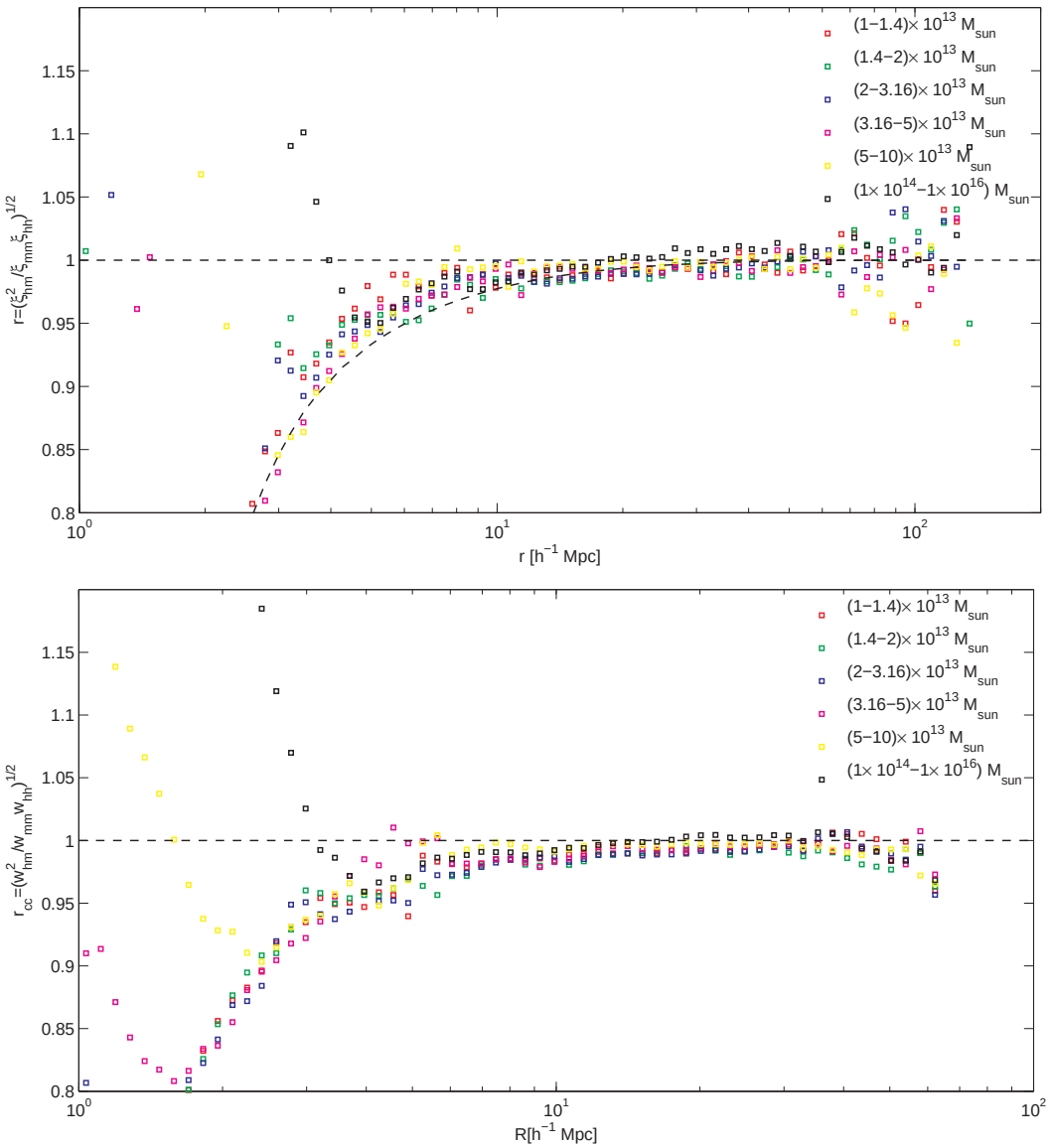

Figure 8.6: *Top panel:* Cross-correlation coefficient between haloes and matter calculated from $\xi(r)$ for six different halo mass bins. Remarkably r is close to one on intermediate scales but drops below unity around 10 h^{-1}Mpc. Furthermore the signal becomes noisy on scales around the baryon acoustic oscillations. Data are obtained from averaging over eight simulations and using a 1024 cell FFT. For comparison we overplot the perturbation theory prediction (8.2) for $b_2 = 0.52$, chosen to fit the shape of the cross-correlation function.*Bottom panel:* Cross correlation coefficient between haloes and matter calculated from $w(R)$ for six equal signal-to-noise halo mass bins. Data are obtained from averaging over eight simulations and using a 1024 cell FFT for redshift $z = 0$.

consider the projected correlation function w to calculate

$$r^{(w)}(R) = \frac{w_{\rm gm}(R)}{\sqrt{w_{\rm gg}(R) w_{\rm mm}(R)}}. \tag{8.3}$$

Results are shown in Figure 8.7 for the bright subsample and in Figure 8.8 for the faint subsample. For these figures we perform a line of sight integration of the non-linear $\xi(r)$, averaged over eight simulation volumes. Both plots show that $r_{\rm cc}^{(w)}$ calculated from the projected correlation is close to unity down to 5 h^{-1}Mpc. There are however differences between the full sample (solid lines) and the sample, where all the satellite LRGs are removed (dashed line). These differences are more pronounced for the faint sample, which is understandable from the fact

that the faint sample has a satellite fraction twice as high as the bright sample. It is interesting to compare Figure 8.7 with Figure 8.6. For the central sample we see a minimum and an upturn in r as we go to smaller and smaller scales that is also present in the highest mass halo bin. This behaviour can be explained from the fact that the central LRGs trace the dark matter haloes above a certain mass threshold and for the central LRGs the halo exclusion applies as well. Inclusion of the satellites makes the dip less pronounced and the slope a bit shallower because the central-satellite and satellite-satellite pairs increase the clustering on scales below the virial radius.
But since w_{gm} is not observable we have to switch to quantities that are in fact observable. Hence we consider $\Delta\Sigma(R)$ as defined in (6.23)[1]

$$\Delta\Sigma(R) = \bar{\Sigma}(R) - \Sigma(R) \tag{8.4}$$

and calculate the cross correlation coefficient of $\Delta\Sigma_{\mathrm{gm}}, \Delta\Sigma_{\mathrm{gg}}$ and $\Delta\Sigma_{\mathrm{mm}}$. The bottom panels of Figure 8.9 and Figure 8.10 show the result as a black solid line - it is different from unity and strongly scale dependent for both samples. That was to be expected, since $\Delta\Sigma$ contains information from the non-linear scales dominated by the halo profile rather than linear correlation functions. In principle one should be able to subtract these non-linear contributions to $\Delta\Sigma$ out.

8.3.3 Galaxies: Compensated Surface Mass Density

We remove the excess surface mass density within radius R_0, whose value we will choose in order to move the resulting cross-correlation as close to unity as possible

$$\Gamma(R) := \Delta\Sigma(R) - \frac{R_0^2}{R^2}\Delta\Sigma(R_0), \tag{8.5}$$

$$= \frac{2}{R^2}\int_{R_0}^{R} w(r')r'dr' - w(R) + w(R_0)\frac{R_0^2}{R^2}. \tag{8.6}$$

We see that $\Gamma(R)$ depends only on correlations on scales larger than the cutoff radius R_0 and that its calculation can be easily performed once the lensing has been measured. For sure the resulting quantity can only be used on scales larger than the cutoff scale. We will now calculate the cross-correlation coefficient from this compensated lensing signal

$$r^{(\Gamma)}(R) = \frac{\Gamma_{\mathrm{gm}}(R)}{\sqrt{\Gamma_{\mathrm{gg}}(R)\Gamma_{\mathrm{mm}}(R)}}. \tag{8.7}$$

In the bottom panel of Figure 8.9 we show the cross-correlation coefficient of Γ for the bright sample with different cutoff radii. We calculated the quantities shown in this plot by numerical integration of the non-linear correlation functions measured in the simulations. The corresponding cross-correlation for the faint sample is plotted in the bottom panel of Figure 8.10. We can conclude that the subtraction of central contributions as described above is an effective way to recast cross-correlation coefficient back to unity. Due to the smaller cluster radii of the faint sample, $R_0 = 3\ h^{-1}$Mpc is already an overcompensation, whereas for the bright sample it gives the best result. As these figures were calculated using the non-linear correlation function averaged over eight simulations, we show the corresponding plots for the excess surface mass density measured directly in the simulations in Figure 8.11.
In real data the quantity $\Delta\Sigma(R_0)$ is not known, just bin averaged lensing signals can be measured. Thus we explore, how the scatter in the bin with centre at R_0 affects the resulting cross-correlation coefficient. We show $\Delta\Sigma$ corrected by the lensing signal in the bin around R_0 as the blue crosses in the top left panel of Figure 8.11 and note that the standard deviation

[1] Note that in the following we will use Σ as a symbol to denote the projected surface number density and omit multiplication with the mass density as this factor is irrelevant for the cross-correlation factor. Furthermore we calculate Σ for all three correlations (mm, gm, gg) and not only for gm as in the usual definition from lensing.

over the eight simulations is not negligible. So we investigate whether the result improves if we use a spline fit to the lensing signal over the range 1.5 h^{-1}Mpc $\leq R \leq$ 3.5 h^{-1}Mpc for the determination of $\Delta\Sigma(R_0)$. We show the resulting corrected lensing signal as red crosses with errorbars in the top left panel of Figure 8.11. Both the scatter and the mean are in accordance with the bin subtraction. The bottom left panel of Figure 8.11 repeats above investigation for the faint sample. In this plot the scatter is lower due to the higher number density and the value of R_0 is chosen smaller to account for the smaller cluster radii.
We saw both from non-linear theory and the simulation measurement that the compensation method can effectively restore a cross-correlation coefficient close to unity. Now we have to test, how well the matter autocorrelation can then be obtained under the assumption $r \equiv 1$

$$\Gamma_{\rm mm}(R) = \frac{\Gamma^2_{\rm gm}(R)}{\Gamma_{\rm gg}(R)}, \qquad R > R_{\rm min}, \tag{8.8}$$

here $R_{\rm min}$ is the radius at which cross-correlation coefficient starts to deviate from unity. Unfortunately we have no theoretical prediction for $R_{\rm min}$ and have to settle for using a value of $R_{\rm min} \approx 5$ h^{-1}Mpc inspired by our numerical studies.
Similarly to our argumentation in §7.5 one could in principle invert $\Gamma_{\rm mm}$ to obtain the projected matter autocorrelation

$$w(R) = \int_{R_0}^{R} w'(\tilde{R}) d\tilde{R} + w(R_0) \tag{8.9}$$

$$= -\int_{R_0}^{R} \left\{ \frac{2}{\tilde{R}} \Gamma(\tilde{R}) + \Gamma'(\tilde{R}) \right\} d\tilde{R} + w(R_0). \tag{8.10}$$

But since the measured lensing signals are already noisy, an integral over the function and its derivative will be even more noisy. Calculating $\Gamma(R)$ from the linear power spectrum and comparing it to the results obtained from the measurement should perform better. This procedure should in fact enable estimates of slope and amplitude of the primordial power spectrum.
In the top right panel of Figure 8.11 we show a reconstructed matter correlation $\Gamma_{\rm mm}$ together with linear and non-linear theory prediction for the bright sample. There is reasonable agreement between reconstructed and theoretical surface mass density. But there are differences between the non-linear and linear $\Gamma_{\rm mm}$ if R_0 is chosen too small. For the bright sample the large virial radii imply a rather large R_0 to restore cross-correlation coefficient of unity. As a consequence the linear and non-linear correlation functions at R_0 are very close and the linear prediction for $\Gamma_{\rm mm}$ gives a reasonable fit to the measured quantity. In contrast, for the faint sample shown in the bottom right panel of figure 8.11 we have to choose R_0 somewhat smaller, since too large R_0 will lead to a too strong correction on $\Delta\Sigma$ and consequently to a cross-correlation coefficient below unity. One can maybe correct for that, using perturbation theory descriptions of cross correlation coefficient.

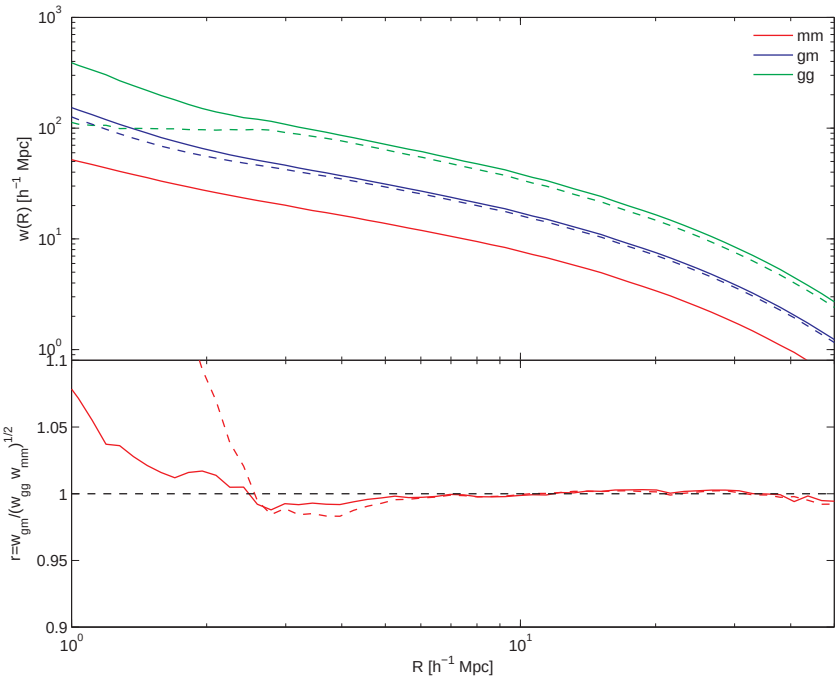

Figure 8.7: *Top panel:* Projected autocorrelations for matter, **bright** galaxies and corresponding cross-correlation calculated from measured non-linear $\xi(r)$. Dashed lines correspond to a sample where all the satellites are removed from the catalogue and only the LRG host halo centres contribute to the signal. *Bottom panel:* Cross-correlation coefficient of the spectra in the top panel.

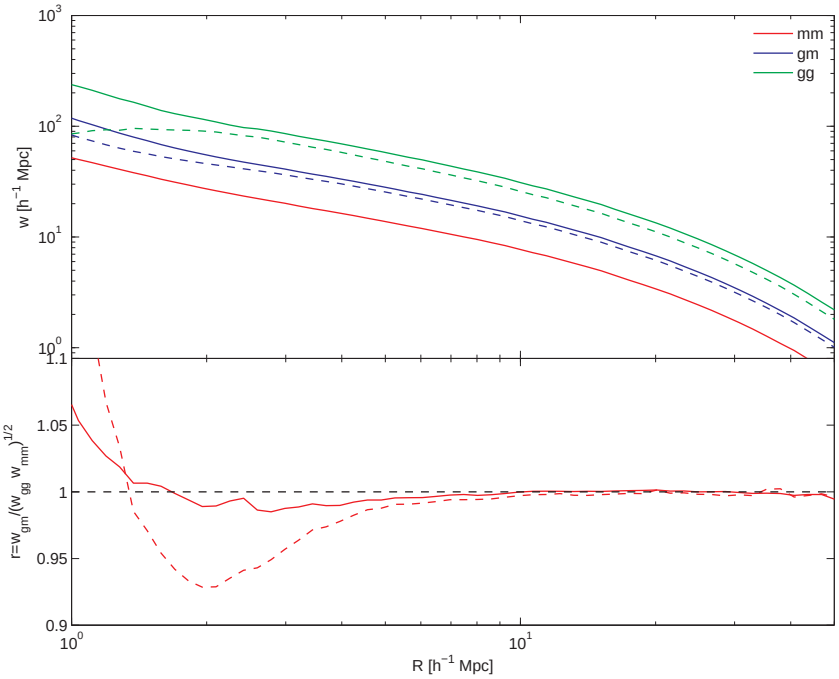

Figure 8.8: *Top panel:* Projected autocorrelations for matter, **faint** galaxies and corresponding cross-correlation calculated from measured non-linear $\xi(r)$. Dashed lines correspond to a sample where all the satellites are removed from the catalogue and only the LRG host halo centres contribute to the signal. *Bottom panel:* Cross-correlation coefficient of the spectra in the top panel.

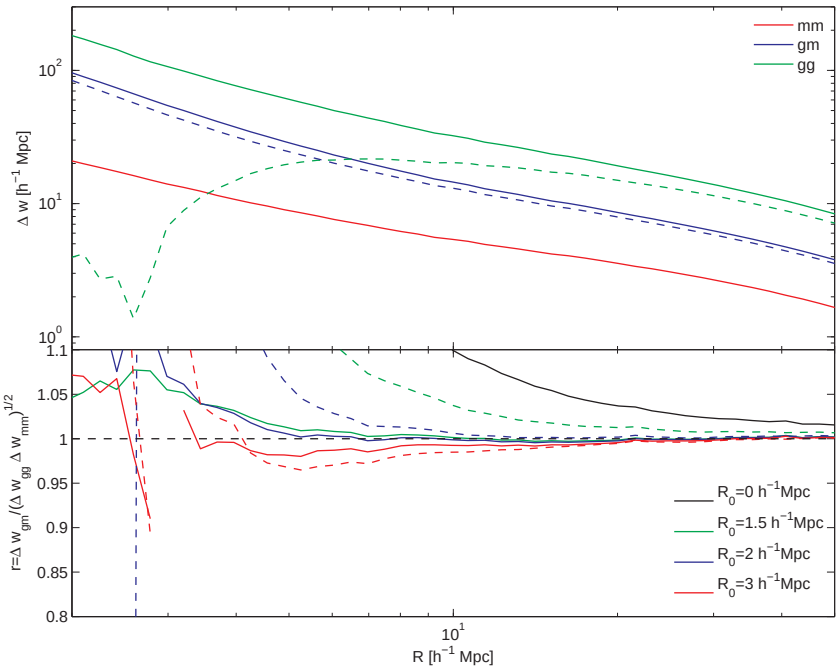

Figure 8.9: *Top panel:* Excess surface density for **bright** sample as calculated from non-linear $\xi(r)$. *Bottom panel:* Cross-correlation coefficient calculated from excess surface mass density. Black is trivial $r = \Delta\Sigma_{gm}/\sqrt{\Delta\Sigma_{gg}\Delta\Sigma_{mm}}$ and is obviously far away from unity. Blue, green and red line are calculated from $\Gamma(R) = \Delta\Sigma(R) - \Delta\Sigma(R_0)R_0^2/R^2$ where $R_0 = 1.5, 2, 3\ h^{-1}$Mpc. Dashed lines correspond to a sample where all the satellites are removed from the catalogue and only the LRG host halo centres contribute to the signal.

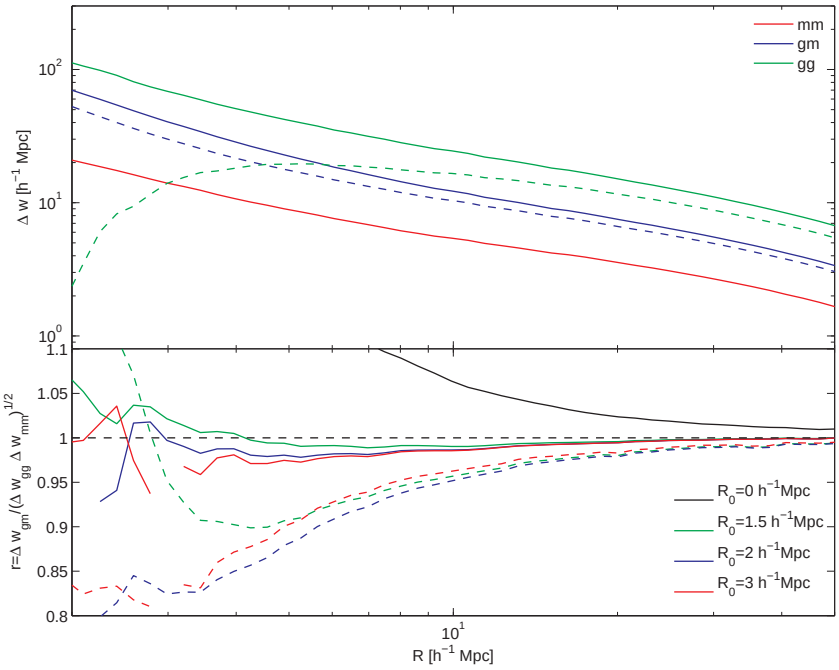

Figure 8.10: *Top panel:* Excess surface density for **faint** sample as calculated from non-linear $\xi(r)$. *Bottom panel:* Cross-correlation coefficient calculated from excess surface mass density. Black is trivial $r = \Delta\Sigma_{gm}/\sqrt{\Delta\Sigma_{gg}\Delta\Sigma_{mm}}$ and is obviously far away from unity. Blue, green and red line are calculated from $\Gamma(R) = \Delta\Sigma(R) - \Delta\Sigma(R_0)R_0^2/R^2$ where $R_0 = 1.5, 2, 3\ h^{-1}$Mpc. Dashed lines correspond to a sample where all the satellites are removed from the catalogue and only the LRG host halo centres contribute to the signal.

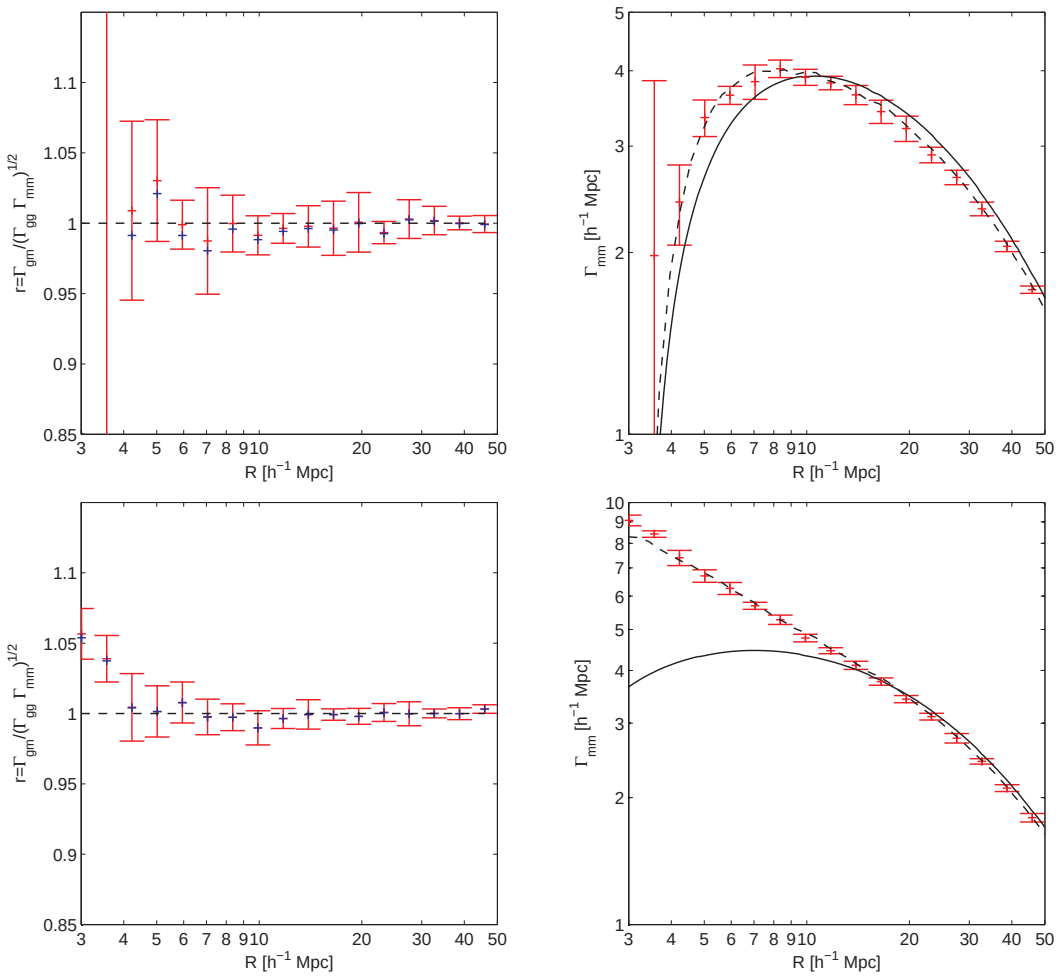

Figure 8.11: *Top left panel:* Cross-correlation coefficient for the **bright** sample calculated from the lensing signal measured in the simulations. For the red points with errorbars we fitted $\Delta\Sigma$ in the range 1.5 h^{-1}Mpc $\leq R \leq$ 3.5 h^{-1}Mpc by a power law and used the resulting function for subtraction of $\Delta\Sigma(R_0 = 3.3\ h^{-1}\text{Mpc})$. Errorbars show standard deviation over 8 simulations. For the blue points we took $\Delta\Sigma$ of the bin containing R_0 for the subtraction. *Top right panel:* Reconstructed non-linear matter surface mass density $\Gamma_{\rm mm}$ (red with errors estimated from the standard deviation between eight simulations). Solid black line shows linear theory $\Gamma_{\rm mm}^{\rm (lin)}$ and dashed black line shows $\Gamma_{\rm mm}^{\rm (nl)}$ calculated from the measured non-linear correlation. *Bottom left panel:* Cross-correlation coefficient for the **faint** sample calculated from the measured projection. For red points with errorbars we fitted $\Delta\Sigma$ in the range 1.5 h^{-1}Mpc $\leq R \leq$ 3.5 h^{-1}Mpc by a power law and used the resulting function for subtraction of $\Delta\Sigma(R_0 = 1.6\ h^{-1}\text{Mpc})$. Errorbars show standard deviation over 8 simulations. For the blue points we took $\Delta\Sigma$ of the bin containing R_0 for the subtraction. *Bottom right panel:* Reconstructed non-linear matter surface mass density $\Gamma_{\rm mm}$ (red with errors estimated from the standard deviation between eight simulations). Solid black line shows linear theory $\Gamma_{\rm mm}^{\rm (lin)}$ and dashed black line shows $\Gamma_{\rm mm}^{\rm (nl)}$ calculated from the measured non-linear correlation.

8.4 Redshift Space Distortions on Projected Correlation Functions

The common assumption is that one can remedy redshift space distortions by integrating along the line of sight. However, there is no consensus on how far one has to integrate to reduce the distortions to a desired level. We address this question both with Kaiser's analytic expression for the power spectrum and with simulation results. In Figure 8.13 we show the ratio of the redshift space to real space galaxy autocorrelation functions, where the theoretical prediction was calculated using Equation (7.108). It is evident from this plot that, even for integration of $\chi_{\rm max} = 100\ h^{-1}$Mpc on each side, there are deviations on the 10% level. Furthermore we see that on these large scales the Kaiser based linear theory prediction is a good description of the data. The excess of the signal in redshift space compared to real space can maybe explain the differences between our HOD and the observed clustering in the outermost bins of Figure 8.4 and Figure 8.5. Unfortunately we did this study only after we finished the fitting so that we could not correct for this effect. From that we can conclude that the fitting should be better done in redshift space.

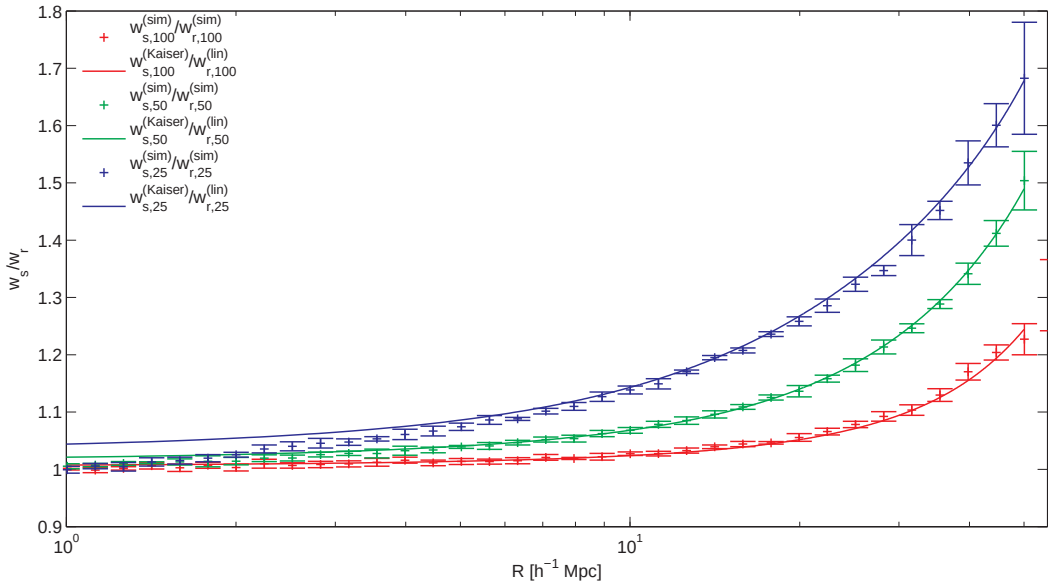

Figure 8.12: Ratio of the redshift space to real space projected galaxy-galaxy correlation function for integration lengths $\chi_{\rm max} = 25, 50, 100\ h^{-1}$Mpc in blue, red and green respectively. The solid lines show the linear theory prediction based on Kaiser formula, whereas the points with errorbars are measured. Kaiser can reproduce the observed ratios very well on scales $R \geq 10\ h^{-1}$Mpc. We see that even for 100 h^{-1}Mpc integration there are deviations on the 10% level. The results shown here are for the bright LRG sample an correspond to $b = 2.2$.

If we want to use the cross-correlation coefficient calculated from lensing and clustering measurements, we are merging two different quantities in terms of integration length. The window for the lensing is not a top hat in radial distance, but a skew window that essentially stretches from the lens to the source plane. We will however make the practical assumption of $\chi_{\rm max,gm} = 500\ h^{-1}$Mpc, which ensures that redshift space distortions are not important for lensing results. In contrast the window for the clustering measurements is relatively shallow and is taken to be $\chi_{\rm max} \approx 50\ h^{-1}$Mpc for most surveys. Consequently a correction of either $w_{\rm gm}$ or $w_{\rm gg}$ should be applied. To do so we have to consider the ratio

$$\gamma = \frac{w_{\rm gg,s}(R, \chi_{\rm max} = 500\ h^{-1}{\rm Mpc})}{w_{\rm gg,s}(R, \chi_{\rm max} = 50\ h^{-1}{\rm Mpc})} \approx \frac{w_{\rm gg,r}(R, \chi_{\rm max} = 500\ h^{-1}{\rm Mpc})}{w_{\rm gg,s}(R, \chi_{\rm max} = 50\ h^{-1}{\rm Mpc})}, \tag{8.11}$$

which can then be used to calculate a $w_{\rm gg,s}(R, \chi_{\rm max} = 500\ h^{-1}{\rm Mpc}) = \gamma w_{\rm gg,s}(R, \chi_{\rm max} = 50\ h^{-1}{\rm Mpc})$ corresponding to $w_{\rm gm}$ as measured from the lensing. We already saw that the

Kaiser based linear theory prediction provides a good description of the projected galaxy clustering on large scales. Hence we evaluate above fraction using linear theory and Kaiser prediction and show the results in Figure 8.13. For our results on cross-correlation coefficient we use projections over 50 h^{-1}Mpc both for galaxy-matter and galaxy-galaxy correlation. Integrating the galaxy-matter cross correlation over 500 h^{-1}Mpc on each side would slow down our calculations tremendously and affect the inferred $\Delta\Sigma$ only on the 1% level in the outermost bin.

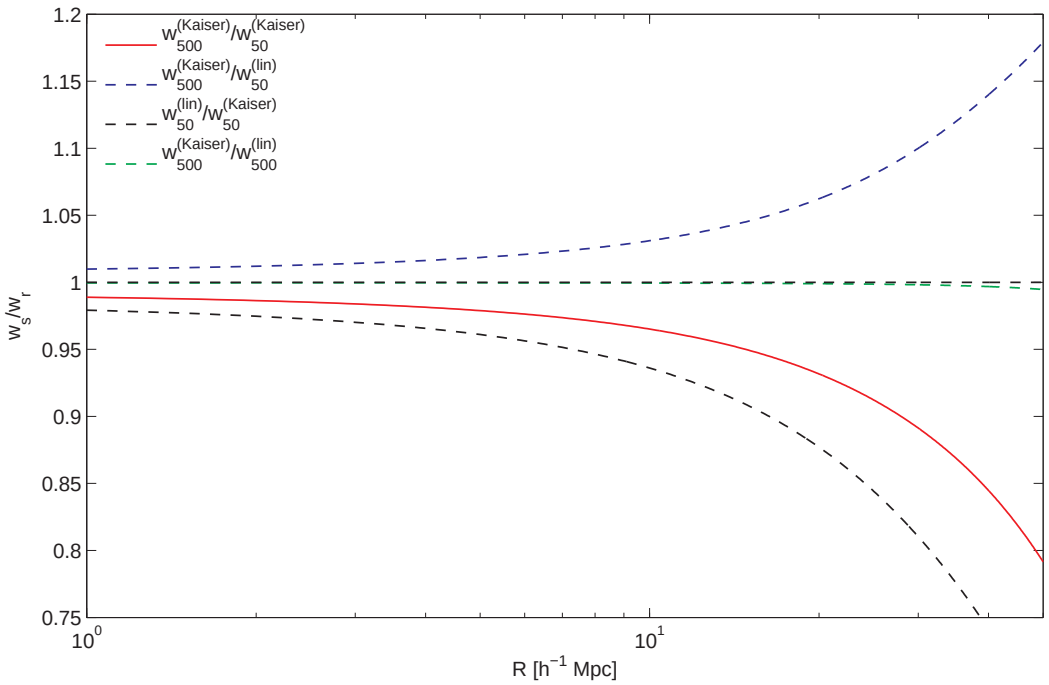

Figure 8.13: Ratio of the redshift space galaxy correlation functions projected over $\chi_{max} = 500\ h^{-1}$Mpc and $\chi_{max} = 50\ h^{-1}$Mpc (red solid). This ratio can be broken up in the difference between real and redshift space (lower black dashed) and the difference due to the integration length (blue dashed). We also show that the projection over 500 h^{-1}Mpc remedies the redshift space distortions completely (green dashed line). The red line thus shows the correction one should apply to the clustering measurements with a narrow window, if one wants to compare them to lensing measurements with a much wider window. The results are based on Kaiser formula for the bright LRG sample and correspond to $b = 2.2$.

8.5 Small Scale Truncation

As already noted the excess surface mass density $\Delta\Sigma$ combines information from very small scales and from larger scales. We know however, that our small scale resolution is limited both by the finite resolution of the simulation and by the resolution of the FFT method used to calculate Σ. Therefore we investigate how the shape of the correlation on small scales (which we are resolving) affects our result on larger scales. To do so we will make the simplifying assumption that $\xi(r)$ and consequently $w(R)$ can be well approximated by power laws. The truncation of such a power law in the form

$$w(R) = \begin{cases} \left(\frac{R}{R_0}\right)^{\alpha}, & \text{for } R > b \\ 0, & \text{otherwise} \end{cases} \tag{8.12}$$

leads to the following result for $\Delta\Sigma$

$$\Delta\Sigma(R) = -\frac{\alpha}{\alpha+2}\left(\frac{R}{R_0}\right)^{\alpha} - \frac{2}{\alpha+2}\left(\frac{b}{R_0}\right)^{\alpha}\left(\frac{b}{R}\right)^{2}. \tag{8.13}$$

The last term on the rhs is a correction to the pure power law behaviour, which is given by the first term. We see that for $\alpha > -2$ there is a supression of the form $-1/R^2$ which will vanish for $R \gg b$. The same argument should apply for more realistic correlation functions. The halo profiles in N-body simulations are remarkably well described by the NFW profile, which is a broken power law with slope -1 in the central regions and -3 further out. For scales below the cluster radius of a halo of given mass M the correlation is given by the density profile. The total correlation function is a superposition of these profiles appropriately weighted by the HOD or mass function.

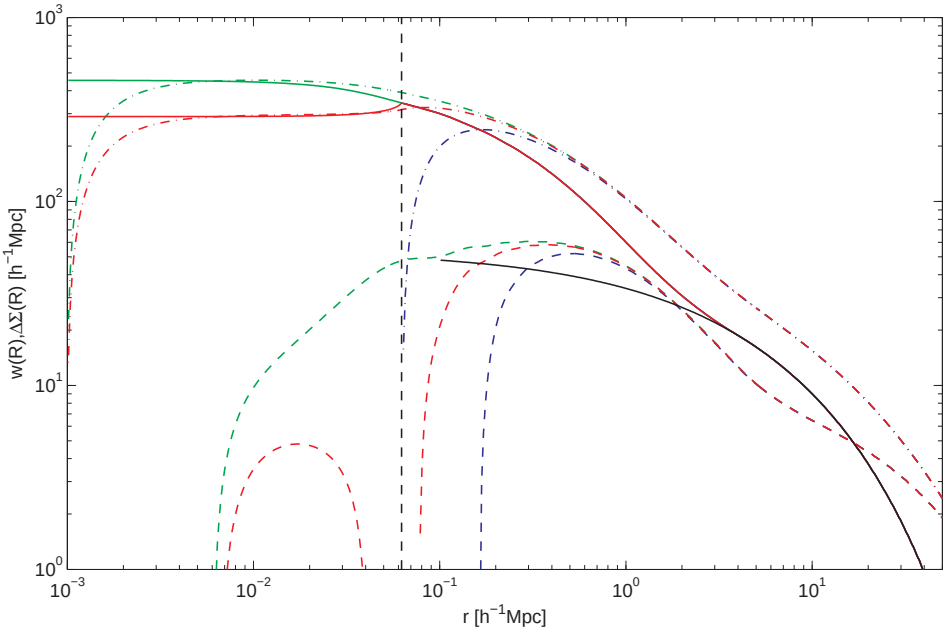

Figure 8.14: Effect of the truncation of correlation function on small scales. We start from a nonlinear correlation function $\xi_{\mathrm{HALOFIT}}(r)$ calculated with `HALOFIT` based on a `CMBFAST` transfer function. The green solid line shows the projected correlation as calculated from $\xi_{\mathrm{HALOFIT}}(r)$. Then we investigate how a truncation of $\xi(r)$ as in Equation (8.14) (red) or $\Sigma(R)$ as in Equation (8.15) (blue) at the radius marked by the vertical dashed line affects $\Delta\Sigma$. The dot-dashed lines show the corresponding $\bar{\Sigma}$ and the dashed lines show $\Delta\Sigma$. The black solid line is the linear $\Sigma(R)$.

In Figure 8.14 we show the results for a numerical study based on a `HALOFIT` [Smith *et al.* , 2003] power spectrum and a cutoff radius $b = 0.07\ h^{-1}$Mpc inspired by the softening length of our simulations. We show the quantities $\Sigma, \bar{\Sigma}$ and $\Delta\Sigma$ calculated by numerical integration of the full non-linear correlation function $\xi_{\mathrm{HALOFIT}}(r)$ as solid, dash-dotted and dashed green lines. Then we modify $\xi(r)$ as

$$\tilde{\xi}(r) = \begin{cases} \xi_{\mathrm{HALOFIT}}(r), & r > b \\ 0, & r < b \end{cases} \tag{8.14}$$

and then calculate $w(R)$ by numerical integration of $\tilde{\xi}(R)$. This results in the solid, dash-dotted and dashed red lines in Figure 8.14 for $\Sigma, \bar{\Sigma}$ and $\Delta\Sigma$, respectively. This would be case if we measured the correlation function from the simulation and then trivially integrated it. For the calculations presented in the the other sections of this thesis we fit a natural spline to the correlation function before integrating it along the line of sight and thus artificially continue the correlation to smaller scales. The missing small scale correlation has no effect on Σ above b, but leads to a decrease in $\bar{\Sigma}$ up to 0.2 h^{-1}Mpc and affects $\Delta\Sigma$ up to 0.5 h^{-1}Mpc. Finally we should consider the case of a truncated Σ

$$\tilde{\Sigma}(R) = \begin{cases} \int_{-\chi_{\mathrm{max}}}^{\chi_{\mathrm{max}}} \xi_{\mathrm{HALOFIT}}(R,\chi) d\chi, & R > b \\ 0, & R < b \end{cases} \tag{8.15}$$

The blue solid, dash-dotted and dashed lines in Figure 8.14 show the result - we see that the truncation of Σ at the scale $b \approx 0.07\ h^{-1}$Mpc results in a too small $\Delta\Sigma$ that converges to the true value only at $R \approx 0.7\ h^{-1}$Mpc. The missing amplitude roughly follows the $-1/R^2$-behaviour predicted in Equation (8.13). The latter case is be the most relevant for the measurement of the lensing signal from the simulation as there is a lack of pairs closer than the softening length. Even the direct summation code, which should resolve all pairs down to zero separation, produces a $\Delta\Sigma$ that peaks at $R \approx 0.8\ h^{-1}$Mpc and decreases on smaller scales.

8.6 Influence of Satellite Galaxies

As already noted by [Zheng *et al.* , 2008] there is clear evidence that a fraction of the LRGs has to be satellites. The small scale clustering amplitude requires pairs closer than the virial radii of the haloes. As we show in figure 8.15 for the bright sample the galaxy-galaxy clustering and galaxy-matter correlation show only minor changes on scales above 3 h^{-1}Mpc if we exclude the satellite galaxies. On smaller scales however, the galaxy-galaxy autocorrelation for the centrals starts to decay below the correlation of the complete sample. This behaviour is clear from the halo model, since the galaxies live in haloes of mass exceeding $M \gtrsim 5 \times 10^{14}\ h^{-1}M_\odot$ corresponding to cluster radii of $r_{200} \gtrsim 1\ h^{-1}$Mpc.[2] By definition such haloes should not overlap and so all the clustering of galaxies on scales smaller than two virial radii must be due to central-satellite or satellite-satellite pairs. The nonzero value for the small scale clustering of the centrals comes from galaxies residing in small mass haloes $M \gtrsim 1.2 \times 10^{13}\ h^{-1}$Mpc in the tail of the smoothed step (7.77), which have radii $r_{200} \gtrsim 0.8\ h^{-1}$Mpc.

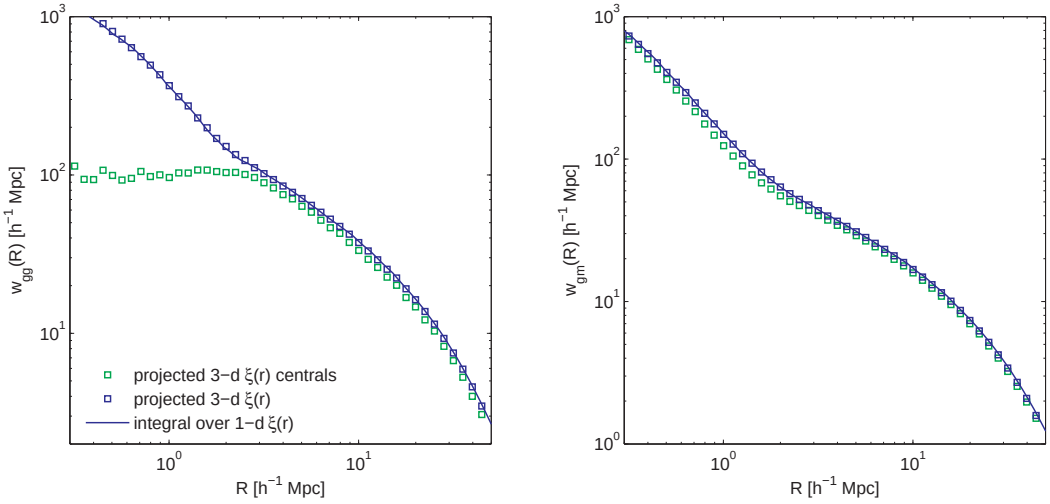

Figure 8.15: *Left panel:* Galaxy autocorrelation function for the bright sample (blue) and the host halo centres of this sample (green). The solid line is obtained from integrating a spline fitted $\xi(r)$, whereas points are obtained directly from the projected 3-d correlation $\xi(\boldsymbol{r})$. *Left panel:* Galaxy-matter cross-correlation for the same sample.

8.7 NFW Versus Dark Matter

As mentioned before our standard approach for the distribution of the galaxies in their host halo is to sample from the dark matter particle distribution. However, this is a computationally expensive task since both the dark matter particle positions and their velocities have to be kept in memory. Therefore we explore a distribution according to the NFW profile

[2] The subscript 200 refers to a halo that has a mean density of 200 times the background density.

[Navarro *et al.* , 1996] with concentration parameter

$$c = 9 \left[\frac{M}{M_*} \right]^{-0.13} . \tag{8.16}$$

As we show in Figure 8.7 the correlation functions obtained for the two approaches differ only on the percent level for intermediate scales. The small scale behaviour however depends strongly on the way in which the galaxies are distributed within their host halo. Differences become also significant at the BAO scale, since this feature depends on the non-linear clustering. We

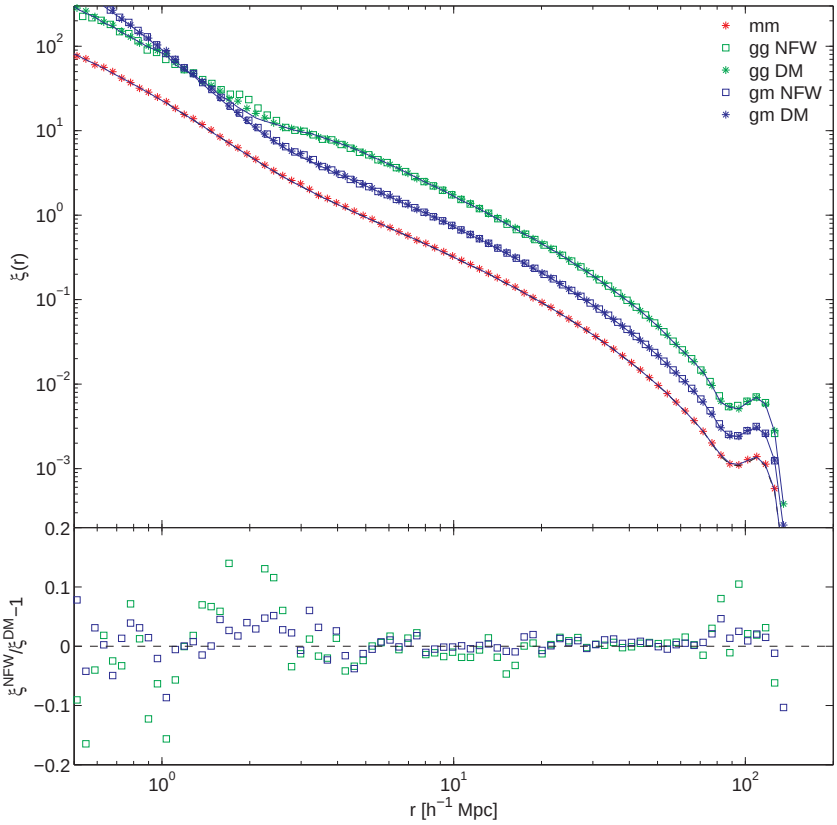

Figure 8.16: *Top panel:* Comparison of the galaxy-galaxy autocorrelation (green) and galaxy-matter cross-correlation (blue) for galaxies following the dark matter distribution (squares) and distributed according to a NFW profile around the halo centre (stars). The results are an average over eight simulation volumes and one galaxy catalogue per simulation. The red stars show matter autocorrelation and the solid lines show the correlation as calculated with the tree code. *Bottom panel:* Relative difference between the galaxy distributions for gg auto-correlation (green) and gm cross-correlation (blue). Note that the two point function is quite similar for the two profiles except for the nonlinear scales where the one halo term dominates.

however caution the reader about an overinterpretation of this preliminary results. Firstly a better modelling of the concentration parameter (8.16) or inclusion of halo triaxiality could maybe improve the accordance on small scales. Secondly the results, we show in Figure 8.7 are averaged over eight simulations but consider only one galaxy catalogue per simulation. So the differences can maybe be explained by the scatter of the HOD. Since we so far could not show the equivalence of the two distribution schemes, we stick to the distribution following the dark matter particles for the time being.

8.8 Projected Correlation Functions

We use two different approaches to calculate the projected statistics. The first one is to calculate the radially averaged $\xi(r)$ from the simulation and then perform a line of sight integration to arrive at $w(R)$. This approach corresponds to a non-linear theory prediction. Second way is to directly calculate $w(R)$ from the 3-d correlation function $\xi(\boldsymbol{r})$ using (7.26). The latter is closer to the observations and more noisy since the number of modes in a circular shell is much lower than in a spherical shell. Furthermore the calculation of $w(R)$ from radially averaged correlation includes a spline fit of the data and hence gives a smoothed result.
The reason for the stochasticity of the galaxy catalogues is twofold: Firstly there is the cosmic variance, which will lead to different results even for the dark matter spectra from simulation to simulation. This cosmic variance was put into the simulations by generating a realisation of the random cosmic density field. Secondly there is stochasticity in each realisation of the galaxy catalogues. The catalogues are generated by sampling from the HOD and thus two catalogues created for the same simulation, but with different random seeds, will lead to different statistics. We try to eliminate the stochastic fluctuations by first averaging over the statistics of four catalogues for each simulation and afterwards over eight simulations. If not otherwise stated, errorbars are standard deviations between results for the eight simulations.

CHAPTER 9

Conclusions

In this last chapter we will return to the objectives of this thesis defined in §1.3 and summarise our findings. Starting with a discussion of the method used to calculate the correlation functions, we will proceed to the LRG catalogues. The latter are the basis of our findings and are thus discussed censoriously. The third and most important purpose of this thesis was to investigate the cross-correlation coefficient of the galaxy-galaxy lensing signal. We will elaborately discuss the implications of our results and devise an algorithm to confront theoretical predictions for the matter power spectrum with lensing and clustering measurements. To analyse these measurements one needs to correct properly for systematic effects introduced by redshift space distortions. Our achievements on this fourth of our objectives should be a warning to the community not to underestimate these effects. Last but not least we will comment on some open questions and future prospects for improvements.

9.1 Analysis Techniques

We developed and tested a method to calculate the clustering statistics and their projections in real and redshift space in a fast and efficient way. This method yields results that deviate only on the 3% level from an exact direct summation code over a wide range of scales. Our method could be further improved by finding a robust rule to determine the scales at which the results, obtained for different coarse mesh sizes, should be stacked. Especially for future simulations with even higher number of dark matter particles this method wins over direct summation codes. Particularly for studies of the baryon acoustic oscillation scales $r \approx 100\ h^{-1}$Mpc, direct summation codes have to sample from the dark matter distribution, whereas our code can account for all the particles. This statement is weakened if one only considers the rare tracers of the density field, such as haloes or galaxies. Being much less abundant, a direct summation code can give more exact results in a reasonable amount of time.

Problems of the FFT Approach

Further subtleties however arise from the assignment of particles to the grid as was previously noted by [Jing, 2005, Cui *et al.* , 2008]. These effects can be categorised as follows:

discreteness The density field is sampled by a finite number of tracer particles leading to a Poisson shot noise term that adds to the power spectrum.

smoothing The convolution of the density field with the assignment window function artificially smoothes the density and introduces a multiplication with the Fourier transform of the window to both the power spectrum and the shot noise.

aliasing The convolved density field is sampled on a finite number of grid points leading to alias sums over the window and the power spectrum. Because of this effect a direct correction as introduced in Equation 7.13 is not possible.

We have not investigated these effects in real space, but presume that implementation of new assignment kernels and iterative deconvolution could clearly improve the results.

Small Scale Effects

On small scales our resolution is limited by the finite grid size and can lead to spurious correlation especially for rare tracers, such as galaxies. This problem could be circumvented by either using a direct summation on small scales or by introducing an analytic continuation with a power law. In terms of the lensing signal we found coherent results between the direct summation and our new FFT approach. The FFT method does not resolve the exact clustering below one or two grid spacings $\lambda_{\mathrm{Ny}}(M = 20) \approx 0.14\ h^{-1}\mathrm{Mpc}$, but it preserves the total number of pairs and thus calculates the mean projected surface mass density correctly.

9.2 Generation of LRG Galaxy Catalogues

As a central part of this work we developed an algorithm to create galaxy catalogues for our simulations that reproduce observed galaxy-galaxy clustering and galaxy-galaxy lensing measurements. This algorithm populates the dark matter haloes and determines the parameters of the halo occupation distribution by matching the projected clustering statistics to the observation.

Interpretation of the Results

In our χ^2 minimisation we see that the HOD can approximate the observations reasonably well. This is on the one hand good news, since it tells us that the theory can describe the underlying dark matter density field sufficiently well and that the galaxy clustering is then mainly influenced by a superposition of halos of different masses, plus some recipe to account for the small scale distribution of satellites. On the other hand, the best fit models obtained with the full covariance matrix still yield relatively large χ^2, whereas by eye the correlation functions seem to fit the data.

In this context it is important to recall that the errors were estimated using a bootstrap resampling of the data set. It is not completely clear if these estimates give a reasonable answer, and if the sample considered by [Mandelbaum *et al.* , 2006a] is a representative realisation of the cosmology with enough statistical power to estimate the amount of cosmic variance. This can be doubted since there are strong features in the lensing signal, especially for the bright sample, which were not reproduced with any of the models considered in our work. If we despite of the strong correlations used the diagonal errors only, we would obtain much better χ^2. This fact strengthens our decision to use the full covariance matrix and the need for a theoretical modelling of the errors on the projected correlation functions. Recently [Smith, 2008] derived a lower bound for the covariance of the cross-correlation function. This approach could be further developed towards projected clustering and the lensing signal.

Our HOD fitting method used only one simulation volume with $V \approx 4V_{\mathrm{SDSS}}$ for the parameter estimation, and thus is subject to cosmic variance. A comparison of best fit values obtained for different simulations with the same generation prescription showed no significant differences in the inferred HOD.

The modelling of the scatter in the luminosity-mass relation used in our work, especially the assumption of a symmetric window for the bin sample, is rather ad hoc and needs better justification. In this context our HOD method could be improved by using a physically motivated conditional luminosity function to obtain a relation between luminosity and mass [Cacciato *et al.* , 2008].

The residuals between our best fit model and the measurements might be due to the fact that

we use the wrong cosmology. Recent data analyses of the WMAP experiment [Dunkley *et al.* , 2008, Komatsu *et al.* , 2008] obtained cosmological parameters that deviate from the ones used for our simulation especially in the slope of the power spectrum. This affects the underlying dark matter distribution and hence the clustering of the galaxies.

Comparison to a Similar Study

Comparing to the results of [Reid *et al.* , 2008] we have to consider that they modeled the full LRG sample from an earlier data release. We modeled two subsamples separately and obtained similar values for the upper cutoff mass of the faint and the lower cutoff mass of the bright sample in Table 8.2. So one could argue that a combination of our two samples should be comparable to the full sample. Their $\sigma_{log10} = 0.7$ translates to $\sigma = 1.13$ in our definition, i.e. we obtain a higher smoothing of the step. Our low mass cutoff for the faint sample compares well to $M_{\rm cut} = 5.6 \times 10^{13}\ h^{-1} M_\odot$ quoted by [Reid *et al.* , 2008]. Their satellite normalisation of $M_1 = 3.5 \times 10^{14}\ h^{-1} M_\odot$ is a bit lower than our value but probably compensates the difference in the satellite slope, for which they obtain $\alpha = 1$.
This reasoning is not very profound and by no means an alternative to a HOD determination for the full sample. It just helps to check whether our results are somehow reasonable. In fact modelling the full sample should lead to better constraints on the HOD parameters due to two reasons: Firstly the full sample has a higher number density and thus better constrained errors. Secondly the modelling of a luminosity-threshold sample, such as the full LRG sample, with a step in mass is physically well motivated in contrast to our modelling of the luminosity-bin sample.

Sampling of the Parameter Space

Owing to the relatively long calculation time per model, we have only calculated the goodness-of-fit for a grid of HOD parameters. In all the above discussion we should thus be aware that the parameter space might have strong gradients leading to very peaked minima, which we not resolve. Clearly a Markov chain Monte Carlo method would provide tighter constraints on the parameters, but such a chain needs a large number of points in parameter space until it converges. We are content with our approximate results, since our primary goal was to obtain a reasonable galaxy catalogue that can then be used to investigate questions about the phenomenology of galaxy clustering.
Finally we have to admit that fitting observed galaxy clustering by populating simulations might be not the most intelligent approach. Other authors successfully modeled the observed correlation and lensing using the halo model [Cacciato *et al.* , 2008]. This analytic prescription provides a much faster way to explore the parameter space and should in fact enable a Markov chain Monte Carlo method.

9.3 Cross-Correlation Coefficient and Dark Matter Recovery

Finally we used our galaxy catalogues to extract information about the galaxy–dark matter connection, especially the cross-correlation coefficient.
We developed a method to recover the dark matter clustering from galaxy-galaxy lensing and galaxy clustering measurements using the constancy of cross-correlation coefficient for a compensated excess surface density. Through removing the influence from small, non-linear scales on the excess surface mass density, we were able to construct a function Γ, whose cross-correlation coefficient is close to unity. While the non-linear matter correlation can be recovered with high fidelity, the linear correlation is only recovered at large scales or by strong compensation. Our results are based on the galaxy catalogues and are hence only applicable for the samples under consideration. The conclusions can be seen as a guide for future analytical work, based on which the dark matter correlation can be reconstructed from the measured auto- and cross-correlations.

There have been theoretical attempts such as the higher order perturbation theory (for a review see [Bernardeau *et al.* , 2002]) or the renormalised perturbation theory of [Crocce & Scoccimarro, 2006a, Crocce & Scoccimarro, 2006b] that perform better in describing the dark matter clustering than linear theory. But even in terms of perturbation theory the task to bridge the gap between dark matter and galaxies remains an open question.

Reconstruction Procedure

To conclude, we propose the following procedure to infer the matter clustering from lensing and clustering measurements:

1. Measure galaxy-galaxy lensing signal for a certain lens galaxy sample and calculate $\Delta\Sigma_{\mathrm{gm}}$ from the tangential shear.
2. Measure the galaxy-galaxy clustering and calculate the projected correlation function $w_{\mathrm{gg}}(R)$. Integrate the result to obtain $\Delta\bar{\Sigma}_{\mathrm{gg}}$.
3. Try to estimate the cluster virial radius of the galaxy sample under consideration. Use this estimated R_0 to correct for the central contributions in $\Delta\Sigma(R)$.
4. Make predictions for the transfer function and resulting matter autocorrelation functions for a set of cosmological parameters and/or modification of gravity. Use these to calculate $\Gamma_{\mathrm{mm}}^{(\mathrm{lin})}$ and find the best fit parameters by comparison to the empirical result.

9.4 Effects Related to the Projected Correlation Functions

When we want to use galaxy-galaxy lensing and galaxy clustering measurements jointly, it is important to account for the difference in the windows used for the projection. While lensing has a very broad window, clustering is typically measured over 50 h^{-1}Mpc only. This shallow window can not completely remove the redshift space distortions on large scales and a correction should be applied to recover the real space values. This correction can be well approximated with linear theory and the Kaiser formalism. A second correction has to be applied to the galaxy-matter cross-clustering inferred from the lensing to obtain the quantity corresponding to the clustering measurements. In this context our results are idealised, since all the projections were performed in real space and with a symmetric window of width 50 h^{-1}Mpc on each side. A more realistic study including the correct lensing windows could maybe improve on our results.
We have to caution the use of cosmological N-body simulations in lensing studies. The missing small scale clustering on scales below the force softening length can affect the excess surface mass density to larger scales.

9.5 Future Prospects and Possible Improvements

Baryon Effects

Our approach has the problem that we are not considering the effect of the baryonic matter on the structures that form in the universe. We rather treat the baryonic matter as non-interacting to account for the total gravitational potential. Simulations that include the baryonic matter have shown that the baryons actually lead to a change in the dark matter halo shape [Gnedin *et al.* , 2004]. This effect is known as adiabatic contraction. Consequences in the context of galaxy-galaxy lensing were discussed by [Mandelbaum *et al.* , 2006a]. They find that the contraction effect is negligible even for cluster-shape studies but that the stellar mass can boost the excess surface mass density on scales of about 0.3 h^{-1}Mpc. We however stick to the N-body simulations since baryonic simulations lack sufficient volume to allow for reliable conclusions on cosmological scales. Lensing studies with higher resolution simulations should however be accompanied by a carefull treatment of baryonic effects.

Halo Finding

In their LRG study [Reid *et al.* , 2008] find that mock catalogues created from FoF haloes have a deficit in clustering at 1 h^{-1}Mpc, which should be visible in the projected autocorrelation. They argue that this effect is due to the tendency of the FoF algorithm to link nearby haloes. We neither find such a deficit in the projected correlation nor the overly high satellite fractions they report for FoF based HOD and finally decide to use the FoF haloes for our galaxy catalogues. This discrepancy however strengthens the need for a systematic study of the differences between HODs based on spherical overdensity and friends-of-friends halo finders.

Covariance Estimation

The internal error estimators bootstrap and jackknife were recently compared to external, Monte Carlo based error estimators by [Norberg *et al.* , 2008]. They find that the internal estimators fail on small and intermediate scales, while they have the advantage that no prior knowledge of the underlying probability distribution is needed.
However, for the use of such internal error estimates the data set has to be a representative realisation of this underlying probability distribution. Furthermore internal error estimates are limited to the survey volume and can not account for cosmic variance or stochasticity on scales larger than the ones observed.
Errors on the two-point clustering statistics depend on higher order statistics of the data and unforeseen systematics might be missed by external estimates, since they consider only the effects that have been included in the underlying theory. Thus a carefull theoretical modelling of the covariance is timely. The extension of the work [Smith, 2008] towards projected correlation functions and the excess surface mass density should provide lower bounds on the covariance matrices. We also suspect that the noise in the measured covariance matrix might affect the inversion - an effect that needs to be studied systematically.

Mass Resolution

The limited mass resolution of the simulations, especially the low mass cutoff for the haloes might have an effect for our fitting procedure. The minimum halo mass is $M_{\mathrm{min}} = 1.3 \times 10^{13}\ h^{-1} M_{\odot}$. So it might occur that haloes that could host faint LRGs are not present in the simulation. This is especially dramatic since those low mass haloes are much more abundant than the high mass haloes.

Galaxy Profiles

We have not explored the possibility of a galaxy concentration different from the halo concentration, a fact that might arise from galaxies sinking to the halo centre due to dynamical friction [Berlind & Weinberg, 2002]. In this case there might be also differences in the velocity of dark matter and galaxies, finally affecting our redshift space results. In contrast to this increased concentrations, halo mergers would cause a less concentrated galaxy population.

Inference of Cosmological Parameters

The possibility of constraining both the HOD and the cosmological parameters from the clustering has been investigated by [Yoo *et al.* , 2006]. There is the important shortcoming, that models based on different cosmologies can fit the data equally well, simply by relying on a different set of HOD parameters [White & Padmanabhan, 2008]. One must use either higher order statistics or a second measurement to break the degeneracies. The currently available LRG data for the lensing are probably not sufficiently well constrained to lift this degeneracy and the covariance is not sufficiently well understood to derive the confidence intervals.

APPENDIX A

Notation and Constants

Gravitational constant	G	=	6.7×10^{-8} erg cm gr^{-2}
Speed of light	c	=	3.0×10^{10} cm s
Planck constant	h	=	6.6×10^{-27} erg s = $2\pi\hbar = 1.1 \times 10^{-27}$ erg s
Boltzmann constant	k_B	=	1.4×10^{-16} erg K^{-1}= 8.6×10^{-5} eV K^{-1}
Proton mass	m_p	=	1.7×10^{-24} gr
Electron mass	m_e	=	9.1×10^{-28} gr
Electron charge	e	=	4.8×10^{-10} esu
Electron volt	eV	=	1.6×10^{-12} erg
Thomson cross section	σ_T	=	6.7×10^{-25} cm^2
Solar mass	$M_\odot$	=	2.0×10^{33}
Solar luminosity	$L_\odot$	=	3.8×10^{33} erg s$^-$1
Solar distance	$D_\odot$	=	1 AU=1.5×10^{13} cm
Astronomical unit	AU	=	1.5×10^{13} cm
Parsec	pc	=	3.1×10^{18} cm = 3.3 ly
Year	yr	=	3.15×10^7 s

Table A.1: Units

As common in cosmology we use the parsec as unit of distance

$$1 \text{ pc} = 3.26 \text{ ly} = 3.086 \times 10^{16} \text{ m}.$$

It is often useful in cosmology to define a **conformal time** τ defined by $ad\tau = dt$. We will use dots to denote derivatives with respect to the physical time t and primes to denote derivatives with respect to conformal time τ where $w' = a(t)\dot{w}$ and $a(t)$ is the expansion factor.
All the calculations are performed in comoving coordinates and we account for the uncertainty in the current value of the Hubble constant by writing it as $H = hH_0$ where $H_0 = 100$ km s^{-1} Mpc^{-1}. This leads us to qoute comoving lengths in units of h^{-1}Mpc and masses in units of $h^{-1}M_\odot$.
To distinguish between radii in three dimensions and two dimensional projections we will use an uppercase R for the latter in contrast to a r for the three dimensional case.

gg	galaxy-galaxy
gm	galaxy-matter
mm	matter-matter
GR	general-relativity
EMT	energy-momentum-tensor
EFE	Einstein field equations
FRW	Friedmann-Robertson-Walker
NFW	Navarro, Frenk & White
EOS	equation of state
HOD	Halo Occupation Distribution
FT	Fourier Transform
FFT	Fast Fourier Transform
rms	root mean square
rhs	right hand side
lhs	left hand side
wrt	with respect to

Table A.2: List of Abbreviations

Bibliography

[Barlow, 1997] Barlow, R. 1997. *Statistics a guide to the use of statistical methods in the physical sciences*. Chichester: Wiley.

[Bartelmann & Schneider, 2001] Bartelmann, M., & Schneider, P. 2001. Weak Gravitational Lensing. *Phys. rept.*, **340**, 291–472.

[Berlind & Weinberg, 2002] Berlind, A. A., & Weinberg, D. H. 2002. The Halo Occupation Distribution: Towards an Empirical Determination of the Relation Between Galaxies and Mass. *Astrophys. j.*, **575**, 587–616.

[Bernabei *et al.* , 2003] Bernabei, R., Belli, P., Cappella, F., Cerulli, R., Montechia, F., Nozzoli, F., Incicchitti, A., Prosperi, D., Dai, C. J., Kuang, H. H., Ma, J. M., & Ye, Z. P. 2003. Dark Matter search. *Nuovo cimento rivista serie*, **26**(1), 010000–74.

[Bernardeau *et al.* , 2002] Bernardeau, F., Colombi, S., Gaztanaga, E., & Scoccimarro, R. 2002. Large-scale structure of the universe and cosmological perturbation theory. *Phys. rept.*, **367**, 1–248.

[Bertschinger, 1998] Bertschinger, E. 1998. Simulations of structure formation in the universe. *Ann. rev. astron. astrophys.*, **36**, 599–654.

[Bonoli & Pen, 2008] Bonoli, S., & Pen, U. 2008. Halo stochasticity in global clustering analysis. *Arxiv e-prints*, **astro-ph:0810.0273**.

[Cacciato *et al.* , 2008] Cacciato, M., van den Bosch, F. C., More, S., Li, R., Mo, H. J., & Yang, X. 2008. Galaxy Clustering & Galaxy-Galaxy Lensing: A Promising Union to Constrain Cosmological Parameters. *Arxiv e-prints*, **astro-ph:0807.4932**.

[Carroll, 2004] Carroll, S. M. 2004. *Spacetime and geometry. An introduction to general relativity*. Addison Wesley, San Francisco, CA, USA;.

[Colless *et al.* , 2001] Colless, M., Dalton, G., Maddox, S., Sutherland, W., Norberg, P., Cole, S., Bland-Hawthorn, J., Bridges, T., Cannon, R., Collins, C., Couch, W., Cross, N., Deeley, K., De Propris, R., Driver, S. P., Efstathiou, G., Ellis, R. S., Frenk, C. S., Glazebrook, K., Jackson, C., Lahav, O., Lewis, I., Lumsden, S., Madgwick, D., Peacock, J. A., Peterson, B. A., Price, I., Seaborne, M., & Taylor, K. 2001. The 2dF Galaxy Redshift Survey: spectra and redshifts. *Mon. not. roy. astron. soc.*, **328**, 1039–1063.

[Cooray & Sheth, 2002] Cooray, A., & Sheth, R. 2002. Halo models of large scale structure. *Phys.rept.*, **372**, 1–129.

[Crocce & Scoccimarro, 2006a] Crocce, M., & Scoccimarro, R. 2006a. Memory of Initial Conditions in Gravitational Clustering. *Phys. rev.*, **D73**, 063520.

[Crocce & Scoccimarro, 2006b] Crocce, M., & Scoccimarro, R. 2006b. Renormalized Cosmological Perturbation Theory. *Phys. rev.*, **D73**, 063519.

[Cui *et al.* , 2008] Cui, W., Liu, L., Yang, X., Wang, Y., Feng, L., & Springel, V. 2008. An Ideal Mass Assignment Scheme for Measuring the Power Spectrum with Fast Fourier Transforms. *Astrophys. j.*, **687**, 738–744.

[Davis *et al.* , 1985] Davis, M., Efstathiou, G., Frenk, C. S., & White, S. D. M. 1985. The evolution of large-scale structure in a universe dominated by cold dark matter. *Astrophys. j.*, **292**, 371–394.

[Dunkley *et al.* , 2008] Dunkley, J., Komatsu, E., Nolta, M. R., Spergel, D. N., Larson, D., Hinshaw, G., Page, L., Bennett, C. L., Gold, B., Jarosik, N., Weiland, J. L., Halpern, M., Hill, R. S., Kogut, A., Limon, M., Meyer, S. S., Tucker, G. S., Wollack, E., & Wright, E. L. 2008. Five-Year Wilkinson Microwave Anisotropy Probe (WMAP) Observations: Likelihoods and Parameters from the WMAP data. *Arxiv e-prints*, **astro-ph:0803.0586v2**.

[Gnedin *et al.* , 2004] Gnedin, O. Y., Kravtsov, A. V., Klypin, A. A., & Nagai, D. 2004. Response of Dark Matter Halos to Condensation of Baryons: Cosmological Simulations and Improved Adiabatic Contraction Model. *Astrophys. j.*, **616**, 16–26.

[Guth, 1981] Guth, A. H. 1981. Inflationary universe: A possible solution to the horizon and flatness problems. *Phys. rev.*, **D23**, 347–356.

[Guzik & Seljak, 2001] Guzik, J., & Seljak, U. 2001. Galaxy-dark matter correlations applied to galaxy-galaxy lensing: predictions from the semi-analytic galaxy formation models. *Mon. not. roy. astron. soc.*, **321**, 439.

[Guzik & Seljak, 2002] Guzik, J., & Seljak, U. 2002. Virial masses of galactic halos from galaxy-galaxy lensing: theoretical modeling and application to SDSS. *Mon. not. roy. astron. soc.*, **335**, 311.

[Hayashi & White, 2007] Hayashi, E., & White, S. D. M. 2007. Understanding the shape of the halo-mass and galaxy-mass cross-correlation functions. *0709.3933*.

[Hirata *et al.* , 2007] Hirata, C. M., Mandelbaum, R., Ishak, M., Seljak, U., Nichol, R., Pimbblet, K. A., Ross, N. P., & Wake, D. 2007. Intrinsic galaxy alignments from the 2SLAQ and SDSS surveys: luminosity and redshift scalings and implications for weak lensing surveys. *Mon. not. roy. astron. soc.*, **381**, 1197–1218.

[Hockney & Eastwood, 1988] Hockney, R. W., & Eastwood, J. W. 1988. *Computer simulation using particles*. Institute of Physics Publishing.

[Jenkins *et al.* , 1998] Jenkins, A., Frenk, C. S., Pearce, F. R., Thomas, P. A., Colberg, J. M., White, S. D. M., Couchman, H. M. P., Peacock, J. A., Efstathiou, G., & Nelson, A. H. 1998. Evolution of structure in cold dark matter universes. *Astrophys. j.*, **499**, 20.

[Jing, 2005] Jing, Y. P. 2005. Correcting for the alias effect when measuring the power spectrum using FFT. *Astrophys. j.*, **620**, 559–563.

[Kaiser, 1987] Kaiser, N. 1987. Clustering in real space and in redshift space. *Mon. not. roy. astron. soc.*, **227**, 1–27.

[Komatsu *et al.* , 2008] Komatsu, E., Dunkley, J., Nolta, M. R., Bennett, C. L., Gold, B., Hinshaw, G., Jarosik, N., Larson, D., Limon, M., Page, L., Spergel, D. N., Halpern, M., Hill, R. S., Kogut, A., Meyer, S. S., Tucker, G. S., Weiland, J. L., Wollack, E., & Wright, E. L. 2008. Five-Year Wilkinson Microwave Anisotropy Probe (WMAP) Observations: Cosmological Interpretation. *Arxiv e-prints*, **astro-ph:0803.0547**.

[Kravtsov *et al.* , 2004] Kravtsov, A. V., Berlind, A. A., Wechsler, R. H., Klypin, A. A., Gottlöber, S., Allgood, B., & Primack, J. R. 2004. The Dark Side of the Halo Occupation Distribution. *Astrophys. j.*, **609**, 35–49.

[Lacey & Cole, 1994] Lacey, C., & Cole, S. 1994. Merger Rates in Hierarchical Models of Galaxy Formation - Part Two - Comparison with N-Body Simulations. *Mon. not. roy. astron. soc.*, **271**, 676–+.

[Liddle & Lyth, 2000] Liddle, A. R., & Lyth, D. H. 2000. *Cosmological inflation and large-scale structure*. Cambridge Univ Pr.

[Lokas & Mamon, 2001] Lokas, E. L., & Mamon, G. A. 2001. Properties of spherical galaxies and clusters with an NFW density profile. *Mon. not. roy. astron. soc.*, **321**, 155.

[Mandelbaum *et al.* , 2005] Mandelbaum, R., Tasitsiomi, A., Seljak, U., Kravtsov, A. V., & Wechsler, R. H. 2005. Galaxy-galaxy lensing: Dissipationless simulations versus the halo model. *Mon.not.roy.astron.soc.*, **362**, 1451–1462.

[Mandelbaum *et al.* , 2006a] Mandelbaum, R., Seljak, U., Cool, R. J., Blanton, M., Hirata, C. M., & Brinkmann, J. 2006a. Density profiles of galaxy groups and clusters from sdss galaxy-galaxy weak lensing. *Mon. not. roy. astron. soc.*, **372**, 758–776.

[Mandelbaum *et al.* , 2006b] Mandelbaum, R., Hirata, C. M., Ishak, M., Seljak, U., & Brinkmann, J. 2006b. Detection of large scale intrinsic ellipticity-density correlation from the Sloan Digital Sky Survey and implications for weak lensing surveys. *Mon. not. roy. astron. soc.*, **367**, 611–626.

[Mandelbaum *et al.* , 2006c] Mandelbaum, R., Seljak, U., Kauffmann, G., Hirata, G. M., & Brinkmann, J. 2006c. Galaxy halo masses and satellite fractions from galaxy-galaxy lensing in the sdss: stellar mass, luminosity, morphology, and environment dependencies. *Mon.not.roy.astron.soc.*, **368**, 715.

[Mandelbaum *et al.* , 2008] Mandelbaum, R., Seljak, U., & Hirata, C. M. 2008. A halo mass-concentration relation from weak lensing. *Journal of cosmology and astro-particle physics*, **8**, 6.

[McDonald, 2006] McDonald, P. 2006. Clustering of dark matter tracers: Renormalizing the bias parameters. *Phys. rev.*, **D74**(10), 103512.

[Miralda-Escude, 1991] Miralda-Escude, J. 1991. The correlation function of galaxy ellipticities produced by gravitational lensing. *Astrophys. j.*, **380**, 1–8.

[Miralda-Escude, 1996] Miralda-Escude, J. 1996. The Mass Distribution in Clusters of Galaxies from Weak and Strong Lensing. *Pages 131–+ of:* Kochanek, C. S., & Hewitt, J. N. (eds), *Astrophysical applications of gravitational lensing*. IAU Symposium, vol. 173.

[Mukhanov, 2005] Mukhanov, V. 2005. *Physical foundations of cosmology*. Cambridge University Press.

[Navarro *et al.* , 1996] Navarro, J. F., Frenk, C. S., & White, S. D. M. 1996. The Structure of Cold Dark Matter Halos. *Astrophys. j.*, **462**, 563–575.

[Neyman & Scott, 1952] Neyman, J., & Scott, E. L. 1952. A Theory of the Spatial Distribution of Galaxies. *Astrophys. j.*, **116**, 144.

[Norberg *et al.* , 2008] Norberg, P., Baugh, C. M., Gaztanaga, E., & Croton, D. J. 2008. Statistical Analysis of Galaxy Surveys - I. Robust error estimation for 2-point clustering statistics. *Arxiv e-prints*, **astro-ph:0810.1885**.

[Padmanabhan *et al.* , 2008] Padmanabhan, N., White, M., Norberg, P., & Porciani, C. 2008. The real-space clustering of luminous red galaxies around z<0.6 quasars in the sloan digital sky survey. *Arxiv e-prints*, **astro-ph:0802.2105**.

[Padmanabhan, 1993] Padmanabhan, T. 1993. *Structure formation in the universe*. Cambridge University Press.

[Peacock, 1999] Peacock, J. A. 1999. *Cosmological Physics*. Cambridge University Press.

[Peacock & Smith, 2000] Peacock, J. A., & Smith, R. E. 2000. Halo occupation numbers and galaxy bias. *Mon. not. roy. astron. soc.*, **318**, 1144.

[Peebles, 1980] Peebles, P. J. E. 1980. *The large-scale structure of the universe*. Princeton, NJ: Princeton University Press.

[Press & Schechter, 1974] Press, W. H., & Schechter, P. 1974. Formation of galaxies and clusters of galaxies by selfsimilar gravitational condensation. *Astrophys. j.*, **187**, 425–438.

[Raffelt & Murdin, 2002] Raffelt, G., & Murdin, P. 2002. Dark Matter: Its Nature.

[Reid & Spergel, 2008] Reid, B. A., & Spergel, D. N. 2008. Constraining the LRG Halo Occupation Distribution using Counts-in-Cylinders. *Arxiv e-prints*, **astro-ph:0809.4505**.

[Reid *et al.* , 2008] Reid, B. A., Spergel, D. N., & Bode, P. 2008. Luminous Red Galaxy Halo Density Field Reconstruction and Application to Large Scale Structure Measurements. *Arxiv e-prints*, **astro-ph:0811.1025**.

[Rich, 2001] Rich, J. 2001. *Fundamentals of cosmology*. Springer.

[Schneider, 2006] Schneider, P. 2006. *Introduction to Gravitational Lensing and Cosmology*. Gravitational Lensing: Strong, Weak and Micro, Saas-Fee Advanced Courses, Volume 33. ISBN 978-3-540-30309-1. Springer-Verlag Berlin Heidelberg, 2006, p. 1. Pages 1–+.

[Scoccimarro, 1998] Scoccimarro, R. 1998. Transients from Initial Conditions: A Perturbative Analysis. *Mon. not. roy. astron. soc.*, **299**, 1097.

[Scoccimarro, 2004] Scoccimarro, R. 2004. Redshift-Space Distortions, Pairwise Velocities and Nonlinearities. *Phys. rev.*, **D70**, 083007.

[Seljak, 2000a] Seljak, U. 2000a. Analytic model for galaxy and dark matter clustering. *Mon. not. roy. astron. soc.*, **318**, 203.

[Seljak, 2000b] Seljak, U. 2000b. *Lectures on dark matter*.

[Seljak & Warren, 2004] Seljak, U., & Warren, M. S. 2004. Large-scale bias and stochasticity of haloes and dark matter. *Mon. not. roy. astron. soc.*, **355**, 129–136.

[Seljak & Zaldarriaga, 1996] Seljak, U., & Zaldarriaga, M. 1996. A Line of Sight Approach to Cosmic Microwave Background Anisotropies. *Astrophys. j.*, **469**, 437–444.

[Seljak *et al.* , 2006] Seljak, U., Slosar, A., & McDonald, P. 2006. Cosmological parameters from combining the lyman-alpha forest with cmb, galaxy clustering and sn constraints. *Jcap*, **0610**, 014.

[Sheth & Tormen, 1999] Sheth, R. K., & Tormen, G. 1999. Large scale bias and the peak background split. *Mon. not. roy. astron. soc.*, **308**, 119.

[Smith, 2008] Smith, R. E. 2008. Covariance of cross-correlations: towards efficient measures for large-scale structure. *Arxiv e-prints*, **astro-ph:0810.1960**.

[Smith *et al.* , 2003] Smith, R. E., Peacock, J. A., Jenkins, A., White, S. D. M., Frenk, C. S., Pearce, F. R., Thomas, P. A., Efstathiou, G., & Couchman, H. M. P. 2003. Stable clustering, the halo model and nonlinear cosmological power spectra. *Mon. not. roy. astron. soc.*, **341**, 1311.

[Smith *et al.* , 2007] Smith, R. E., Scoccimarro, R., & Sheth, R. K. 2007. Scale dependence of halo and galaxy bias: Effects in real space. *Phys. rev.*, **75**(6), 063512.

[Spergel *et al.* , 2003] Spergel, D. N., Verde, L., Peiris, H. V., Komatsu, E., Nolta, M. R., Bennett, C. L., Halpern, M., Hinshaw, G., Jarosik, N., Kogut, A., Limon, M., Meyer, S. S., Page, L., Tucker, G. S., Weiland, J. L., Wollack, E., & Wright, E. L. 2003. First-Year Wilkinson Microwave Anisotropy Probe (WMAP) Observations: Determination of Cosmological Parameters. *Astrophys. j.*, **148**, 175–194.

[Spergel *et al.* , 2007] Spergel, D. N., Bean, R., Doré, O., Nolta, M. R., Bennett, C. L., Dunkley, J., Hinshaw, G., Jarosik, N., Komatsu, E., Page, L., Peiris, H. V., Verde, L., Halpern, M., Hill, R. S., Kogut, A., Limon, M., Meyer, S. S., Odegard, N., Tucker, G. S., Weiland, J. L., Wollack, E., & Wright, E. L. 2007. Three-Year Wilkinson Microwave Anisotropy Probe (WMAP) Observations: Implications for Cosmology. *Astrophys. j.*, **170**, 377–408.

[Springel, 2005] Springel, V. 2005. The cosmological simulation code gadget-2. *Mon.not.roy.astron.soc.*, **364**, 1105–1134.

[Tegmark *et al.* , 2006] Tegmark, M., Eisenstein, D. J., Strauss, M. A., Weinberg, D. H., Blanton, M. R., Frieman, J. A., Fukugita, M., Gunn, J. E., Hamilton, A. J. S., Knapp, G. R., Nichol, R. C., Ostriker, J. P., Padmanabhan, N., Percival, W. J., Schlegel, D. J., Schneider, D. P., Scoccimarro, R., Seljak, U., Seo, H.-J., Swanson, M., Szalay, A. S., Vogeley, M. S., Yoo, J., Zehavi, I., Abazajian, K., Anderson, S. F., Annis, J., Bahcall, N. A., Bassett, B., Berlind, A., Brinkmann, J., Budavari, T., Castander, F., Connolly, A., Csabai, I., Doi, M., Finkbeiner, D. P., Gillespie, B., Glazebrook, K., Hennessy, G. S., Hogg, D. W., Ivezić, Ž., Jain, B., Johnston, D., Kent, S., Lamb, D. Q., Lee, B. C., Lin, H., Loveday, J., Lupton, R. H., Munn, J. A., Pan, K., Park, C., Peoples, J., Pier, J. R., Pope, A., Richmond, M., Rockosi, C., Scranton, R., Sheth, R. K., Stebbins, A., Stoughton, C., Szapudi, I., Tucker, D. L., Berk, D. E. V., Yanny, B., & York, D. G. 2006. Cosmological constraints from the SDSS luminous red galaxies. *Phys. rev.*, **D74**(12), 123507.

[Tinker, 2007] Tinker, J. L. 2007. Redshift-space distortions with the halo occupation distribution - II. Analytic model. *Mon. not. roy. astron. soc.*, **374**, 477–492.

[Tyson *et al.* , 1984] Tyson, J. A., Valdes, F., Jarvis, J. F., & Mills, Jr., A. P. 1984. Galaxy mass distribution from gravitational light deflection. *Astrophys. j.*, **281**, L59–L62.

[Vikhlinin *et al.* , 1999] Vikhlinin, A., McNamara, B. R., Hornstrup, A., Quintana, H., Forman, W., Jones, C., & Way, M. 1999. X-Ray Overluminous Elliptical Galaxies: A New Class of Mass Concentrations in the Universe? *Astrophys. j. l.*, **520**, L1–L4.

[White & Padmanabhan, 2008] White, M., & Padmanabhan, N. 2008. Breaking Halo Occupation Degeneracies with Marked Statistics. *Arxiv e-prints*.

[White & Rees, 1978] White, S. D. M., & Rees, M. J. 1978. Core condensation in heavy halos - A two-stage theory for galaxy formation and clustering. *Mon. not. roy. astron. soc.*, **183**, 341–358.

[Yoo *et al.* , 2006] Yoo, J., Tinker, J. L., Weinberg, D. H., Zheng, Z., Katz, N., & Dave, R. 2006. From galaxy-galaxy lensing to cosmological parameters. *Astrophys. j.*, **652**, 26–42.

[York *et al.* , 2000] York, D. G., *et al.* . 2000. The Sloan Digital Sky Survey: technical summary. *Astron. j.*, **120**, 1579–1587.

[Zheng *et al.* , 2008] Zheng, Z., Zehavi, I., Eisenstein, D. J., Weinberg, D. H., & Jing, Y. 2008. Halo Occupation Distribution Modeling of Clustering of Luminous Red Galaxies. *Arxiv e-prints*, **astro-ph:0809.1868**.

Index